IOWA STATE UNIVERSITY
Digital Repository

Graduate Theses and Dissertations

Iowa State University Capstones, Theses and Dissertations

2010

Effects of grid resolution in a three-dimensional hydrostatic model: Modeling field observations

Joshua Scanlon
Iowa State University

Follow this and additional works at: https://lib.dr.iastate.edu/etd

 Part of the Civil and Environmental Engineering Commons

Recommended Citation
Scanlon, Joshua, "Effects of grid resolution in a three-dimensional hydrostatic model: Modeling field observations" (2010). *Graduate Theses and Dissertations*. 11257.
https://lib.dr.iastate.edu/etd/11257

This Thesis is brought to you for free and open access by the Iowa State University Capstones, Theses and Dissertations at Iowa State University Digital Repository. It has been accepted for inclusion in Graduate Theses and Dissertations by an authorized administrator of Iowa State University Digital Repository. For more information, please contact digirep@iastate.edu.

Effects of grid resolution in a three-dimensional hydrostatic model: Modeling field observations

by

Joshua Allen Scanlon

A thesis submitted to the graduate faculty
in partial fulfillment of the requirements for the degree of
MASTER OF SCIENCE

Major: Civil Engineering (Environmental Engineering)

Program of Study Committee:
Chris Rehmann, Major Professor
Timothy Ellis
John Downing

Iowa State University
Ames, Iowa
2010

Copyright © Joshua Allen Scanlon, 2010. All rights reserved.

This thesis is dedicated to my parents, who have always challenged me to succeed in all of life's endeavors. I would not be where I am today without your love and support.

TABLE OF CONTENTS

LIST OF TABLES

LIST OF FIGURES

ACKNOWLEDGEMENTS

I would first like to then the National Science Foundation Physical Oceanography Program for their financial support of this project. To Danielle Wain, thank you for all the help you gave in paving the way for my contribution to this project. For all your help over the last two years, I'd like to thank Mike Kohn. Although it's quite possible that we've spent entirely too much time out on the lake with each other, I couldn't imagine a better friend to do it with all over again. For all their help with the field work, I'd like to thank Adam Wright, Emily Libbey, and Taryn Tigges. I'd like to acknowledge Peter van der Linden, Matt Fairchild, Jane Shuttleworth, and Dennis Heimdal at Iowa Lakeside Laboratory; you never stopped to amaze me with your willingness to assist with our field work, allowing us access to lab space, and the genuine interest you gave in our research. I'd like to thank Gary Owen at the Iowa Department of Natural Resources and Tom Clary at Clary Lake Service, for their help with the logistics of the 2009 field study. To my office mate Joel Sikkema, thanks for all the friendly debates, lunch-hour chats, and being a soundboard for my ideas. I would also like to thank my committee, Drs. Tim Ellis and John Downing. Finally, I'd like to extend my gratitude to my advisor Dr. Chris Rehmann for your guidance, support, and advice; your enthusiasm for science is truly inspiring.

I would be remiss if I didn't thank my wife Kadera. As always, thank you for the patience and love you constantly exhibit.

ABSTRACT

Basin-scale internal waves drive the energy flux path in a stratified lake. Therefore, accurate modeling of lake response under environmental forcing is important when considering mixing and the transport of dissolved substances. The Estuary, Lake, and Coastal Ocean Model was used to determine the grid resolution required to model field observations from Ada Hayden Lake and West Okoboji Lake. The use of the hydrostatic assumption in modeling wind-forced motions across a wide frequency spectrum accurately reproduced field observations, supporting the use of the hydrostatic assumption. Model results were compared to field data using dimensionless variables for potential and kinetic energy to assess the model's ability to predict stratification and internal wave oscillations. The results indicated best model performance for a fine model grid: horizontal resolutions between 150-225 points per V1H1 wavelength and vertical resolutions between 95-140 points over the depth produced normalized energy values within 25% of field observations.

NOTATION LIST

A = area

A_{ij} = matrix coefficients for conservation of momentum

A_s = surface area

a_k = viscous discretization term for top face of cell k

$\mathbf{a_m}$ = eigenvector for the m^{th} vertical mode

A_1 = integration constant in normal mode equation

B = basin width

B_{ij} = matrix coefficients for continuity

b_k = viscous discretization term for cell k

C = baroclinic discretization operator in ELCOM

C_D = drag coefficient

CFL = Courant-Friedrichs-Lewy number

c_k = viscous discretization term for bottom face of cell k

c_m = wave phase speed for the m^{th} vertical mode

c_n = wave phase speed

$D_{x,y}$ = horizontal diffusion operators in the x and y-direction, respectively

E_B = background potential energy

E_D = dynamic energy

E_K = kinetic energy per unit area

E_K' = normalized kinetic energy

E_P = potential energy per unit area

$E_{P,0}$ = potential energy reference value

$E_{P,\text{field}}$ = potential energy calculated using field data

$E_{P,\text{model}}$ = potential energy calculated using model data

E_P' = normalized potential energy

F_m = modal forcing function for the m^{th} vertical mode

Fr = Froude number

f = Coriolis frequency

G = explicit source term in ELCOM

g = gravitational acceleration

g' = reduced gravity

H = total undisturbed water depth

h = effective water depth

h_i = thickness of the i^{th} layer

I = advective discretization operator in ELCOM

i = cell location in the x-direction

j = cell location in the y-direction

K = shear velocity constant

$\mathbf{K}$ = wavenumber vector

k = cell location in the z-direction

k_K = x-component of the wavenumber

L = basin length

L_N = Lake number

L_R = Rossby radius

l_K = y-component of the wavenumber

M = mixing operator in ELCOM

m_K = z-component of the wavenumber

N = buoyancy frequency

n = time

n_x = number of horizontal nodes

n_z = number of vertical nodes

p = pressure

Q_m = modal transport due to the m^{th} vertical mode

R_0 = Rossby number

Ri_b = bulk Richardson number

Ri_g = gradient Richardson number

S = scalar value in ELCOM

$S^{(C)}$ = scalar source in ELCOM

S^* = scalar concentration due to advection in ELCOM

$\tilde{S}$ = scalar concentration after mixing in ELCOM

S_t = Schmidt stability

S_w = water surface

T = wave period

T_b = bore timescale

T_d = damping timescale

T_i = wave period of the i^{th} vertical mode

T_{KH} = billowing timescale

T_s = steepening timescale

T_w = wind duration

U = matrix containing u velocities at grid locations specified in ELCOM

U_h = depth-averaged water velocity in the x-direction

U_i = depth-averaged water velocity in the x-direction in the i^{th} layer

$\mathbf{u}$ = fluid velocity vector

u = x-component of the water velocity

u_w = wind speed at 10 m

u_* = shear velocity

V = matrix containing v velocities at grid locations specified in ELCOM

v = y-component of the water velocity

W = Wedderburn number

WS = Willmott skill number

w = z-component of the water velocity

w_{field} = vertical velocity calculated from field data

w_{model} = vertical velocity calculated from model data

w_0 = velocity amplitude

X_{field} = physical parameter based on field observations

$\bar{X}_{\text{field}}$ = time-averaged parameter value from field observations

X_{model} = physical parameter based on model results

z = elevation

z_s = elevation of the water surface

z_t = elevation of the center of the metalimnion

z_v = elevation of the center of volume

z_0 = elevation of lake bottom

z_1 = elevation of the bottom of the metalimnion

z_2 = elevation of the top of the metalimnion

α = coefficient of the nonlinear term in the wave equation

β_m = eigenvalue for the m^{th} vertical mode

Γ = numerical error scaling parameter

Γ_C = critical value of the numerical error scaling parameter

γ_k = boundary condition variable in ELCOM

ΔE_P = fluctuations in potential energy calculated from model data

ΔZ = vector of vertical grid size in ELCOM

Δx = horizontal grid size

Δt = model time step

Δz = vertical grid size

$\Delta\rho$ = density jump across an interface

δt = sub model time step

$\delta_{x,y}$ = discrete difference operators in *x* or *y*-direction, respectively

δ_0 = metalimnion thickness

ζ = wave displacement

ζ_e = end wall vertical displacement

ζ_i = displacement of the i^{th} layer

ζ_s = surface displacement

ζ_0 = initial wave displacement

η = free surface height

θ = angle wavenumber makes to horizontal

κ = diffusivity

κ_{vK} = von Kármán's constant

κ_κ = numerical diffusivity in a diffusion-dominated system

κ_ν = numerical diffusivity in a dissipation-dominated system

λ = wavelength of the V1H1 internal wave

λ_0 = initial wavelength of the gravest mode

μ = dynamic viscosity of water

ν = kinematic viscosity of water

ν_κ = numerical viscosity in a diffusion-dominated system

ν_ν = numerical viscosity in a dissipation-dominated system

ν_3 = viscosity in the *z*-direction

π_m = modal pressure due to the m^{th} vertical mode

ρ = water density

ρ_a = air density

ρ_i = i^{th} layer water density

ρ_0 = reference density

ρ' = density perturbation from reference value

$\bar{\rho}$ = background density

τ_b = shear at lake bottom

τ_s = timescale to the onset of steepening

τ_0 = wind-applied surface shear

ϕ = mode shape

φ = latitude

ξ = dimensionless parameter for numerical error terms

Ω = Earth's angular velocity

ω = wave frequency

$D\psi/Dt$ = $\partial\psi/\partial t \pm c_m \partial\psi/\partial x$, substantial derivative of ψ

CHAPTER 1: INTRODUCTION

Significance

The structure and hydrodynamics of lakes are important when considering the transport of dissolved substances and overall water quality. The presence of water constituents such as oxygen, nutrients, micro-organisms, and plankton play a large role in water quality in lakes and reservoirs. Stratification—typically caused by temperature, salinity, or both—restricts vertical mixing and therefore plays a large role in water column variability, such as affecting the availability of nutrients to phytoplankton (MacIntyre et al., 1999). For temperate freshwater lakes at mid-latitudes, stratification depends on temperature and the season. Two turnover periods in the spring and autumn vertically mix the lake throughout, with a period of strong stratification during the summer months. During the summer, the thermal structure of the lake consists of a well mixed surface layer (epilmnion), a quiescent weakly stratified bottom layer (hypolimnion), and a region of rapid density change (metalimnion, or thermocline) which separates the top and bottom layers.

Imberger (1998) outlined the energy flux path in a stratified lake by separating the overall flux into four processes: i) momentum transfer due to wind-applied surface shear, ii) seiching of internal waves, which can be related to the magnitude of the Wedderburn or Lake numbers, iii) degeneration of waves into higher frequency motions such as solitons, supercritical bores, and shear instabilities, and iv) damping of internal motions which leads to the thickening of the benthic boundary layer. The basin-scale energy flux

from the wind is of particular interest because of its dominant role in setting the thermocline in motion, which in the absence of inflows and outflows, is the primary energy store for transport and mixing below the wind-mixed layer. Therefore, modeling the basin-scale internal wave behavior is a requirement to modeling and quantifying the flux paths of nutrients in a stratified lake (Imberger, 1998). Recent evidence shows that seiching by long-period, basin-scale waves in a stratified lake generates a turbulent benthic boundary layer that can be many meters thick in the hypolimnion (Lemckert and Imberger, 1998). The internal wave field was shown to have implications for the distributions of variables such as dissolved oxygen, nitrate, hydrogen sulfide, and the reduction-oxidation potential in the metalimnion (Eckert et al., 2002), and upwelling conditions due to internal waves have been responsible for several fish kills (Marti-Cardona et al., 2008).

Modeling stratified systems can therefore have implications to predict water quality and the spatial variability of water parameters (e.g., temperature, salinity, and dissolved oxygen), characterize lake response under certain forcing conditions, and implement real-time water management systems. Layered models have been used to estimate upwelling conditions (Stevens and Lawrence, 1997), predict vertical displacements in the water column (Heaps and Ramsbottom, 1966), simulate the seasonal deepening of the mixed layer (Spigel and Imberger, 1980), and estimate mixed layer shear (Monismith, 1985). Three-dimensional, hydrostatic, numerical models have been shown to accurately predict basin-scale behavior (i.e., Casulli and Cheng, 1992; Saggio and Imberger, 1998; Hodges et al., 2000). These three-dimensional models discretize the flows onto a model grid composed of computational cells. These cells are used to

represent scalar concentrations, fluid velocities, and free surface elevations. Although hydrostatic models have been a useful tool in coastal ocean (and similar) systems, there is the criticism of the inability of a hydrostatic model to reproduce non-hydrostatic forces. These non-hydrostatic conditions shift the energy flux to small-scale mechanisms, such as wave steepening, shear billowing, and supercritical bores. To resolve non-hydrostatic forces, grid-switching strategies have been presented (Botelho et al., 2009) which result in a hybrid hydrostatic/non-hydrostatic model. Additionally, fully non-hydrostatic models have been shown to be successful in predicting non-linear motions (Botelho and Imberger, 2007; Kocyigit and Falconer, 2004).

However, despite the success of three-dimensional numerical models, numerical errors in the form of numerical diffusion and numerical viscosity can compromise model results (Rueda et al., 2007; Hodges and Rueda, 2008). Methods have been put forth to minimize numerical diffusion using filters (Laval et al., 2003a) or to assimilate field data directly into the model during a simulation run (Yeates et al., 2008). Empirical formulas relating numerical diffusivity and numerical viscosity to grid size have been found for diffusionless, inviscid, two-dimensional, simple non-linear systems using a three-dimensional hydrostatic model (Hodges et al., 2006). However, no work has been done to quantify numerical error due to model resolution while modeling real world, fully three-dimensional, wind-forced events.

Objectives

The goal of this work is to i) observe internal waves and forcing conditions across a wide frequency range, ii) assess the validity of the hydrostatic assumption in modeling observed events, iii) compare predictions from a three-dimensional, hydrostatic, numerical model to field observations, iv) provide a dialogue which quantifies model performance, and v) develop general guidelines for choosing grid sizes and model time steps.

Hypotheses

Deep lakes at mid-latitutdes can be classified as temperate lakes, which are defined to possess summer and winter stratification separated by two overturn events (Kalf, 2002). Preliminary field data and previous literature (i.e., Fee, 1967; Fee and Bachmann, 1968) indicate a stratified environment suitable for the formation of internal wave activity in two Iowa lakes. Stratified conditions during the course of the summer months are initially hypothesized to be suitable for analysis using a hydrostatic numerical model. The ability of a numerical model to capture internal wave motions is limited by the grid size (e.g., Schwab and Dietrich, 1997; Hodges et al. 2000; Botelho et al., 2009). Therefore, higher model resolution should be able to better resolve internal wave motions. Thus, it is hypothesized that the more refined the model grid, the better the model's results. The model time step should be selected as to provide stable results, as described by the Courant-Friedrichs-Lewy condition.

Organization

In this thesis, a background of physical limnology and a review of existing work will be presented in Chapter 2. Chapter 3 will address the methodology pertaining to field work, model implementation, and data analysis techniques. In Chapter 4, field and simulation results will be presented, as well as discussion on the significance of those results. A summary of the work, as well as recommendations for future work, will be given in Chapter 5.

CHAPTER 2: BACKGROUND AND LITERATURE REVIEW

Introduction

Chapter 2 reviews the background and existing work on lake response and hydrodynamics. An introductory discussion of hydrodynamics focuses on stratification and internal waves. Dimensionless numbers related to physical limnology are presented and outlined in terms of their importance for both past and present work. Analytical solutions are presented, as well as the simplifications involved when finding solutions which can accurately represent a wind-forced stratified system. Numerical schemes are introduced, with a description of a particular numerical model for its use in this work. The summary offers the motivation and significance behind the present work in context of previous work.

Stratification

For freshwater lakes, the thermal structure often consists of a well mixed epilimnion, a metalimnion with a steep temperature gradient, and a deeper weakly stratified hypolimnion (Fig. 2.1). The metalimnion can be referred to as the pycnocline when incorporating density effects on stratification, or a thermocline when considering the effects of temperature stratification. This layering of lower density water above higher density water is one example of stratification in nature. Generally, stratification is gravitationally stable, and acts to inhibit motion in the vertical direction (parallel to the

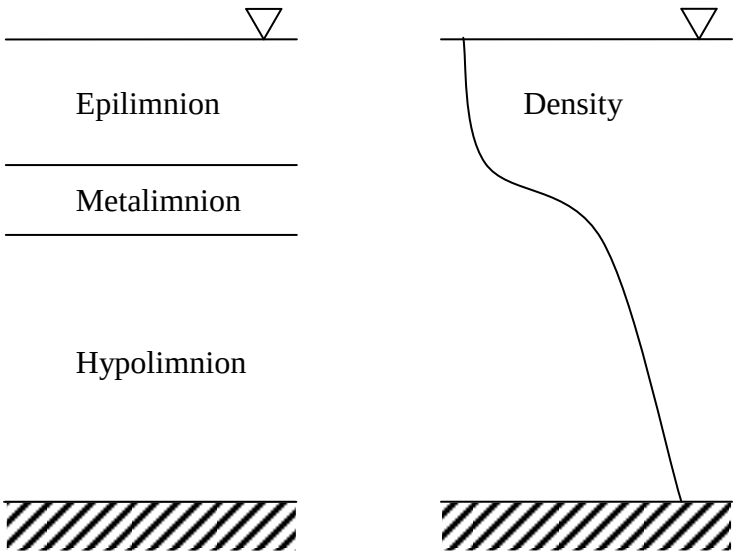

Figure 2.1. Typical temperature structure of stratified lakes during the summer months, with warmer water overlaying colder water.

density gradient). Therefore, motions generated within the stratified fluid tend to be greater in the horizontal direction.

For dimictic lakes, this stratification is established through solar heating of the surface layer during the summer months. The spring and fall overturn periods—caused by heating and cooling of the surface waters, respectively—occur when the entire water column reaches the same density and is mixed vertically throughout. Therefore, during the summer months when stratification is present, inhibited vertical mixing results in comparatively low dissolved oxygen levels in the hypolimnion. Wind further adds energy to the lake through various mechanisms. Surface stresses generate turbulence that

keeps the epilimnion well mixed. The wind shear also forms surface gravity waves which add further energy when they break and convectively mix the epilimnion. Wind stress can also tilt the water surface by pushing surface water from the windward to the leeward side of the lake.

Internal Waves and Seiches

Waves are generated because of a restoring force that tends to bring a disturbed system back to its original state and inertia that causes the system to overshoot the undisturbed position (Kundu and Cohen, 2008). In the case of a density-stratified fluid, waves can form when a horizontal density interface is disturbed. The density interface can consist of a water-air interface such as a water surface, or a water-water surface with lower density water overlying higher density water, in the case of stratified lakes. When gravity acts as the restoring force, gravity waves form. Non-dispersive, small amplitude waves will obey the wave equation

$$\frac{\partial^2 \zeta}{\partial t^2} = c_n^2 \left(\frac{\partial^2 \zeta}{\partial x^2} + \frac{\partial^2 \zeta}{\partial y^2} + \frac{\partial^2 \zeta}{\partial z^2} \right) \tag{2.1}$$

where ζ is the wave displacement and c_n is the phase speed. In a fluid with a constant density gradient, the solution for the displacement in a long rectangular basin is given by (Gill, 1982)

$$\zeta = \zeta_0 \cos(k_K x + l_K y + m_K z - \omega t) \tag{2.2}$$

where ζ_0 is the initial displacement (positive upwards), $\mathbf{K} = \left(k_K, l_K, m_K\right)$ is the wavenumber vector, and ω is the wave frequency. The internal wave's vertical velocity w can be calculated by taking the time derivative of the isotherm displacement. The horizontal velocities u and v are defined in the x and y directions, respectively. To simplify the analysis, assume two-dimensional flow, giving the solutions for u and w

$$w = w_0 \sin\left(k_K x + m_K z - \omega t\right) \tag{2.3}$$

$$u = -\frac{m}{k} w_0 \sin\left(k_K x + m_K z - \omega t\right) \tag{2.4}$$

where $w_0 = \omega\zeta_0$ is the velocity amplitude. For two-dimensional internal waves where the amplitudes for which the amplitudes are small compared to the wavelength, linear wave theory gives the frequency ω of the wave as related to the wavenumber vector $\mathbf{K}$ by the dispersion relation

$$\omega = N\left(\frac{k_K^2}{k_K^2 + m_K^2}\right)^{1/2} = N\cos\theta \tag{2.5}$$

where θ is the angle the wavenumber makes to the horizontal and N is the buoyancy frequency, defined as

$$N = \sqrt{-\frac{g}{\rho_0}\frac{\partial \bar{\rho}}{\partial z}} \tag{2.6}$$

where g is the acceleration of gravity, ρ_0 is a reference density and $\bar{\rho}$ is the background density (Turner, 1973). The buoyancy frequency provides a means for quantifying the stratification of a fluid. The dispersion relation states that a wave with a given frequency in a fluid of given stratification propagates at a specific angle. Another outcome of the dispersion relation is that the buoyancy frequency represents the upper bound for the frequency of an internal wave as the cosine term cannot be greater than one.

A seiche is a basin-scale standing wave formed by reflection of an internal wave by the boundaries. Seiches can form with n_x number of nodes in the horizontal and n_z nodes in the vertical, where n is an integer greater or equal to unity for baroclinic motions (Fig 2.2). For example, in a rectangular basin of constant width, the first horizontal mode oscillates with a wavelength of twice the length of the lake around a node in the basin's center. Lakes characterized as a two-layer system can only oscillate with a first vertical node; however, if a metalimnion has a finite thickness, higher vertical modes can exist.

The modal response in a lake is important for calculating velocity profiles, estimating isotherm displacements, and identifying modal frequencies and wave periods. A first vertical mode seiche has peak horizontal velocities at the top and bottom of the

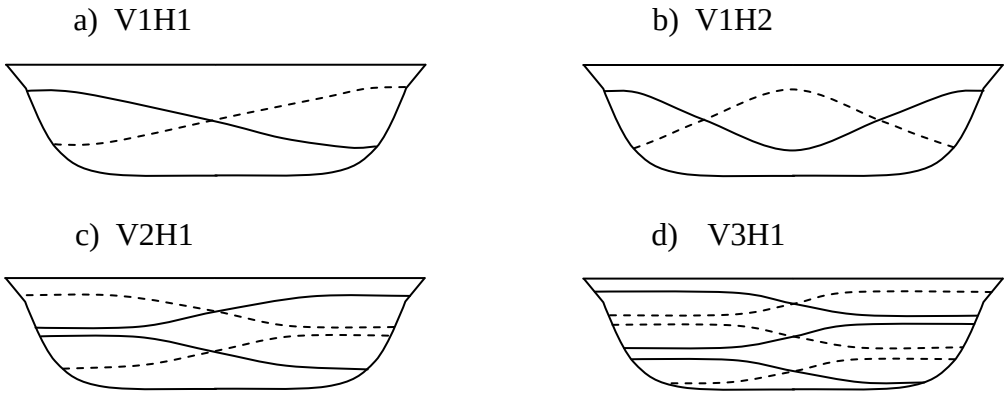

Figure 2.2. Schematic view of various seiche modes in a closed basin. Interfaces are shown for the initial maximum displacement (solid line) and one-half period later (dashed line).

water column, while increasing the number of vertical nodes yields more peaks in the velocity profile. A second vertical mode experiences an expansion and compression of the metalimnion, therefore resulting in more peaks in the velocity profile with a maximum velocity within the metalimnion (Münnich et al., 1992). The first vertical mode will see the highest shear at that central node, as the direction of horizontal velocity changes. Higher vertical nodes generate shear at each node with consequently shorter distances between these points. Therefore, higher nodes are more damped (Vidal et al., 2005). For evaluating the normal vertical mode, the simplest case is for a continuously stratified fluid with constant buoyancy frequency. Gill (1982) showed that the mode shape ϕ is governed by

$$\frac{\partial^2 \phi}{\partial z^2} + \frac{N^2}{c_n^2}\phi = 0 \tag{2.7}$$

When considering a case of constant N (i.e., linear stratification), the solution to (2.7) consists of sines and cosines. Applying boundary conditions of $\phi = 0$ at $z = 0$ and $z = H$, where H is the water depth, gives

$$\phi = A_1 \sin \frac{N}{c_n} z \tag{2.8}$$

where A_1 is an integration constant and gives the magnitude of the vertical displacement. The argument of the sine function must obey the boundary condition of no vertical displacement at the surface, giving a condition on the phase speed

$$c_n = \frac{NH}{n_z \pi} \tag{2.9}$$

where $n_z = 1, 2, 3, \ldots$ is the number of vertical nodes. The wave period T can be found by dividing the wavelength by the phase speed $T = 2\pi n_z / N$.

However, most stratified lakes and oceans have a varying density gradient. As a first approximation, the lake can be considered to be represented as a two-layer system. Because a metalimnion of finite thickness is required for a vertical mode two or higher, the preliminary approximation will yield a solution of one vertical mode (V1), but can

contain multiple horizontal nodes. Turner (1973) gave the angular frequency of the V1H*n* seiche as

$$\omega = \frac{n_x}{2L}\sqrt{g'\frac{h_1 h_2}{h_1 + h_2}} \tag{2.10}$$

where n_x is the number of horizontal nodes, $g' = g\Delta\rho / \rho_0$ which is the reduced gravity at the epilimnion-hypolimnion interface, $\Delta\rho$ is the density difference between the top and bottom layers, ρ_0 is a reference density, commonly taken as the hypolimnion density, h_1 is the thickness of the epilimnion, and h_2 is the hypolimnion thickness.

Münnich et al. (1992) expanded on the 2-layer assumption to analyze the m layer case by calculating the mode shape ϕ numerically by solving the eigenvalue problem, which amounts to solving (2.7)

$$(\Delta z)^{-2}\begin{bmatrix} -2 & 1 & 0 & 0 \\ 1 & -2 & \ddots & 0 \\ 0 & \ddots & \ddots & 1 \\ 0 & 0 & 1 & -2 \end{bmatrix}\begin{bmatrix} \phi_2 \\ \phi_3 \\ \vdots \\ \phi_{j-1} \end{bmatrix} = -c_n^{-2}\begin{bmatrix} N_2^2 & 0 & 0 & 0 \\ 0 & N_3^2 & 0 & 0 \\ 0 & 0 & \ddots & 0 \\ 0 & 0 & 0 & N_{j-1}^2 \end{bmatrix}\begin{bmatrix} \phi_2 \\ \phi_3 \\ \vdots \\ \phi_{j-1} \end{bmatrix} \tag{2.11}$$

where ϕ_k is the eigenfunction (mode shape) at vertical position $k = 2,3,..., j-1$, Δz is the vertical grid size, and N_k is the buoyancy frequency at position k. This mode model is valid for an arbitrary density profile as it accounts for varying buoyancy frequency values in the eigenvalue problem. To compute the frequency of the V*m*H1 mode, the lake

length L is divided by the solution for c_n from (2.11). For a rectangular lake, the solution for multiple horizontal nodes is more straightforward than solving an eigenvalue problem. The V*m*H*n* frequency is *n* times that of the V*m*H1. Correspondingly, the wave periods for the V*m*H2-4 modes are half, one-third, and one-quarter that of the V*m*H1.

Dimensionless Numbers

Several dimensionless numbers are used in physical limnology and geophysical fluid dynamics. The benefit of a dimensionless number lies in its use when comparing various systems across different scales. This section will outline dimensionless numbers as they pertain to this work.

Rossby Number

The description "large-scale" varies from one system to the next. Atmospheric flows are typical at much larger scales than oceanic flows, which in turn are of much larger scale than a laboratory flume. In the case of geophysical fluid dynamics, motions are to be considered large-scale when the effect of Earth's rotation becomes increasingly important (Pedlosky, 1979). The relative strengths of advective and Coriolis forces are given in the Rossby number R_0, defined as

$$R_0 = \frac{u}{fB} \tag{2.12}$$

where B is the width of flow, $f = 2\Omega \sin\varphi$ is the Coriolis frequency, calculated using Ω as the Earth's angular velocity (7.3×10^{-5} s^{-1}) and latitude φ. The Coriolis frequency is positive in the northern hemisphere and negative in the southern hemisphere. It varies from $\pm$ 1.45×10^{-4} s^{-1} at the poles to zero at the equator. The physical meaning behind the Coriolis frequency varying with latitude is that a person standing on a pole rotates, while a person standing on the equator merely translates (Kundu and Cohen, 2008).

Rotation can affect internal wave as the wave's frequency approaches the Coriolis frequency. Thus, a limit has been placed on both the upper and lower bounds of an internal wave's frequency, such that $f < \omega < N$. Similarly, effects of the Earth's rotation can be neglected if $R_o >> 1$. For low frequency waves, a length scale representing the effect of rotation on the wavelength is given by the Rossby radius L_R, defined as

$$L_R = \frac{Nh_1}{f} \tag{2.13}$$

where h_1 is the thickness of the epilimnion. The Rossby radius gives the length at which rotation forces begin to become significant. For an enclosed basin, such as a lake, the Rossby radius can indicate whether the basin size allows for rotational effects due to Coriolis forces. If the basin width is less than L_R, rotational forces can be considered negligible, which may apply to small lakes or water bodies with a long and narrow basin.

Richardson Number

Another useful relation for physical limnology and other stratified flows is the comparison of potential to kinetic energy. In this work, the relation takes the form of the bulk Richardson number Ri_b and gradient Richardson number Ri_g. The bulk Richardson number is used when comparing the buoyancy force to the inertia force in a layer of fluid. The gradient Richardson number is used for a local comparison between the velocity gradient and stratification (or buoyancy effects) and is important when dealing with turbulence and instability. When considering infinitesimal disturbances in a fluid with linear density and velocity profiles, the stability criterion for the gradient Richardson number guarantees stable flows for $Ri_b > 1/4$ (Kundu and Cohen, 2008). The Richardson number, both in bulk and gradient form, are defined as

$$Ri_b = \frac{g'h}{u_*^2} \tag{2.14}$$

$$Ri_g = \frac{N^2}{\left(\partial u / \partial z\right)^2} \tag{2.15}$$

where h is the depth of the top layer in a system with two or more layers (or the total depth for a single layer system), while the shear velocity u_* and reduced gravity g' defined as

$$u_* = \sqrt{\frac{\tau_0}{\rho_0}} \tag{2.16}$$

and

$$g' = g\,\frac{\rho_2 - \rho_1}{\rho_0} \tag{2.17}$$

where τ_0 is the wind-applied shear, ρ_2 is the density of the bottom layer, and ρ_1 is the density of the top layer. However, it is difficult to directly measure shear. The shear velocity can be estimated using measured wind speed by the following

$$u_* = \sqrt{\frac{\rho_a C_D u_w^2}{\rho_0}} \tag{2.18}$$

where ρ_a is the air density, C_D is the drag coefficient, u_w is the wind speed measured at 10 m above the water surface. In the case of a one-layer system, ρ_2 is the density of water, and ρ_1 is the air density. Since the density of water is approximately 1000 times that of air, $g' \approx g$. However, in a two-layer system ρ_2 will be slightly larger than ρ_1, resulting with $g' = O(10^{-2})$ m/s^2. Wüest and Lorke (2003) performed a least squares fit of data from several studies to yield values for the drag coefficient based on wind speed u_w

$$C_D = 0.0044 u_w^{-1.15} \qquad \text{for } u_w < 5 \text{ m/s} \tag{2.19}$$

$$C_D = \left[\frac{1}{\kappa_{vK}} \ln\left(\frac{10g}{C_D u_w^2} \right) + K \right]^{-2} \qquad \text{for } u_w > 5 \text{ m/s} \tag{2.20}$$

where κ_{vK} is von Kármán's constant (typically taken to be 0.41) and the constant K is taken to be 11.3 (Smith, 1988; Yelland and Taylor, 1966). Typical values for C_D range from 0.0011 (at u_w = 5 m/s) to 0.0021 (at u_w = 25 m/s). Estimates of wind speed can therefore be directly applied to estimate the applied wind shear.

Wedderburn Number

To relate the response of a lake to wind forcing, Spigel and Imberger (1980) modeled the lake as a two-layer system and showed that the response of the upper mixed layer depended on the magnitude of Ri_b for the upper layer and the aspect ratio of the layer depth to the lake's length (i.e. h / L). Thompson and Imberger (1980) combined these two terms to form the Wedderburn number W defined as

$$W = \frac{g' h_1^2}{u_*^2 L} \tag{2.21}$$

This classification based on W allows for a simple description of the lake response pertaining to the interface tilt. A condition in which $W = 1/2$ corresponds to

the interface surfacing at the windward end of the lake, resulting in upwelling. Greater stratification will result in higher Wedderburn numbers, as g' increases. Alternatively, as either wind speed increases or stratification strength decreases, W decreases, indicating greater movement of the interface.

Lake Number

The Wedderburn number provides valuable insight into the lake response given some basic information concerning the stratification, wind forcing, and basin size. While these are important parameters to use for describing the lake behavior as a whole, it does not account for the lake's bathymetry. To incorporate the lake bathymetry, an estimate of the lake's stability S_t is required:

$$S_t = \int_0^{z_s} (z_v - z) A(z) \rho(z) dz \tag{2.22}$$

where z_s is the height of the water surface, $A(z)$ and $\rho(z)$ are the area and density as a function of depth, respectively, and z_v is the center of volume of the lake, defined as

$$z_v = \frac{\int_0^{z_s} zA(z)dz}{\int_0^{z_s} A(z)dz} \tag{2.23}$$

A ratio of stabilizing to de-stabilizing forces may be made by taking moments about the center of volume. This ratio will yield a dimensionless group referred to as the Lake number L_N (Imberger and Patterson, 1990)

$$L_N = \frac{gS_t\left(1-z_t/z_s\right)}{\rho_0 u_*^2 A_s^{3/2}\left(1-z_v/z_s\right)} \tag{2.24}$$

where A_s is the area of the water surface $A\left(z_s\right)$ and z_t is the height to the center of the metalimnion. The stabilizing forces are defined using (2.22) coupled with gravitational acceleration and the destabilizing forces attributed to wind stress, which were not previously defined but are represented in the denominator of (2.24).

The Lake number is defined in a similar manner to the Wedderburn number in that $L_N = 1$ corresponds to upwelling at the windward end of the lake and $L_N > 10$ will result in no isotherm tilting; therefore, internal waves will theoretically exist for $L_N \leq 10$ (MacIntyre et al., 1999). For large Lake numbers, stratification will dominate the wind shear forces applied to the lake surface, resulting in little or no seiching of internal waves. The Lake number is well suited to model the response for a three-layered system as it accounts for a varying density profile in the stability term. Imberger and Patterson (1990) differentiated the first and second vertical mode by comparing values for W and L_N: mode one is characterized by small values for both W and L_N, while mode two results in small W and large L_N.

Degeneration of Internal Waves

In lakes the major source of energy required for the internal wave field is supplied by wind-induced shear at the surface. If the wind is sufficiently strong, basin-scale low frequency internal waves are formed which continue until damped by viscous forces. However, field observations show that the wind-forced basin-scale internal waves decay at a rate far greater than can be accounted for simply by internal dissipation (Stevens et al. 1996). The observed decay times require that other mechanisms must act to transfer energy from basin-scale internal waves to either smaller scale waves of shorter wavelength or turbulence and mixing.

Horn et al. (2001) evaluated degeneration mechanisms by comparing mechanism timescales in a two-layer model. The authors accounted for steepening due to nonlinear effects (solitary waves), shear instabilities (Kelvin-Helmholtz billows), and supercritical conditions (internal bores). The nonlinear non-dispersive wave equation was used to account for wave steepening

$$\frac{\partial \zeta}{\partial t} + c_n \frac{\partial \zeta}{\partial x} + \alpha \zeta \frac{\partial \zeta}{\partial x} = 0 \tag{2.25}$$

where ζ is the interface displacement and $\alpha = \frac{3}{2} c_n \left(h_1 - h_2 \right) / h_1 h_2$. Balancing the unsteady and nonlinear terms in (2.25) gives the steepening timescale T_s. The K-H billow timescale T_{KH} was found by defining a local Richardson number across the interface and

using the Richardson number criterion $Ri > 1/4$. By defining Froude numbers as $Fr_j^2 = U_j^2 / g'h_j$ for the upper ($j = 1$) and lower ($j = 2$) layers, the critical condition of $Fr_1^2 + Fr_2^2 = 1$ gives the timescale for internal bores T_b. The damping timescale T_d was given as the e-folding timescale for the internal wave amplitude decay.

Depending upon the ordering of the timescales, five possible regimes can be defined in which a particular mechanism is expected to dominate: i) damped linear waves, ii) solitary waves, iii) supercritical flow, iv) K-H billows, and v) bores and billows. The boundaries of these regimes are expressed in terms of the Wedderburn number and the ratio of the internal wave amplitude and the surface layer (Fig 2.3). All mechanisms excluding the formation of K-H billows depend on lake-specific variables. As a result, timescales and corresponding figures change depending upon the individual characteristics of a lake, such as size and stratification.

Comparisons between predictions given by the timescale analysis to laboratory experiments and field measurements confirmed its applicability (Horn et al., 2001). For all depth ratios during the experiment, $W > 5$ indicated energy loss due to damped linear waves, as the internal wave is damped before it can steepen and evolve into solitons. Therefore, outside of Regime 1, linear wave theory no longer applies. For weak forcing ($W^{-1} < 0.3$ in the experiment) an internal standing seiche was generated and eventually damped by viscosity. Moderate forcing ($0.3 < W^{-1} < 1$) resulted in the production of internal solitary waves and internal surges.

Boegman et al. (2005) expanded on the laboratory work conducted by Horn et al. (2001), particularly in quantifying temporal distribution of energy between standing

waves, and the nonlinear solitary waves and surges. Boegman et al. (2005) found that over 98% of the energy contained within a linear wave field is found in the first horizontal mode wave. Therefore, if the response falls within Regime 1, basin-scale internal standing waves will contain much of the energy within the lake.

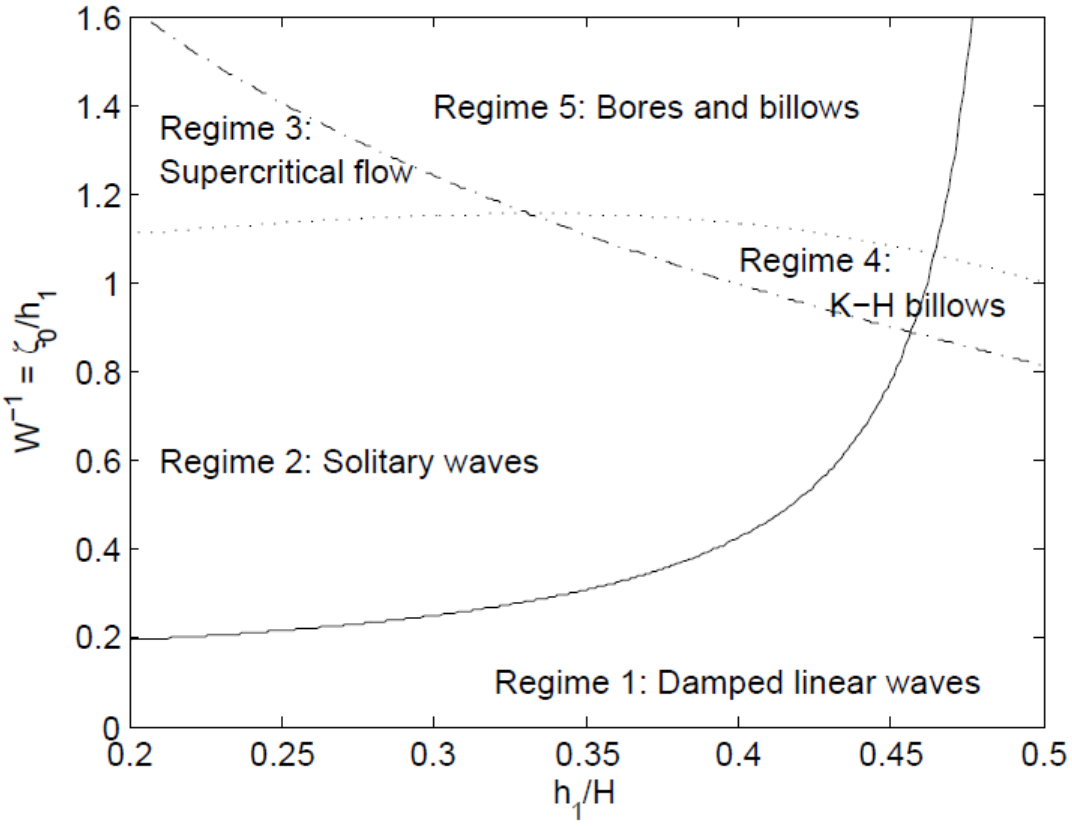

Figure 2.3. Regime boundaries for degeneration mechanism timescales: $T_d = T_s$ (solid), $T_b = T_i / 4$ (dotted), and $T_{KH} = T_i / 4$ (dash-dot). Timescales are based on laboratory conditions given in Horn et al. 2001.

Lake Modeling

To properly represent the energy flux path within a lake, basin-scale motions must be accurately reproduced. Simple energy arguments (Imberger, 1998) show that an important component of vertical mass flux in a stratified lake is through the benthic boundary layer, which is sustained initially by high-frequency internal waves breaking on the slopes and later by seiche-generated turbulence in the hypolimnion. Therefore, small errors in modeling the vertical transport will accumulate into large errors in the evolution of the density struture, resulting in poor representation of the long-term evolution of physics and ecology of a lake (Hodges et al., 2000). Thus, accurate modeling of mixing requires correct modeling of the internal wave field. Simple models must accurately incorporate the effects due to wind forcing, stratification, and basin shape, while complex models should also include the effects due to surface thermodynamics and variable bathymetry. This section will present the governing equations involved in lake and oceanic environments and present the numerical methods involved with three-dimensional modeling as a viable solution to accurately account for the complexities involved in predicting lake response.

Governing Equations

The governing equations for lake and coastal ocean systems are the equations for conservation of momentum and conservation of mass. When neglecting the effects of rotation, the conservation equations for a Newtonian fluid are given by

$$\rho \frac{D\mathbf{u}}{Dt} = -\nabla p + \rho g + \mu \nabla^2 \mathbf{u} \tag{2.26}$$

and

$$\frac{1}{\rho} \frac{D\rho}{Dt} + \nabla \cdot \mathbf{u} = \mathbf{0} \tag{2.27}$$

with pressure p, density ρ, and viscosity μ; the time substantial derivative D/Dt gives the rate of change following the fluitd motion, such that

$$\frac{D}{Dt} = \frac{\partial}{\partial t} + \mathbf{u} \cdot \nabla \tag{2.28}$$

where the fluid velocity vector can be expressed in terms of the $x - y - z$ directions as $\mathbf{u} = (u, v, w)$. Simplifying the above conservation equations by assuming a Boussinesq fluid, momentum conservation(2.26) and mass conservation (2.27) can be rewritten by expanding the substantial derivative (2.28) and Laplace operator, such that

$$\frac{\partial u}{\partial t} + u\frac{\partial u}{\partial x} + v\frac{\partial u}{\partial y} + w\frac{\partial u}{\partial z} = -\frac{1}{\rho_0}\frac{\partial p}{\partial x} + \nu\left(\frac{\partial^2 u}{\partial x^2} + \frac{\partial^2 u}{\partial y^2} + \frac{\partial^2 u}{\partial z^2}\right) \tag{2.29}$$

$$\frac{\partial v}{\partial t} + u\frac{\partial v}{\partial x} + v\frac{\partial v}{\partial y} + w\frac{\partial v}{\partial z} = -\frac{1}{\rho_0}\frac{\partial p}{\partial y} + \nu\left(\frac{\partial^2 v}{\partial x^2} + \frac{\partial^2 v}{\partial y^2} + \frac{\partial^2 v}{\partial z^2}\right) \tag{2.30}$$

$$0 = -\frac{\partial p}{\partial z} + g\rho(z) \tag{2.31}$$

$$\frac{\partial u}{\partial x} + \frac{\partial v}{\partial y} + \frac{\partial w}{\partial z} = 0 \tag{2.32}$$

where $\nu = \mu / \rho$ is the kinematic viscosity, and x and y momentum are given by the Navier-Stokes equations in (2.29) and (2.30), respectively. Gravitational forces do not enter into the momentum equations if acting in a direction perpendicular to the respective coordinate axis, thus both x and y -directions are taken to be in the horizontal plane with z in the vertical. The hydrostatic assumption is expressed in (2.31), where advective, unsteady, and viscous forces have been neglected in favor of a gravity-pressure balance; the scaling involved is shown in Cushman-Roisin (1994). The result is that pressure depends on water density, gravity, and the depth of the fluid. The pressure can be computed from (2.31) as

$$p(z) = p_0 + g\int_0^z \rho(z)\,dz \tag{2.33}$$

where depth z is the vertical distance in the fluid measured as positive down from the water surface, and p_0 is atmospheric pressure. As $z \to 0$, the pressure approaches atmospheric.

Conservation of mass (2.32), also referred to as the continuity equation, or simply continuity, assumes the substantial derivative is negligible when compared to the velocity gradient. The assumption is that the fluid is approximately incompressible, or that a fluid

parcel's density is constant. As part of the shallow water assumption, x-viscous forces are negligible compared to z-viscous forces, justified by scaling using continuity. Limiting the case to a two-dimensional solution, scaling of x-momentum (2.29) results in both advective terms of the same order of magnitude, but less than the vertical viscous term, giving

$$\frac{\partial u}{\partial t} = -\frac{1}{\rho}\frac{\partial p}{\partial x} + \nu\frac{\partial^2 u}{\partial z^2} \tag{2.34}$$

Equation (2.34) provides a simplified relationship for momentum conservation which can be used in modeling the lake response and corresponding hydrodynamic flows. Limiting the solution to a two-dimensional flow field may at first seem to be a step back in terms of accurately reproducing internal dynamics; however, the assumption will be shown in the literature to produce accurate results under certain conditions (i.e. a long, narrow lake).

Analytical Models

Analytical models are useful when considering lake response to wind forcing as they provide a succinct solution. However, analytical solutions come at a price; many simplifications and assumptions arise throughout the process. While these assumptions provide a set of equations which can solve the system explicitly, the inherent complexities of the system are lost. This section will present the shallow-water

equations, which assume the fluid can be represented by layers of constant density in a system where the depth is much less than the horizontal extent of the fluid (i.e. small aspect ratio). The first step is to define the simple one-layer case, which can be expanded to provide the solutions for systems with more layers.

One-Layer

The simplified x-momentum equation (2.34) can be used for a basic analytical solution. First, consider the steady one-layer case, initially neglecting $\partial u / \partial t$. To simplify the geometry involved, the lake can be represented by a rectangular basin of length L, total undisturbed depth H, wind-applied surface stress τ_0, surface displacement ζ_s, and effective depth h such that $h = H + \zeta_s$. A further simplification for evaluating a layered system is to integrate the conservation equations over the depth. Integration of the viscous term for x-momentum yields

$$\frac{\mu}{\rho}\int_0^h \frac{\partial^2 u}{\partial z^2}\,dz = \frac{1}{\rho}\left(\mu \left.\frac{\partial u}{\partial z}\right|_0^h\right) = \frac{1}{\rho}\left(\tau_0 - \tau_b\right) \tag{2.35}$$

where z here is defined as positive upwards from the lake bottom and τ_b is the shear along the bottom of the lake and can be assumed negligible (Lighthill, 1969). Integrating the pressure term in (2.34) using (2.33) for a constant layer density gives

$$-\int_0^h \frac{1}{\rho}\frac{\partial p}{\partial x} = -\frac{1}{\rho}\rho g h \frac{\partial}{\partial x}\left(h - z\right) = -gh\frac{\partial h}{\partial x} \tag{2.36}$$

and combining (2.35)and (2.36) gives

$$\frac{\partial h}{\partial x} = \frac{\tau_0}{\rho g h} = \frac{u_*^2}{g h} \tag{2.37}$$

Therefore, under steady conditions, the water surface tilt can be expressed in terms of shear velocity, gravity, and the water depth.

When accounting for unsteady conditions, it is first useful to integrate the continuity equation over the depth. Integrating the first term and using the Leibniz rule gives

$$\int_0^h \frac{\partial u}{\partial x} dz = \frac{\partial}{\partial x} \int_0^h u dz - \frac{\partial h}{\partial x} u(h) \tag{2.38}$$

where $u(h)$ is the horizontal velocity evaluated at the water surface. The first term on the right side of the equation relates the depth-averaged velocity U_h by the following

$$\frac{\partial}{\partial x} \int_0^h u dz = H \frac{\partial U_h}{\partial x} \tag{2.39}$$

Integrating the vertical acceleration over the depth yields the vertical velocity evaluated at the boundaries, and combining (2.38), (2.39), and the vertical velocity at h gives

$$H\frac{\partial U_h}{\partial x}+w(h)-u(h)\frac{\partial h}{\partial x}=0 \tag{2.40}$$

which is the integrated expression for continuity. To further simplify(2.40) it is useful to define the water surface as a function $S_w(x,z,t)$, and then express the surface as the difference between the elevation and surface displacement $S_w = z-\zeta_s(x,t)=0$, calculated at the free surface $z=\zeta_s$. Under the assumption that the normal velocity of fluid at a surface is equal to the normal velocity of the surface, the substantial derivative is zero when $S_w=0$. Taking the substantial derivative

$$\frac{DS_w}{Dt}=\frac{\partial S_w}{\partial t}+u\frac{\partial S_w}{\partial x}+w\frac{\partial S_w}{\partial z}=-\frac{\partial \zeta_s}{\partial t}-u(\zeta)\frac{\partial \zeta_s}{\partial x}+w(\zeta_s)=0 \tag{2.41}$$

As the water surface is defined such that the undisturbed surface is measured at $z=0$, $u(\zeta_s)=u(h)$ and $w(\zeta_s)=w(h)$ under previous notation, and the slope of the surface displacement is equivalent to the slope of the effective depth. Rearranging the final solution of (2.41) and combining with (2.40) gives a new definition for continuity

$$\frac{\partial \zeta_s}{\partial t}+H\frac{\partial U_h}{\partial x}=0 \tag{2.42}$$

To solve the unsteady case for a one-layer system, express the integral of the time derivative in (2.34) by using the Leibniz rule but define the upper bound as the sum of the undisturbed depth and the displacement $h=H+\zeta_s$. Because the magnitude of the

surface displacement's time derivative is small compared to the time derivative of the depth-averaged velocity, it can be neglected, resulting in

$$\int_0^{H+\zeta_s} \frac{\partial u}{\partial t} dz = H \frac{\partial U_h}{\partial t} \tag{2.43}$$

combining(2.43) with (2.35) and (2.36) gives x-momentum for the unsteady one-layer case:

$$\frac{\partial U_h}{\partial t} = -g \frac{\partial \zeta_s}{\partial x} + \frac{u_*^2}{h} \tag{2.44}$$

According to (2.44), the depth-averaged velocity depends on the slope of the free water surface and the wind-applied surface shear. Coupling (2.42) and (2.44) yields a solution for the velocity U_h and free surface displacement ζ_s based on the shear velocity u_*.

Two-Layer

Utilizing the one-layer solution, expanding to a two-layer solution involves much of the same procedure; however, more variables are introduced to account for additional layer depths, displacements, and velocities. Suppose subscripts 1 and 2 refer to the top and bottom layer, respectively. Therefore, let h_1 and h_2 be the undisturbed thicknesses of the epilimnion and hypolimnion, ζ_1 and ζ_2 the displacements from the undisturbed position, and $h_1 + \zeta_1$ and $h_2 + \zeta_2$ the effective thicknesses (Fig 2.4).

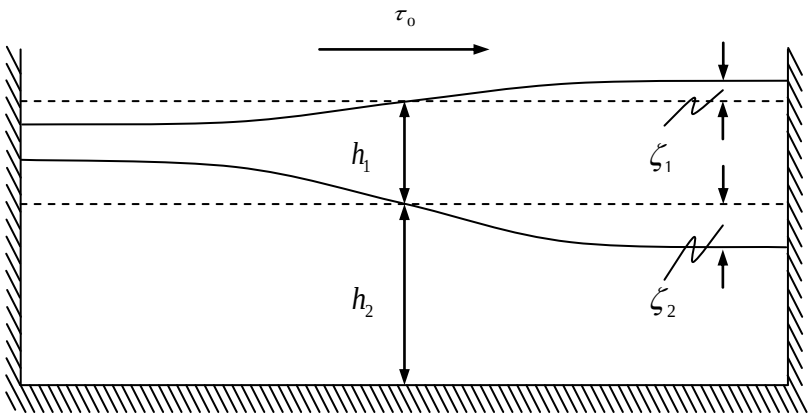

Figure 2.4. Definition sketch for a two-layer model in a rectangular basin.

The top layer can be treated similarly as the one-layer model, with the exceptions that the bottom shear is replaced with interfacial shear. Additionally, both interfacial and bottom shear can still be considered negligible under transient conditions (Csanady, 1982). Momentum conservation for layer 1 is therefore

$$\frac{\partial U_1}{\partial t} = -g\frac{\partial \zeta_1}{\partial x} + \frac{u_*^2}{h_1} \tag{2.45}$$

Continuity in the top layer is similarly treated as before in the one-layer case, but it requires defining surfaces at both the free water surface and the interface. Manipulating the depth-integrated equation and combining with the defined surface relationships yields

$$h_1\frac{\partial U_1}{\partial x} + \frac{\partial \zeta_1}{\partial t} - \frac{\partial \zeta_2}{\partial t} = 0 \tag{2.46}$$

When writing conservation of momentum for layer 2, the boundary pressure cannot be assumed to be atmospheric. Rather, as $z \to h_2$, the pressure at the interface should be given by (2.33). It is useful to express the integral bounds as the sum of the undisturbed depth and the displacement, for when differentiating with respect to x, only the displacement terms remain, giving

$$-\frac{1}{\rho_0}\frac{\partial p_2}{\partial x} = -g'\frac{\partial \zeta_2}{\partial x} - g\frac{\partial \zeta_1}{\partial x} \tag{2.47}$$

By integrating x-momentum over the depth, both viscous terms can be neglected as their respective magnitudes are small compared to the pressure terms. The kinematic shear stress, which is analogous to the viscous terms, is assumed to vary linearly throughout the mixed layer from a value of u_*^2 at the free surface to zero at the base of the mixed layer (Monismith, 1985). Therefore, viscous terms are neglected when considering anything but the surface layer.

Using (2.47) in the momentum expression for the bottom layer gives

$$\frac{\partial U_2}{\partial t} = -g\frac{\partial \zeta_1}{\partial x} - g'\frac{\partial \zeta_2}{\partial x} \tag{2.48}$$

and continuity for the bottom layer is given by

$$h_2\frac{\partial U_2}{\partial x} + \frac{\partial \zeta_2}{\partial t} = 0 \tag{2.49}$$

The two layer system can now be modeled analytically by using (2.46) - (2.49), given an initial density profile and information related to the environmental forcing (i.e. wind-applied shear).

Simplifying the above momentum and continuity equations by assuming steady conditions yields an important relationship. Under steady conditions, the only terms remaining in (2.48) are the pressure terms given in (2.47). Rearranging the expressions to compare free water and interface displacements yields

$$\frac{\partial \zeta_2 / \partial x}{\partial \zeta_1 / \partial x} = \frac{-\rho_0}{\Delta \rho} \tag{2.50}$$

The tilting of the free surface is often referred to as the barotropic response, while baroclinic response refers to internal responses caused by layer interfaces. The required time for equilibrium conditions for interface set-up is $T_i / 4$, as the effects of the end walls have not made themselves felt for $t < T_i / 4$ (Spigel and Imberger, 1980). Here, T_i is the wave period of the i^{th} vertical mode, which increases with increasing modes (Monismith, 1985). Stevens and Imberger (1996) gave the non-dimensional ratio delineating whether the wind duration sufficient to allow adequate tilting to develop the i^{th} mode as $4T_w / T_i$, where T_w is the wind duration. Therefore, a time-series of u_* should first be low-pass filtered with a cutoff frequency of $4 / T_i$ before W or L_N is calculated (Stevens et al., 1997).

Three important observations can be made with the results from (2.50). First, the interfacial tilt is always opposite (or negative) of the free surface tilt. Therefore, as the

water surface tilts up towards the leeward end of the lake, the interface will rise towards the windward end. The second conclusion relates the overall magnitude given in (2.50). As previously discussed, the density difference in freshwater systems is often $O(10^0)$ kg/m^3, while the reference density is $O(10^3)$ kg/m^3. Therefore, when the water surface is tilted, the interface will experience a tilt in the opposite direction of far greater magnitude. This difference in magnitudes leads to an assumption known as the rigid lid approximation, which states that the displacement of the water surface is much less than that of the interface, and therefore $w = 0$ at the free water surface (Kundu and Cohen, 2008). The rigid lid approximation is useful when considering normal vertical modes in a stratified fluid.

Finally, if (2.50) is multiplied through by the surface displacement slope and combined with (2.37) to relate the surface displacement in terms of the shear stress, then

$$\frac{\partial \zeta_2}{\partial x} = -\frac{u_*^2}{g' h_1} = -Ri_b^{-1} \tag{2.51}$$

Therefore, if wind set-up is complete under the steady-state assumption, the interface will tilt with the magnitude of the slope equal to the inverse of the bulk Richardson number. The endwall vertical displacement can then be estimated by multiplying the slope of the interface (2.51) with the length over which it acts ($L / 2$) and combining with (2.21), giving

$$\zeta_e = \frac{h_1}{2W} \tag{2.52}$$

where ζ_e is the vertical displacement (e.g. of a fluid parcel or isotherm) at the lake's windward end and W is the Wedderburn number. Equation (2.52) shows that upwelling ($\zeta_e \le h_1$) occurs when $W \ge 1/2$.

Stevens and Lawrence (1997) compared estimated displacements based on the Wedderburn number to measured lake response from four lakes of different size: a short deep lake (Sooke Lake Reservoir), a long deep lake (Kootenay Lake), a very short, very deep lake (Brenda Pit Lake) and a short shallow lake (Chain Lake). The model provided postive results for Sooke Reservoir but tended to underpredict response for Brenda Pit and Chain Lake. The longer wave period of Kootenay Lake limited the applicability of the model, as the seiche experienced greater variations in forcing. Therefore, the Wedderburn number can be used to predict endwall displacements within an order of magnitude. Outliers in the observed data were related to weak deflections or continuing wave activity from previous events. The authors also compared the values of W and L_N to try to distinguish different vertical mode response; however, there were no periods where L_N was differing by an order of magnitude from W (L_N reached a maximum of $4W$ for Kootenay Lake). Therefore, results were deemed to be primarily mode one.

Heaps and Ramsbottom (1966) gave solutions for the two-layer case similar to (2.45), (2.46), (2.48), and (2.49) but accounted for damping by including a separate bottom shear force. The bottom friction was defined as proportional to the horizontal flow in the bottom layer. The solution for the two-layer case with bottom friction was applied to field observations from Lake Windermere with good results for the displacement of the layer interface (see Fig. 11 in Heaps and Ramsbottom, 1966). The

velocity results from the two-layer solution were unable to be compared to field work as no current measurements sensitive enough to capture velocities of $O(10^{-2})$ m/s were available.

The homogenous two-layer model was combined with the Dynamic Reservoir Simulation Model (DYRESM) (Imberger et al., 1978) to describe mixed layer deepening under different winds (Spigel, 1978; Spigel and Imberger, 1980). The combined model was applied to conditions at Wellington Reservoir, comparing predicted temperature and salinity values from the model to field data. The model fit was deemed excellent for mixed-layer depths, but the model overestimated heat content during the summer (Spigel and Imberger, 1980). Spigel (1978) cited the accuracy to generally be within $\pm$ 0.1°C for temperature and $\pm$ 10 ppm for salinity.

N-Layer

Monismith (1985) expanded on the two-layer case to formulate a solution for the response of a rectangular, n-layered, stratified lake to a temporally varying wind stress. If the effects of rotation, mixing, nonlinearity, and non-hydrostatic pressures are neglected, the equations for the conservation of momentum and continuity can be written using the summation convention, yielding for the i^{th} layer

$$\frac{\partial U_i}{\partial t} = -gA_{ij}\frac{\partial \zeta_j}{\partial x} + C_i \tag{2.53}$$

$$\frac{\partial U_i}{\partial x} = -B_{ij}\frac{\partial \zeta_j}{\partial t} \tag{2.54}$$

where C_i is the vector of kinematic stress gradient and assumed to have components $(u_*^2 / h_1, 0, 0, \ldots, 0)$. The matrices A_{ij} and B_{ij} are defined by the relations in Table 2.1

The conservation equations given by (2.53) and (2.54) were then transformed to characteristic form using variables to represent modal transport Q_m, modal pressure variations π_m, and modal forcing functions F_m, defined as (no summation on m)

$$\mathbf{a}_{\mathbf{m}i}^T U_i = Q_m \tag{2.55}$$

$$\mathbf{a}_{\mathbf{m}i}^T B_{ij} \zeta_j = \pi_m \tag{2.56}$$

$$\mathbf{a}_{\mathbf{m}i}^T C_i = F_m \tag{2.57}$$

where $\mathbf{a}_\mathbf{m}$ is the eigenvector associated with the eigenvalue β_m, which are solutions to the generalized eigenvalue problem

$$\mathbf{a}_{\mathbf{m}i}^T \left(A_{ij} - \beta_m B_{ij} \right) = 0 \tag{2.58}$$

Here, the eigenvector $\mathbf{a}_\mathbf{m}$ and eigenvalue β_m are associated with the m^{th} mode. For an n -layered model, there will be n distinct eigenvalues and eigenvectors. The first mode response is represents the barotropic response and higher modes will correspond to baroclinic motions. The phase speed c_m is defined such that $c_m^2 = g\beta_m$ for the

Table 2.1. Matrix values for conservation equation coefficients in an n-layered system (from Monismith, 1985).

Matrix	Value	Condition
A_{ij}	1	if $j=1$
A_{ij}	$\frac{\rho_j - \rho_{j-1}}{\rho_0}$	if $i \geq j$ and $j \neq 1$
A_{ij}	0	if $i < j$
B_{ij}	$1/h_1$	if $j=i$
B_{ij}	$-1/h_1$	if $j=i+1$
B_{ij}	0	if $j>i$ or $j>i+1$

appropriate mode response. Using the directional derivative $D/Dt = \partial/\partial t \pm c_m \partial/\partial x$ gives

$$\frac{DQ_m}{Dt} \pm c_m \frac{D\pi_m}{Dt} = F_m \tag{2.59}$$

which can be integrated along characteristic curves given by $dx/dt = \pm c_m$. Monismith (1985) applied the above approach to Wellington Reservoir using n = 3 to model the mixed-layer shear. The layered model predicted the mixed-layer momentum ($U_1 h_1$) as

0.55 m^2/s, which is comparable to the observed value of approximately 0.5 m^2/s given by Imberger (1985). However, the model could not accurately predict maximum velocities, two cases of different vertical structure yielded maximum shear of 0.44 and 0.065 m/s, while Imberger (1985) gave mixed-layer velocities of about 0.1 m/s. Thus, while the model failed to predict mixed-layer shear, it could properly estimate the gain in mixed-layer momentum, which Monismith (1985) attributed to the successful prediction of fluid response timing.

The layered model can estimate end-wall displacements (Stevens and Lawerence, 1997) and, by incorporating damping due to bottom friction, accurately estimate dynamic isotherm displacements over a five-day simulation (Heaps and Ramsbottom, 1966). It has been combined with a vertical mixing model to accurately estimate temperature and salinity profiles over a year (Spigel, 1978; Spigel and Imberger, 1980), and it can estimate fluid response and mixed-layer momentum (Monismith, 1985). The solution of an n-layered rectangular stratified lake has been provided (Monismith, 1985) such that higher modal responses can be solved for systems with more vertical layers.

Numerical Models

The previous section dealt with analytical models as a tool for evaluating lake response. Analytical solutions are indeed useful; however, several simplifying assumptions are necessary in order to solve the system. The assumptions vary from representing the lake with a rectangular basin, to limiting the solution to a two-

dimensional solution and neglecting convective and viscous terms in the momentum equations. To preserve the complexities within the system, numerical models have been developed which retain more details than analytical models. This section will outline selected numerical schemes used in hydrostatic models, highlight several applications of a particular hydrostatic model, discuss effects related to grid resolution in numerical modeling, and introduce the development and application of non-hydrostatic models.

Hydrostatic Models

Casulli and Cheng (1992) developed a general three-dimensional model TRIM-3D (Tidal, Residual, and Inter-tidal Mudflat), which solves the Navier-Stokes equations with the hydrostatic assumption and a semi-implicit finite difference method. The TRIM method can be classified as a two-level, single-step method which uses two time levels of information and takes a single model step to integrate forward in time. The gradient of the water surface elevation in the momentum equations, the velocity in the free surface equation, and the vertical mixing terms are discretized implicitly. However, the convective, Coriolis, and horizontal viscosity terms in the momentum equations are discretized explicitly. The free surface is solved by using the conjugate gradient method at every time step. Once the free surface is known throughout the domain, cells near the free surface are defined as either flooding or drying, which allows the model to accurately account for permanently dry areas (e.g., islands and mud flats), as well as boundary shorelines which may experience significant changes in water level.

Designating a cell as either wet or dry simplifies the computer algorithm by increasing the computational efficiency (Casulli and Cheng, 1992).

Saggio and Imberger (1998) used the TRIM-3D method to help differentiate various wave modes recorded at lower frequencies from field data. Power spectra were constructed from both field and numerical model results and compared across various frequencies. The main frequency peaks associated with basin-scale motions were well produced, but higher frequencies in the numerical spectrum deviated from the measured values. The authors reported the discrepancy for higher frequency motions was attributed to coarse (500 m) horizontal grid size and lack in the model of the generation mechanisms provided by the variability in the real winds.

Hodges et al. (2000) adapted the fundamental numerical scheme from TRIM-3D with modifications for accuracy, scalar conservation, numerical diffusion, and implementation of a mixed-layer turbulence closure. The Estuary, Lake, and Coastal Ocean Model (ELCOM) has demonstrated reasonable short-term models (approximately 4 wave periods) of hydrostatic internal waves (Hodges et al., 2000) and longer-term simulations of circulations with density structure (Laval et al., 2003b). ELCOM provides a semi-implicit solution of the hydrostatic, Boussinesq, Reynolds-averaged Navier-Stokes equations and scalar transport equations (Hodges et al., 2006). The grid is a Cartesian *z*-coordinate mesh using an Arakawa-C grid stencil: velocities are defined on cell faces with free-surface height and scalar concentrations on cell centers. The model also includes a filter to control the numerical diffusion of potential energy (Laval et al., 2003a).

ELCOM computes a model time step in a staged approach consisting of (1) introduction of surface heating/cooling in the surface layer, (2) mixing of scalar concentrations and momentum using a mixed-layer model, (3) introduction of wind energy as a momentum source in the wind-mixed layer, (4) solution of the free-surface evolution and velocity field, (5) horizontal diffusion of momentum, (6) advection of scalars, and (7) horizontal diffusion of scalars. For details on the numerical method, see Hodges et al. (2000).

To evaluate model performance, ELCOM output was compared to field observations from Lake Kinneret (Hodges et al., 2000), focusing on the reproduction of basin-scale waves, wave amplitudes, and the depth of the base of the mixed layer. The existence and reproduction of internal waves in model space can be supported by comparing isotherm displacement spectra between measured and model isotherm movement. ELCOM resolved the basin-scale waves, but showed a rapid divergence of the model and field signals for higher frequencies, which is a consequence of the dissipation occurring at numerical grid and temporal scales in the model.

A heat budget was analyzed to determine if ELCOM could accurately replicate the surface heat fluxes. Over the course of a 12 d simulation, the cumulative change is less than 0.004% of the total heat budget. The error per time step amounted to less than 10^{-5} °C in each grid cell, which is on the level of the truncation error (Hodges et al., 2000). The field data were compared to the model output in terms of wave amplitudes, depth of the mixed-layer, and phase angle. ELCOM captured the nature of the peaks and troughs in the thermocline signature and the depth of the wind-mixed layer; however, the wave phases, amplitudes, and steepness differed. ELCOM led the field data by as much

as 5 h (25% of the base period) and lagged up to 2.5 h (10% of base period). Overall, ELCOM was shown to successfully recreate basin-scale motions in the lake, but it could not resolve higher frequency waves due to restrictions in the spatial and temporal grid resolution.

Applications of Numerical Models

The importance of ELCOM as a numerical model can best be described with its wide range of applications. More specifically, the successful matching of model output to measured field data allows ELCOM to extrapolate upon known scenarios in order to incorporate hypothetical situations. Several applications of ELCOM are presented to provide a better understanding and appreciation of the importance of lake modeling.

ELCOM has been used to model the dynamics in a salt-stratified lake (Lake Maracaibo) because of concerns with highly saline water and anoxic conditions in the hypolimnion (Laval et al., 2005). Field data from Lake Maracaibo show a persistent basin-scale cyclonic gyre which dominated the lake's circulation and resulted in doming of isopycnals (Parra-Pardi, 1979). ELCOM was therefore compared to field data in terms of reproducing circulation currents and saline levels, particularly the doming of isopycnals. Simulations reproduced the observed cyclonic gyre from field studies, and while the isohaline doming was slightly underestimated, the model was able to reproduce the basic characteristics in the salinity profiles (Laval et al., 2005).

Often, meteorological field data comes from one source and ELCOM must therefore use a horizontally uniform wind field (e.g., Hodges et al., 2000; Vidal et al.,

2005; Chung et al., 2009), while using multiple wind gauges allows for spatially-varying wind fields (e.g., Leon et al., 2005; Rao et al., 2009). To evaluate the effects of spatial variations in the wind field on numerical model results, simulations were conducted using uniform and non-uniform wind fields (e.g., Laval et al., 2003; Laval et al., 2005) and compared in terms of the model's ability to reproduce circulation or the internal wave field. A non-uniform wind field more accurately reproduced the mean circulation in the surface layer for both drifter studies (Laval et al., 2003b) and in the case of setting up gyres which lead to the doming of isopycnals (Laval et al., 2005). However, applying a uniform wind field derived from the horizontally averaged wind stress improved the model's prediction for isotherm displacements and phase coherency (Laval et al., 2003).

Vidal and Casamitjana (2008) studied the response of a lake to a wind field in an attempt to capture higher vertical mode waves. The authors compared field data to model output from ELCOM and found excellent agreement for the velocity field, vertical isotherm displacement, and evaluated the internal wave field using a power spectral density plot. ELCOM reproduced the modal response of the V2 wave quite well; however, the displacements associated with the V3 modal response were damped because of the model's artificial dissipation. Additionally, ELCOM was used to find the natural periods of the modes by removing wind forcing and designating initial tilting of the isotherms. The results from the model indicate far different periods for the V2 and V3 modes than was previously predicted by solving the eigenvalue problem (i.e., Vidal et al., 2005).

Chung et al. (2009) used ELCOM to simulate turbid density inflows into a stratified reservoir with the goal of integrating real-time turbidity monitoring and

modeling systems to develop effective decision-making processes for controlling turbid inflows. For the numerical simulations, ELCOM was paired with the Computational Aquatic Ecosystem Dynamics Model (CAEDYM), which was used to simulate particle dynamics by accounting for settling and resuspension rates of non-cohesive suspended sediments. Temperature and turbidity profiles were compared between field observations and numerical simulations by calculating the mean absolute error (MAE) and the root mean square error (RMSE). The average results for temperature were 1.5°C for MAE and 1.8°C for RMSE, and the average results for turbidity were 35 NTU for MAE and 41.9 NTU for RMSE. Overall, ELCOM-CAEDYM provided excellent agreement with field measurements of turbidity propagation in the reservoir, although the model tended to under-predict the suspended sediment concentrations.

The coupling of physical and biological processes through the use of ELCOM-CAEDYM also has implications in modeling nutrient cycling and distribution (e.g. Spillman et al., 2007). The model was used to assess the role of nutrient inputs, basin-wide nutrient fluxes, and the response of phytoplankton concentrations and distribution within the Northern Adriatic Sea. To evaluate model success, simulated salinity and temperature profiles were compared to measured values, giving r^2 values of 0.908 and 0.863 for salinity and temperature, respectively. The model accurately reproduced the temperature field and the free water surface but overestimated the distribution chlorophyll concentrations within the basin and slightly underestimated the observed peak concentrations. Despite the discrepancies, the authors were able to use the model results to indicate possible nutrient reduction methods for water bodies emptying in the Northern Adriatic Sea.

The coupling of ELCOM-CAEDYM can be used as a hydrodynamic/chemical model to reproduce the thermal structure and pattern circulation in lakes (e.g. Leon et al., 2005; Rao et al., 2009), with the goal of using modeled hydrodynamic fluxes to estimate nutrient transport and distribution. Rao et al. (2009) cited considerable model skill when comparing model output to measured field data, with respect to circulation, free surface level, and thermal structure in the lake. ELCOM was able to match measured water level variabilities within 90%. The model was able to provide circulation patterns within the lake, in particular, recreating two rotating gyres in the lake interior (Leon et al., 2005). Both papers suggested the model can accurately describe flow and transport of material required for detailed water quality simulations.

Effects of Grid Resolution in Numerical Models

While numerical models have been shown to accurately resolve internal dynamics in lakes and other similar environments, numerical error created throughout the simulation can compromise the model's results. The most significant forms of error to consider when dealing with numerical models are typically seen in the form of numerical diffusion and numerical dissipation. Numerical diffusion is caused by a density-transport truncation error while a truncation error in the momentum equation results in numerical dissipation (Hodges et al., 2006).

Numerical diffusion can cause cumulative effects in a 3D model, slowly reducing the background stratification (i.e., altering the background potential energy) and thickening the metalimnion. Unstable numerical discretization methods rely on

additional viscous or diffusive terms through truncation errors (Rueda et al., 2007). ELCOM was implemented with a turbulence closure method to reduce artificial diffusion; however, cumulative numerical diffusion limits the use of the model for long-term simulations (Hodges et al., 2000).

Background potential energy is classified as the minimum potential energy attainable through adiabatic redistribution of the density field (Lorenz, 1955). Thus, in order to maintain vertical stratification, methods which reduce change in background potential energy over the course of a time step could successfully reduce numerical diffusion. One such method is a pycnocline sharpening filter based on the inverse Z transform of a linear response to a Heaviside step function (Laval et al., 2003). For a year-long ELCOM simulation, the pycnocline filter reduced artificial mixing due to numerical diffusion and retained the metalimnion stratification better than the unfiltered simulation.

However, assessing the change in background potential energy requires additional computation time and a closed basin with no mass fluxes into or out of the model domain (Yeates et al., 2008). Therefore, the pycnocline filter was further refined by comparing model results to high-resolution thermistor chain data collected in the field. The simulation results using the new thermistor chain data assimilation technique leads to more accurate long-term model performance and addresses mixing processes not resolved by the current mixing model in ELCOM.

While numerical diffusion can hinder model performance by reducing the background stratification, the damping of internal motions due to numerical dissipation can under-predict the lake response. While ELCOM has been shown to qualitatively

reproduce the internal wave structure in terms of peaks and troughs in the motions, the model output exhibited decreased amplitudes and damping of internal waves (Hodges et al., 2000; Vidal and Casamitjana, 2008; Gomez-Giraldo et al., 2006). There are further complications relating to interrelationships between numerical diffusion and numerical dissipation; a theoretically perfect solution to the momentum equation may lose kinetic energy due to numerical diffusion of mass (Hodges et al., 2006).

Other consequences involved with modeling arise from representing naturally smooth features with grids of finite length scales. Due to the nature of the *z*-coordinate system in numerical modeling, bottom boundaries may experience significant changes in elevation for steep lake bottoms. The main concern associated with *z*-coordinate models is that the stair-step representation can introduce abrupt local topography, which is known to generate strong form drag (Edwards et al., 2004). Form drag contributes to higher and more widespread mixing than frictional drag (Moum and Nash, 2000). To evaluate the effect of form drag, ELCOM was compared to an analytical solution by modeling a two-dimensional wave train over a non-uniform bottom boundary (Simanjuntak et al., 2009). The authors found that weak slopes and low wavenumber internal waves can be well resolved; however, higher mode waves exhibit problems with refraction along the grid edge.

Hodges et al. (2006) estimated values of numerical diffusion and dissipation for nonlinear internal waves using ELCOM to simulate a simple unforced standing wave in a diffusionless, inviscid fluid. By assuming no molecular diffusion or dissipation, changes in the background potential energy E_B and the dynamic energy E_D could be attributed solely to numerical diffusion and numerical dissipation, respectively. Simulations were

modeled past the time scale to the onset of steepening τ_s, which is similar to the steepening timescale T_s given by Horn et al. (2001). Results show numerical dissipation (i.e., loss of E_D) becomes prevalent after time τ_s.

To compare results, Hodges et al. (2006) grouped simulations into "dissipation-dominated" and "diffusion-dominated" based upon their changes in E_D and E_B, respectively, and found for times $0 < t < \tau_s$

$$\kappa_\nu = Ri_g^{-1/3} \frac{\zeta_0^2}{T} \left(\frac{\Delta z^2}{\delta_0^2} \right) \tag{2.60}$$

$$\kappa_\kappa = Ri_g^{-1/3} \frac{\delta_0^2}{T} \left(\frac{\Delta z^2}{\delta_0^2} + \frac{\Delta x}{\lambda_0} \right) \tag{2.61}$$

$$\nu_\nu = Ri_g^{-1/3} \frac{\delta_0 \zeta_0}{T} \left(\frac{\Delta z^2}{\delta_0^2} + \sqrt{\frac{\Delta x}{\lambda_0}} \right) \tag{2.62}$$

$$\nu_\kappa = Ri_g^{-1/3} \frac{\delta_0^2}{T} \left(\frac{\Delta z^2}{\delta_0^2} + \sqrt{\frac{\Delta x}{\lambda_0}} \right) \tag{2.63}$$

where Ri_g is the gradient Richardson number, δ_0 is the interface (or metalimnion) thickness, λ_0 is the initial wavelength, T is the period of the V1H1 wave, Δx is the horizontal grid size, Δz is the vertical grid size, κ is numerical diffusivity, and ν is numerical viscosity, and subscripts κ and ν correspond to diffusion and dissipation-

dominated systems, respectively. By comparing κ_κ to ν_κ, a scaling parameter Γ was defined as

$$\Gamma = \frac{\nu_\kappa}{\kappa_\kappa}\left(1 + H\frac{|h_1 - h_2|}{h_1 h_2}\right) \tag{2.64}$$

such that $\Gamma > \Gamma_C$ corresponded to a dissipation-dominated system and $\Gamma < \Gamma_C$ to a diffusion-dominated system. Then for a dissipation-dominated system with a thin upper layer $0 < h_1 < H/2$

$$\frac{h_1}{H} < \left(\frac{2+\xi}{2\xi}\right) - \sqrt{\left(\frac{2+\xi}{2\xi}\right)^2 - \frac{1}{\xi}} \tag{2.65}$$

where the ξ term arises from (2.61) and (2.63), such that

$$\xi = \Gamma_C\left(\frac{\Delta z^2}{\delta_0^2} + \frac{\Delta x}{\lambda_0}\right)\left(\frac{\Delta z^2}{\delta_0^2} + \sqrt{\frac{\Delta x}{\lambda_0}}\right)^{-1} - 1 \tag{2.66}$$

where $\Gamma_C = 8.5$ was found to correctly place 93% of dissipation-dominated results in the regime $\Gamma > \Gamma_C$ and 94% of diffusion-dominated results in the regime $\Gamma < \Gamma_C$. Therefore, (2.64) - (2.66) can be used to determine whether a set of model conditions is likely to be dominated by numerical diffusion or dissipation using ELCOM.

Non-Hydrostatic Models

Three-dimensional hydrostatic models are commonly used to predict the basin-scale internal wave field (e.g., Hodges et al., 2000; Laval et al., 2003; Laval et al., 2005; Chung et al., 2009). However, internal wave dynamics can often be nonlinear, especially at smaller scales, and the hydrostatic assumption may no longer be valid (Hodges et al., 2006). The complication when considering nonlinear waves lies with the spatial scale of the internal wave spectrum: 1,000-10,000 m for the basin-scale waves, down to ~100-1,000 m for solitons, and about 10-100 m for shear instabilities (Botelho and Imberger, 2007). Unless horizontal grid scales are on the order of $1/10^{th}$ of the water depth, it is unlikely that a 3D non-hydrostatic model will resolve the non-hydrostatic motions (Hodges et al., 2006).

Therefore, models at high enough resolution to simulate nonlinear waves will provide further insight into the flux path of energy in lakes. While non-hydrostatic models are important in terms of reproducing internal wave activity at larger than basin-scale frequencies, the description of non-hydrostatic models at great detail is outside the scope of this work. However, to illustrate their applicability and the current stage of their development, examples of non-hydrostatic models are presented.

Examples and Applications of Non-Hydrostatic Models

Botelho et al. (2009) developed a grid switching strategy for ELCOM where the hydrostatic model predicts basin-scale internal waves but switches to a higher resolution

grid when the flow becomes non-hydrostatic in order to resolve the internal wave field utilizing additional numerical techniques (i.e., Bi-CGSTAB solver). The hybrid hydrostatic/non-hydrostatic grid-switching model was compared to measured field data from a small lake (Lake Pusiano) to assess the model's accuracy. Hydrostatic calculations were accomplished on a 100x100 m and 20x20 m horizontal uniform grid. The non-hydrostatic grid size varied from 20x20 m and 10x10 m uniform grid to a 1x1 m non-uniform grid. Overall, the non-hydrostatic waves were resolved well with the finer grid resolution, but the model could not reproduce the measured waves at frequencies approaching the buoyancy frequency. However, utilizing models at such high resolution requires a much larger amount of run time: the 1x1 m grid took approximately two days to run for a one-hour simulation.

Another example of non-hydrostatic model is a three-dimensional numerical model which solves the Boussinesq, Reynolds-averaged Navier-Stokes equations using a σ-coordinate system (Kocyigit and Falconer, 2004). The behavior of the model was compared to a simple example of a rectangular closed basin example under hydrostatic conditions and to a full-scale example using measured field data from a small lake (Esthwaite Water). The model performed well when compared to the rectangular basin in terms of reproducing velocity, pressure, and circulation within the system. When compared to the full-scale example, the ability of the model to predict velocities decreased significantly near the boundaries. Furthermore, Coriolis forces had a pronounced effect on the circulation patterns, except close to lateral boundaries (Kocyigit and Falconer, 2004). To increase model accuracy, the authors stated improvements in representing the lateral boundary interactions were necessary.

Summary

Stratification in lakes and reservoirs has been shown to restrict and inhibit vertical mixing and control the spatial variability of nutrients, dissolved oxygen, and other dissolved substances. The energy flux path consists of momentum transfer from wind-applied surface shear to the internal wave field, ultimately degenerating or dissipating. Internal dynamics within a stratified body therefore has far-reaching implications in overall water quality and aquatic biological communities.

Analytical solutions have been developed which separate the stratified body into layers of constant density and represent the lake as a rectangular basin. These solutions have been shown to accurately recreate the thermal structure and internal motions due to environmental forcing. Often systems are represented by a two or three-layer system, either treating the thermocline as an interface, or of finite thickness and uniform density.

Numerical models play an important role in representing hydrodynamics in lakes and coastal oceans. Currently, hydrostatic models have received much of the attention, as they have proven that they can reproduce basin scale motions at reasonable model computational times. Three-dimensional models have been shown to accurately reproduce thermal structures and circulation patterns. The coupling of ELCOM as a hydrodynamic model with biological/chemical models such as CAEDYM is providing new opportunities for the use of numerical models outside the physical oceanography and limnology communities. Much of success of 3D models has been well documented; however, the comparisons made between real and simulated events (especially those of

the internal wave field and surface layer circulation) is often limited to qualitative discussion. It is therefore one of the aims of this work to quantify model performance by comparing model results to field observations.

While 3D models have been shown to be accurate in predicting many facets of hydrodynamic flows, numerical modeling is limited by the presence of numerical error: numerical diffusion erodes stratification and numerical viscosity has been shown to dampen and dissipate internal motions. Much work has been done to circumvent numerical diffusion with filters, new numerical techniques, and incorporating measured data into model output, but the issue is far from resolved. Scaling has offered estimates for numerical diffusion and viscosity, but these experiments were conducted on simplified basins with simple waves. Therefore, by considering the effects of spatial and temporal resolution on model predictions, this work will evaluate the role of numerical error in model results through comparison to field observations.

CHAPTER 3: METHODS

Introduction

Chapter 3 describes the experimental methods, simulation techniques, and data analysis procedures. An objective of the completed work is to classify the response of a lake to external forcing and evaluate the effects of spatial and temporal resolutions in a three-dimensional numerical model on reproducing measured events. The response of the lake will be evaluated by means of the meteorological conditions, internal wave field, and power spectra. To accomplish this objective, meteorological conditions were measured using a Lake Diagnostic System (LDS) and used to quantify the applied wind forcing. Additionally, the thermal structure of the lake was measured using multiple thermistor chains at various locations throughout the lake. The Wedderburn and Lake numbers combine the forcing stress and the lake's thermal structure into dimensionless numbers which can be further used to classify a response. Numerical modeling of fully three-dimensional stratified flows was done using the Estuary, Lake, and Coastal Ocean Model. A brief overview of the model will be presented, followed with the methods involved with setting up and running the model. For further details on the numerical methods and proper procedures for using the model, see Hodges et al. (2000) and Hodges and Dallimore (2007). Lastly, methods for analyzing field and model results will be presented.

Field Work

The field work was conducted in two lakes over the course of three years. The summers of 2007 and 2008 were spent at Ada Hayden Lake in Ames, Iowa. West Okoboji Lake near Arnold's Park, Iowa was the site for further field research in 2009. As part of the fieldwork, several instruments were used to collect data. An overview of each lake will be presented which will provide information regarding instrument locations and general characteristics of the water body. A description of the instruments used in the field is provided, outlining the methods used for deployment and data collection.

Ada Hayden Lake

Ada Hayden Lake (Fig. 3.1) is an abandoned gravel quarry that now provides a secondary water supply for the City of Ames. It consists of two basins separated by a shallow shelf (approximately 3 m). All field measurements conducted in the larger, southern basin. The basin of interest has a surface area of approximately 0.3 km^2 and a maximum depth of about 17 m. The lake is fed through groundwater and surface runoff which is filtered through a wetland system. During the summer when the stratification of the lake is fully developed, a 4-5 m well mixed epilimnion overlies a linearly stratified hypolimnion with a buoyancy frequency N between 25 and 45 cph. Because the shelf separating the two basins is shallower than the epilimnion, only epilimnetic water is probably exchanged. Additionally, motorized boats are prohibited on the lake, minimizing any potential mixing attributed to boat traffic.

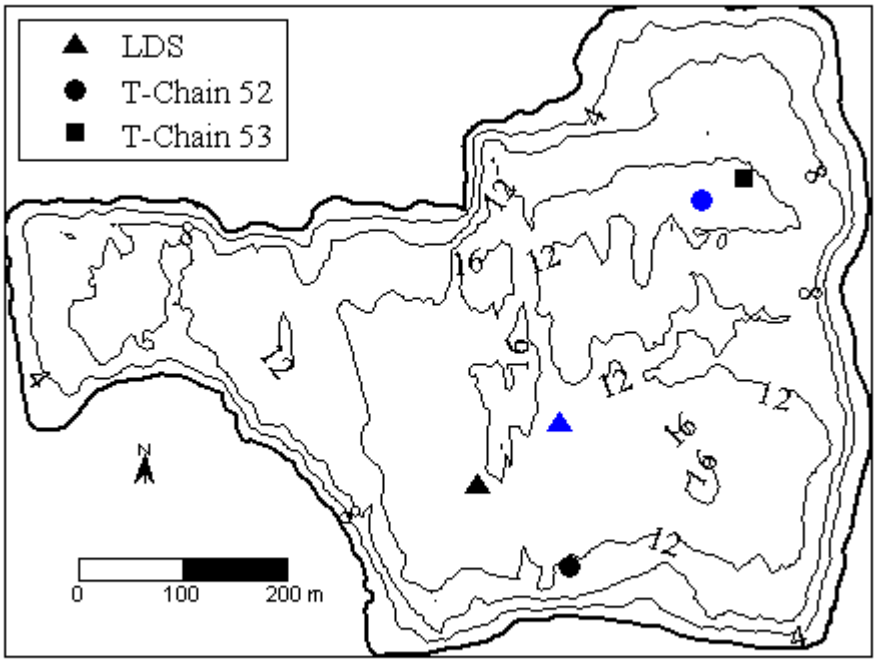

Figure 3.1. Bathymetric map of Ada Hayden Lake with 4 m contour intervals. Symbols depicting instrument deployment locations are shown for 2007 (blue) and 2008 (black). Only two thermistor chains were deployed in 2007.

The lake has steep northern, eastern, and southern sides. The LDS was deployed near the deepest section of the lake to provide measurements to the lake bottom (Fig. 3.1). Free-standing thermistor chains were deployed near the northeast and southeast section of the lake. The location for the thermistor chain at the NE corner (T-Chain 52 in 2007, T-Chain 53 in 2008) was selected to be along the primary wind axis. The location

for the SE thermistor chain (T-Chain 52 in 2008) was selected because it was at a comparable depth to T-Chain 1.

West Okoboji Lake

West Okoboji Lake (Fig. 3.2) is a natural lake located in Dickinson County in northwest Iowa. It acts as a drinking water source for several communities near the lake, as well as a popular recreation destination for sailing and power boating. It is fed primarily by groundwater and subterranean springs. West Okoboji Lake has a surface area of 15.6 km^2 and a maximum depth of 41 m. The lake flows into East Okoboji Lake through Smith's Bay through a 3 m deep channel. Because of the stratification of West Okoboji Lake during the summer months, the structure of the lake consists of a well-mixed epilimnion, a steep temperature gradient contained within a thick metalimnion, and weakly stratified hypolimnion. The epilimnion extends well below 3 m, preventing internal wave action within West Okoboji Lake from interacting with East Okoboji Lake. As such, West Okoboji Lake is considered to be an enclosed basin in this study.

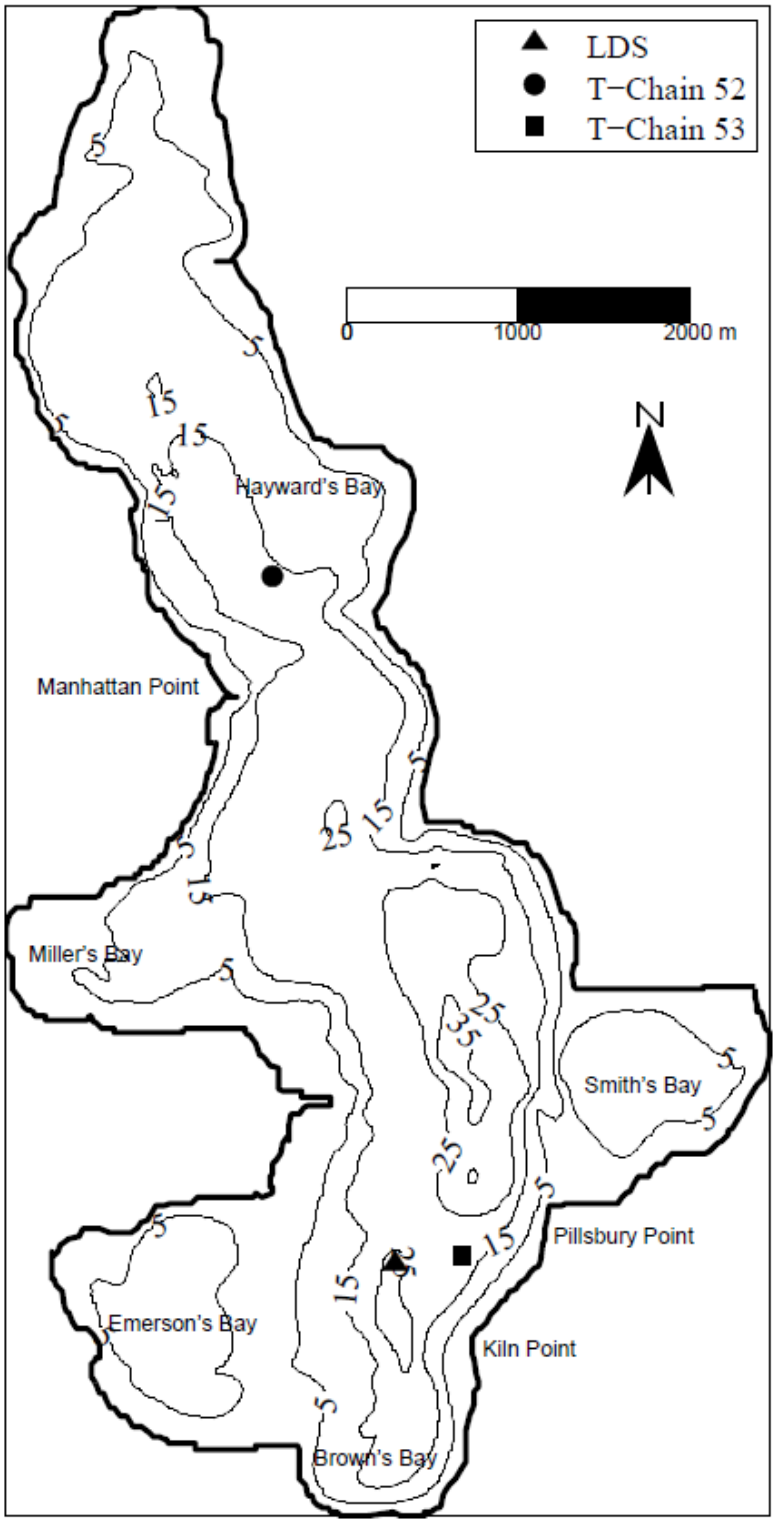

Figure 3.2. Bathymetric map of West Okoboji Lake with 5 m contour intervals. T-Chain 53 malfunctioned starting 6 July 2009.

The LDS was deployed along the thalweg of the lake in one of the deepest points of the lake (approximately 27 m), while yet far enough from high boat traffic areas to maintain safety for both boaters and field instruments. The thalweg—or "valley way"—is the deepest continuous line along the lake bottom. Regulatory hazard buoys with a mounted one-mile solar amber light (flashing at 1 Hz) were placed around the LDS to warn boaters of its location. The northern of the two free-standing thermistor chains (T-Chain 52) was deployed between Manhattan Point and Hayward's Bay (see Fig. 3.2). The southern thermistor chain (T-Chain 53) was deployed approximately 90 m offshore almost directly east of the LDS between Pillsbury and Lime Kiln Point. Because instrument locations were required to be marked by hazard buoys, additional mooring techniques were used for both freestanding T-Chains in West Okoboji Lake than previously discussed for Ada Hayden Lake. In addition to the 60 kg floats, hazard buoys were attached to the top of the T-Chains and mounted with one-mile amber lights (flashing at 1 Hz).

Lake Diagnostic System

A Lake Diagnostic System (LDS) manufactured by Precision Measurement Engineering (PME) was moored in both lakes. The LDS measures wind speed and direction, solar and net radiation, relative humidity, and air temperature. It also measured water temperature as a function of depth, as described in the next subsection. The sensors on the LDS were positioned approximately 2 m off the lake surface, with a slight variation depending on the mooring process (i.e., anchor locations, anchor weights,

weights attached to LDS frame, etc.). Wind speed and direction were measured by a propeller anemometer and wind vane, respectively, both manufactured by Met One Instruments, Inc. To estimate the heat fluxes at the water surface, a pyranometer by LI-COR was used to measure solar radiation, and net radiation was measured using a pyrradiometer by Middleton Solar. The relative humidity and air temperature were measured using a combined sensor designed by Vaisala. All the sensors on the LDS sampled every 15 s.

The LDS was moored using two lines anchored with 136 kg each for Ada Hayden Lake and 227 kg for West Okoboji Lake. Floats were attached to the mooring lines to allow the LDS to adjust to changes in the water surface. The submerged floats reduced the effective mooring mass by 60 kg each. The span of the mooring, which ranged from 45 m (Ada Hayden Lake) to 80 m (West Okoboji Lake), was set based upon the lake depth. Meteorological data collected by the LDS was recorded to an internal data logger which could store data for approximately 50 h. When deployed at Ada Hayden Lake, a wireless dial-up modem connected to the LDS transmitted measured data every 2 h. There was insufficient signal while deployed at West Okoboji Lake to use the modem and data had to be manually downloaded at least every 4 d.

Thermistor Chains

Thermistor chains, manufactured by PME, were deployed in the lake as either part of the LDS, or free-standing. The number of free-standing thermistor chains varied from one to two depending upon the year: studies were conducted in 2007 with only one free-

standing thermistor chain, 2008 used two, and 2009 used two for most of the summer (one malfunctioned starting 6 July). Each thermistor chain was approximately 30 m in length with a temperature node at approximate 1 m intervals. Each node was measured prior to deployment for the vertical distance between the thermistor and the top of the thermistor chain. Thus, once deployed, the exact depth of the temperature nodes would be known. This allowed for accurate tracking of isotherm movements between one thermistor chain and another. Once deployed, the vertical distance between the top of the thermistor chain and the water surface was measured. This vertical distance was added or subtracted for the LDS and free-standing thermistor chains depending upon the deployment procedure.

The LDS thermistor chain hung freely from the frame, with any nodes deeper than the lake at the mooring point resting on the lake bottom. These temperature nodes which were left resting on the lake bottom were not used when evaluating the temperature profile. The free-standing thermistor chains were looped to provide higher resolution temperature measurements by staggering the nodes every 0.5 m (approximately). The depth of Ada Hayden Lake at the deployment location was less than 15 m, such that the thermistor chains were merely folded over. Because West Okoboji Lake was deeper (approximately 20 m), the bottom 10 m of the thermistor chain was looped back up in order to provide higher resolution measurements near the bottom of the water column. This higher resolution provided more measurements of temperature gradient in the thermocline, resolving internal wave motions more precisely. The free-standing thermistor chains were moored to the lake bottom with a 45 kg anchor, and attached to a

buoy at the lake surface. The buoy can provide a submerged force of 60 kg; however, the floats were only partially submerged.

Field data from the free standing thermistor chains were sampled at 15 s intervals and stored in a submersible data logger on data cards. The data cards were removed every 3-4 weeks due to data space limitations, and were replaced with blank data cards such that data recording could continue. Because the frequency of internal waves cannot exceed the buoyancy frequency (approximate frequencies under strongly stratified conditions of 1×10^{-2} Hz for Ada Hayden Lake and 7×10^{-3} Hz for West Okoboji Lake), the sampling rate was chosen to resolve any high frequency internal waves which may occur. Also, the thermistor chains will not enter into a sleep mode if they sample faster than every 15 s. Thus, the sampling rate selected maximized battery efficiency while allowing for accurate measurement of high frequency waves.

The thermistor chains must not be placed near a potential horizontal node. Because seiches are standing waves, if a thermistor chain were to be placed directly on a node, it would register little (if any) temperature fluctuations attributed to seiching motions. Likewise, when considering the deployment location for three thermistor chains (one attached to the LDS, two free-standing), they should be orthogonal to capture both longitudinal and transverse seiching. Two thermistor chains should be deployed along the length of the basin to measure internal waves along the main axis of the lake. The third thermistor chain will measure internal waves along the cross section of the lake.

Estuary, Lake, and Coastal Ocean Model

The Estuary, Lake, and Coastal Ocean Model (ELCOM) numerically resolves the three-dimensional, hydrostatic, Boussinesq, Reynolds-averaged Navier-Stokes and scalar transport equations (Hodges et al., 2000). ELCOM accounts for varying bathymetry, unsteady surface stresses and heat fluxes, inflows and outflows, barotropic and baroclinic responses, rotational effects, and the transport of salt, heat, and other passive scalars (e.g. tracers and drifters). The discretization algorithms are based on the Euler-Lagrange method for advection of momentum with a conjugate-gradient solution for the free surface height (Casulli and Cheng, 1992). Scalars are advected using an ULTIMATE QUICKEST discretization (Leonard, 1991). ELCOM is implemented in FORTRAN 90 such that three-dimensional space can be mapped into a single vector for fast operation using array-processing techniques (Hodges and Dallimore, 2007). Only cells which contain water are represented, thereby maximizing computation and minimizing memory usage.

ELCOM requires, creates, and uses many files during the course of a simulation. Data is input in the form of *.dat* files. Output from the pre-processer code consists of two FORTRAN unformatted binary files: *sparsedata.unf* and *usedata.unf*. The pre-processor and processor codes used by ELCOM are executable files, *pre_elcom.exe* and *elcom.exe*, respectively. The output from the processing code is in the form of *.unf* files but can be converted to NetCDF files, which are compatible with MATLAB, using a post-processing code. Each processing code, coordinating *.dat* files, and output files will be described in the upcoming sections. It is useful to run ELCOM through the command

line as opposed to the executable windows shortcuts, as the command window displays model results and any errors encountered during a simulation.

All ELCOM simulations required five basic steps: (1) creating a bathymetry file, (2) running a pre-processing code, (3) preparing temperature profiles to set the initial start-up stratification, (4) creating a file representing the environmental forcing conditions on the lake surface, (5) designating the model output, running a simulation, and post-processing. Each of the five steps will be outlined below as to the methods involved in running a simulation. Table 3.1 contains keywords used during the course of setting up and running ELCOM. Table 3.2 lists each file which is created, used by, or output by ELCOM. A set of example files for a simulation run in ELCOM are found in the Appendix.

Bathymetry

Bathymetric data is input into ELCOM in a *bathymetry.dat* file which is read by the pre-processing code *pre_elcom.exe*. The convention used when entering bathymetric data into ELCOM in (x ,y, z) space is z positive upwards, while x is positive down the page and y positive to the right when seen from above (Fig 3.3). The z = 0 m baseline can be set by the user, as long as the upward positive z convention is maintained.

Throughout all simulations, the baseline was selected as the water surface, with all depths given as negative values. The upper-left corner of the bathymetry file must contain the origin, i.e. (x, y) = (0, 0). Horizontal data can be represented with non-uniform spacing in each of the horizontal directions (x and y). That is, the grid size in the

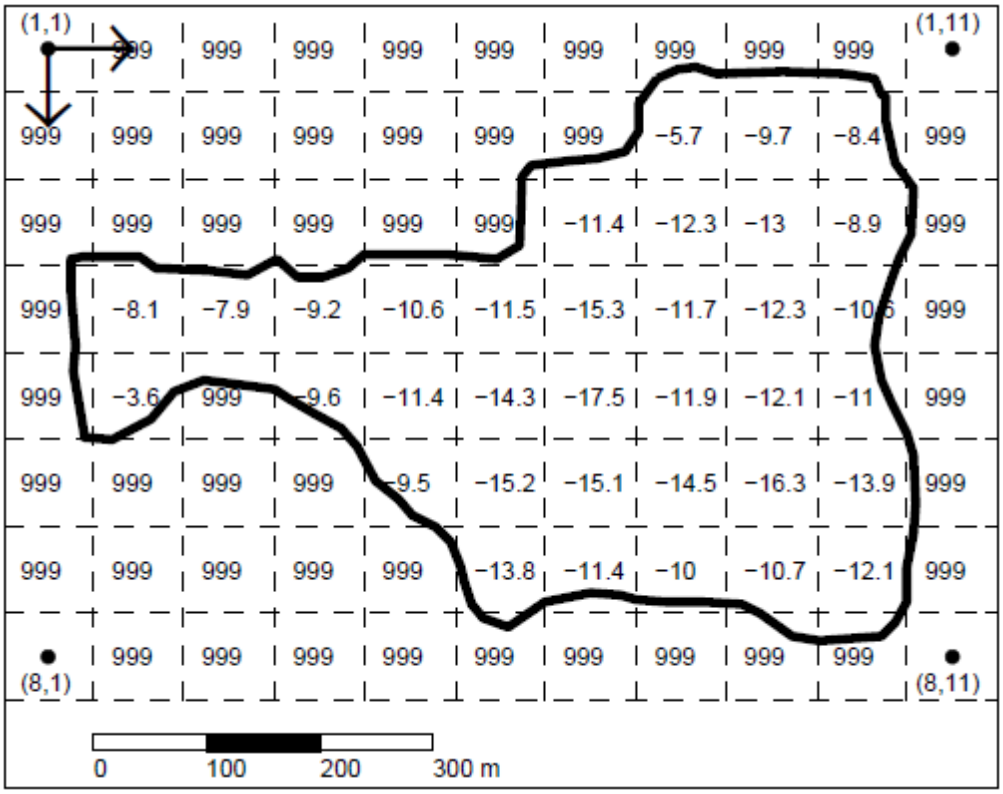

Figure 3.3. Bathymetric map of Ada Hayden Lake as represented on a grid pattern in ELCOM. Elevation values (in m) are shown as negative with $z = 0$ representing the water surface. Land values are given an elevation value of 999 to distinguish land cells from water cells. The upper left cell in the grid acts as the reference ($i = 1$, $j = 1$) with i increasing down the page, and j increasing across the page to the right. North is represented by the vector (-1, 0). The horizontal grid size in the figure is 80×80 m.

x-direction must be uniform, but it could differ from the constant grid size in the *y*-direction. However, the horizontal grid size was equal in each direction for all simulations.

The computational space–as well as the output data–is represented in (*i, j, k*) space. The *i, j,* and *k* values are integer indices of a three-dimensional array. Just as in real (*x, y, z*) space, (*i, j, k*) space also maintains the right hand rule, with non-zero,positive integers. Therefore, $k = 1$ is associated with the lowest cell layer (the lake bottom). The user provides the bathymetry data by designating the vertical distance measured from the $z = 0$ baseline for each cell. ELCOM differs from other data storage programs in that the origin is located in the upper-left corner, as opposed to the conventional mirror-image storage with the origin at the lower-left corner.

There are two cell qualifiers to keep in mind when setting up the *bathymetry.dat* file: land values and open values. A land value should be given to each cell which does not initially contain water. An open value is to be used when simulating an estuary or coastal ocean environment where the area is open to the ocean or similar body of water. Each cell within the *bathymetry.dat* file must contain one of three values: i) a vertical distance (m) corresponding to the basin depth, ii) a land value, or iii) an open value. The land value is typically listed as 999, and an open value is 888. These values do not correspond to 999 and 888 m above the baseline level; they merely signal that ELCOM will recognize these designated values and reserve these cells as land values and open values, respectively.

ELCOM's pre-processor code requires the number of rows in the *x*-direction, the number of columns in the *y*-direction, and the number of vertical layers in the *z*-direction.

If there is insufficient memory to process the bathymetry data, the initial number of grid cells can be estimated by providing a value for the keyword *n_max*. Otherwise, setting *n_max* = 0 will result with the code initiating a grid size of *x_rows* by *y_columns* by *z_layers*, and reducing the size by removing unused cells designated as land values. For all simulations, no estimates were made for the number of grid cells; minimum grid sizes were selected such that sufficient memory was available for processing.

Horizontal grid size is given by *x_grid_size* and *y_grid_size*, respectively, while the vertical grid size is given by the *dz* variable. ELCOM allows for changes in the vertical grid size by designating a structure of horizontal layers which can vary with depth. The layer thicknesses are entered in descending values from the top of the domain in a vector array. However, the selection of the vertical spacing does have some implications. Although any manner of vertical grid resolution is allowed, the simulation will provide the best accuracy using a grid of uniform thickness or one in which the changes in *dz* are gradual (Hodges and Dallimore, 2007). Therefore, each simulation was modeled using a uniform vertical grid size. The maximum depth of the lake was divided by *dz* and rounded up to not cut off part of the water column. An additional layer was added when required (for small values of *dz*) to account for changes in water level and to reproduce surface waves. At every model time step, ELCOM updates whether a cell is wet (contains water) or dry (does not contain water). In this way, there were no adverse effects from adding an additional vertical layer.

As wind forcing on the surface requires a direction, the direction of the north arrow is also required. Because of ELCOM's convention when defining the origin, a standard "north up" data set has a north vector of (-1, 0). The latitude, longitude, and

Table 3.1. Keywords used in ELCOM files. Keywords must exactly match as shown below.

Keywords	Description	Used in File
File	Identifies file	some *.dat* files
Title	File header	*bathymetry.dat*
Analyst	File header	*bathymetry.dat*
Organization	File header	*bathymetry.dat*
Comment	File header	*bathymetry.dat*
north_x	Defines North	*bathymetry.dat*
north_y	Defines North	*bathymetry.dat*
x_rows	Defines x-grid size	*bathymetry.dat*
y_columns	Defines y-grid size	*bathymetry.dat*
z_layers	Defines z-grid size	*bathymetry.dat*
n_max	Estimates number of grid cells	*bathymetry.dat*
dz	Defines horizontal layer thickness	*bathymetry.dat*
land_value	Defines cell land value	*bathymetry.dat*
open_value	Defines cel open value	*bathymetry.dat*
idensity	Stratification vs. passive tracers	*run_elcom.dat*
itemperature	Controls temperature as a scalar	*run_elcom.dat*
isalinity	Controls salinity as a scalar	*run_elcom.dat*
initial_profile_file	Designates an initial density profile	*run_elcom.dat*
met_file	Designates an environmental forcing file	*run_elcom.dat*
time	CWR time (yyyyddd.dd)	*met_file.dat*
wind_speed	Wind speed (m/s)	*met_file.dat*
wind_dir	Wind direction (° CW from north)	*met_file.dat*
solar_rad	Solar radiation (W/m^2)	*met_file.dat*
rel_hum	Relative humidity (0-1)	*met_file.dat*
air_temp	Air temperature (°C)	*met_file.dat*
profile_1D	Output cell set	*datablock.db*
curtain_2D	Output cell set	*datablock.db*
sheet_2D	Output cell set	*datablock.db*
all_3D	Output cell set	*datablock.db*
temperature	Output scalar water temperature (°C)	*datablock.db*
u_velocity	Output velocity in x-direction (m/s)	*datablock.db*
v_velocity	Output velocity in y-direction (m/s)	*datablock.db*
w_velocity	Output velocity in z-direction (m/s)	*datablock.db*

Table 3.2. ELCOM files. Exact filenames are not required as shown, descriptive names were simply chosen for clarity.

Files	Presence	Used by:	Generated by:
bathymetry.dat	required	*pre_elcom.exe*	User
bc.dat	required	*pre_elcom.exe*	User
update.dat	optional	*pre_elcom.exe*	User
run_pre.dat	required	*pre_elcom.exe*	User
DataOut.txt	output		*pre_elcom.exe*
sparsedata.unf	output	*elcom.exe*	*pre_elcom.exe*
usedata.unf	output	*elcom.exe*	*pre_elcom.exe*
initial_profile.dat	required	*elcom.exe*	User
boundary_condition.dat	required	*elcom.exe*	User
datablock.db	required	*elcom.exe*	User
run_elcom.dat	required	*elcom.exe*	User
elcom_out.unf	output	*dbconv.exe*	*elcom.exe*
dataconvert.dat	required	*dbconv.exe*	User
convert_out.nc	output		*dbconv.exe*

altitude of the simulation can be specified, where values reference the origin cell. The latitude is used to provide Coriolis forces, while the longitude and altitude do not enter into any calculations. Latitudes in the northern hemisphere are positive, and simulations occurring in the southern hemisphere will use negative latitude values.

The *bathymetry.dat* file requires a file header for proper processing. The first non-comment line of the file must begin with the keyword *File*, followed by the name of the bathymetry file (e.g. *bathymetry.dat*). The next four lines are reserved for a description of the file and are read by ELCOM in *keyword; 'string'* notation. There are four *keywords*: *Title*, *Analyst*, *Organization*, and *Comment*. The *string* associated with each *keyword* must contain non-null characters and enclosed in single quotation marks.

If the *string* is left empty, the pre-processer will crash. The file must have only one *Comment* line. The information provided in the file header will be printed to the output file and at the beginning of the start of the simulation run. The bathymetry section must be completely filled with data; there can be no missing elevation values.

Bathymetry data for Ada Hayden Lake and West Okoboji Lake were provided in two different forms. Data for Ada Hayden Lake were obtained by combining depth measurements from a Lowrance 520C 200 kHz sonar with 10 cm resolution and a WAAS-enabled hemisphere R100 GPS unit with 60 cm resolution, each sampling at 0.25 Hz frequency using LabVIEW. Depth and position data were linearly interpolated to provide a suitable grid for ELCOM. Data for West Okoboji Lake were obtained through the Iowa Department of Natural Resources with a horizontal resolution of 15 m.

The horizontal and vertical grid resolutions were modified for each simulation event. For a simulation, the horizontal and vertical measurements were linearly interpolated onto a suitable grid size. The model grid sizes and time steps were varied for each particular event, with changes being made in the horizontal (Δx) and vertical (Δz) grid size, as well as the model time step (Δt). After Hodges et al. (2006), model simulations were run at efficient time steps with the Courant-Friedrichs-Lewy (*CFL*) number held fixed at 1/3, where the *CFL* number is applied to baroclinic motions as

$$CFL = c_n \frac{\Delta t}{\Delta x} = \frac{1}{3} \tag{3.1}$$

where c_n is the phase speed of the V1H1 internal wave. The V1 wave was selected as it propagates with the highest phase speed. Therefore, the *CFL* number will be highest for V1H1 seiche, assuring stability for seiches with a higher number of vertical modes. The vertical grid size does not enter (3.1), leaving a relationship between Δx and Δt based on the phase speed of an internal wave. Therefore, given a horizontal model grid size and phase speed, the model time step was determined explicitly from (3.1).

Pre-Processing

The pre-processing code *run_elcom.exe* is paired with a *run_pre.dat* file which contains the names and locations of required bathymetry files. ELCOM uses four input files and three output files in the pre-processing code. The input files consist of i) a bathymetry file *bathymetry.dat*, ii) a boundary condition file *bc.dat*, iii) a boundary condition update file *update.dat*, and iv) a data file *run_pre.dat* which is associated with the pre-processing code. Three input files are required for the pre-processor code: *bathymetry.dat*, *bc.dat*, and *run_pre.dat*, while the *update.bc* file is optional. The bathymetry file was previously discussed concerning the syntax and setup involved. The boundary condition file designates cell sets for various conditions such as river infow/outflow, groundwater inflows, or a bubble plume. While required, the boundary condition file was left empty because Ada Hayden Lake and West Okoboji Lake were modeled as closed basins. The boundary condition update file allows arbitrary modification in scalar values (e.g., a tracer release). No tracer studies were modeled using ELCOM; therefore, the *update.dat* file was not used. The file *run_pre.dat* is

required for the pre-processing code and contains names and locations of input/output files used by *pre_elcom.exe*.

Output directories should correspond to the *infiles* directory used by the processing code. The setup of the processing code will be discussed in a later section. The output files for the pre-processing code consist of one text file and two unformatted files: i) data output text file, ii) *usedata.unf*, and iii) *sparsedata.unf*. The data output text file contains pre-processing results and is generally not important for the model simulation. However, the *usedata.unf* and *sparsedata.unf* files are required for *elcom.exe* processing as they contain bathymetry data given by the pre-processing code. The directory associated with the output of the pre-processing code must coordinate with specified directories in the main processing code. Once all pre-processing files are complete and placed in locations designated by *run_pre.dat*, the next step is to run the pre-processing code. Running the pre-processing code is accomplished by executing *pre_elcom.exe* at the command line.

Temperature Profiles

The initial conditions for the temperature structure in the lake can be specified through the use of vertical profiles. Density stratification in ELCOM can be through salt, temperature, or both, and is controlled using the keywords *idensity* in conjunction with *itemperature* and *isalinity*. Setting *idensity* = 1 enables density stratification, while setting *idensity* = 0 will allow for temperature and salinity to be treated as passive tracers (i.e., eliminating the density term from the momentum equations). Initial conditions can

be specified with any number of input files identified by ELCOM using the keyword *initial_profile_file*. Because all simulations were for freshwater lakes and stratification is attributed solely to temperature, *itemperature* and *idensity* were each set to1, while *isalinity* was set to 0. Multiple input files were used to provide initial conditions, where these files were generated using field data from the thermistor chains.

The vertical profile input files require a format consisting of four header lines followed by columns of data. The first line in the file header includes the number of data sets (columns) in the initial profile, not including the depth column. The second line in the file header provides the number of rows containing data. The third header line contains the horizontal location of the profile, given in the (*i, j*) coordinate system. The fourth line contains keywords which correspond to the data provided in each of the columns. Depth values are required in the first column, while other data is required to be an ELCOM valid transportable scalar (i.e., salinity, water temperature, or a tracer concentration). Therefore, the first keyword in the fourth line must be *depth* followed by *wtr_temp* for the case of temperature-stratification.

The depth values in the first column started at zero and increased monotonically (depth is defined as vertically downward), while the temperature values in the second column were determined from field measurements. ELCOM linearly interpolates the initial data given in the vertical profile files onto the grid given by the bathymetry data. Horizontal interpolation is done for multiple profiles using the inverse distance weighting method, given by Hodges and Dallimore (2007):

$$S_{i,j,k} = \sum_{n=1}^{N} \frac{S_{n,k} r_n^{\alpha}}{\sum_{m=1}^{N} r_m^{\alpha}} \tag{3.2}$$

where $S_{i,j,k}$ is the interpolated scalar value at (i, j, k), $S_{n,k}$ is the scalar value given for the n^{th} profile at vertical position k, r_n is the distance between the column and profile n, α is the distance weighting parameter (default = 2.0), and N is the number of profiles. Simulations were initialized with two or three vertical profiles, and interpolation was done using the default value for α.

Input data for all *initial_profile_files* were supplied by thermistor chain measurements for both Ada Hayden Lake and West Okoboji Lake simulations. Temperature values at each depth were time-averaged over a 10 min period prior to the simulation start time. Temperatures were averaged to reduce any influence high frequency oscillations would have on the model performance. The thermistor chains did not measure at the water surface, corresponding to zero depth for the input files; the first node generally was at a depth of approximately 1 m or less. Examination of the temperature profile showed a well-mixed epilimnion, such that there should be negligible temperature differences between the water surface and the depth measured by the first thermistor node. Therefore, the temperature reading from the first node was also used for the water surface to give values at zero depth.

Because the grid resolution was altered in each of the simulations, the maximum depth at the thermistor chain locations changed slightly as a result of the interpolation method used in MATLAB. The temperature profile was therefore only given for depth values within the lake boundary set by the cell grid input into ELCOM. Any temperature

measurements at depths greater than the equivalent grid location were not input into the model. As the grid resolution was reduced (i.e., the horizontal spacing increased), the bottom boundary at each cell was interpolated over more points. This interpolation resulted in maximum depths that would decrease with increased horizontal grid sizes.

Environmental Forcing

ELCOM incorporates environmental forcing conditions by data given in temporal boundary condition files (*met.dat*). These one-dimensional files designate environmental conditions at a particular point, if multiple files are used, or for the entire free surface in the case of one boundary file. ELCOM recognizes many data types within a boundary condition file and the data supplied are required for each instant in time. For all simulations, five data types (other than time) were input into ELCOM: wind speed, wind direction, relative humidity, solar radiation, and air temperature. Simulations at Ada Hayden Lake used field measurements from the LDS for all data types. However, the temperature probe malfunctioned while in the field during deployment at West Okoboji Lake. The Iowa Great Lakes Water Safety Council has a weather station located at the Gull Point State Park which was used to supply air temperature values at 15 min intervals. These 15 min values were linearly interpolated to correspond with the sampling frequency of the LDS to provide accurate temperature values.

The boundary condition file requires a file header designating the number of data sets and the type of data used. The first line contains the number of data sets within the file not including the time values. The second line should contain the number 0, which

indicates CWR time format is being used. The third line requires integer values for each data column designating the location of the boundary condition file. For boundary conditions applied to the entire surface, these integer values should all be set to 0. The fourth line contains keywords that describe the data set in each column. The first keyword should be *time*, as time values are required in the first column. See Table 3.1 for a list of keywords and the appropriate units.

The data in the boundary condition file are organized into columns, with the first column containing time in CWR format (yyyyddd.dd). Each successive column contains data for a respective data type, and each row contains data values for the respective time step. The time interval used in the boundary condition file is not required to correspond with the model time step; ELCOM will linearly interpolate the input data values onto a suitable time grid. Within the data columns, missing data values will cause the code to crash; each row must have the appropriate number of data values to correspond with the number of columns.

Designating Model Output, Running Simulations, and Post-Processing

ELCOM provides a number of data output options. Output information is designated in a *datablock.db* file, which is organized into series of blocks. The first four lines of the *datablock.db* file are the datablock descriptions, including the ELCOM version number, the number of output groups, and the number of output sets. Output groups identify a group of data to be output, such as temperature, velocities, etc. The output sets specify points (cells) at which data are to be output. Output cell sets can be

either one-dimensional profiles, a continuous series of columns (curtains), a horizontal series of cells (sheets), or the entire domain. Table 3.1 contains the keywords associated with each type of output cell set types and scalar types. There are 11 lines in each group description and 16 lines for each set description. As the cell set type changes, values will change for 'sheet type', 'sheet calc', 'sheet value', and the 'cell location' lines. For a complete description of the options and requirements for a datablock file, see Hodges and Dallimore (2007).

ELCOM is executed at the command line by typing *elcom.exe* in the appropriate directory. ELCOM will send monitoring information to the command line, which will show any errors during a simulation. Once the model is complete, post-processing of the *elcom_out.unf* files is required. The post-processing code *dbconv.exe* converts the model output into NetCDF *convert_out.nc* files which are compatible with MATLAB. The post-processing code requires *.dat* files which specify.*unf* filenames and locations, as well as the name and location of the converted *.nc* file. Running the post-processing code is done by typing *dbconv.exe* at the command line in the *unf* directory of ELCOM.

Description of Numerical Methods

ELCOM's numerical scheme is adapted from the TRIM approach (Casulli and Cheng, 1992). The approach uses an Arakawa C-grid stencil, which defines velocities on cell faces, while the free surface height and scalar concentrations are defined on cell centers. ELCOM uses a semi-implicit method where the water surface gradient, the velocity in the free surface equation, and the vertical mixing terms are discretized

implicitly. The advective, Coriolis, and horizontal viscosity terms in the momentum equations are discretized explicitly. A brief description of the numerical method used by ELCOM will be presented. For more details, see Casulli and Cheng (1992), Hodges et al. (2000), and Hodges and Dallimore (2006).

Momentum Discretization

ELCOM solves the velocity field in a manner similar to the TRIM approach given by Casulli and Cheng (1992), with the addition of a vertical mixing model and the use of a hybrid linear/quadratic Eulerian-Lagrangian method. The momentum equations in the x and y directions are

$$U_{i+1/2,j}^{n+1} = \left(A_{i+1/2,j}^{n}\right)^{-1} G_{i+1/2,j}^{n} - g\frac{\Delta t}{\Delta x}\left(\eta_{i+1,j}^{n+1} - \eta_{i,j}^{n+1}\right) \tag{3.3}$$

$$V_{i,j+1/2}^{n+1} = \left(A_{i,j+1/2}^{n}\right)^{-1} G_{i,j+1/2}^{n} - g\frac{\Delta t}{\Delta y}\left(\eta_{i,j+1}^{n+1} - \eta_{i,j}^{n+1}\right) \tag{3.4}$$

where U and V are matrices containing the velocities at location (i, j) and η is the free surface height. Subscripts i, j, k refer to cell locations and superscript n refers to time. G is an explicit source term and A is a matrix defined as

$$A = \begin{bmatrix} b_n + \gamma_k & c_n & 0 & \cdots & 0 \\ a_{n-1} & b_{n-1} & c_{n-1} & \ddots & \vdots \\ 0 & a_{n-2} & b_{n-2} & \ddots & 0 \\ \vdots & \ddots & \ddots & b_2 & c_2 \\ 0 & \ldots & 0 & a_1 & b_1 + \gamma_1 \end{bmatrix} \tag{3.5}$$

where the γ_k terms are set by ELCOM to correspond to boundary conditions (e.g., no-slip, free-slip, Neumann, etc.), while the *a*, *b*, and *c* terms are given by

$$b_k = -a_k + \Delta z_k - c_k \tag{3.6}$$

$$a_k = -\left.\frac{\nu_3 \Delta t}{\Delta z}\right|_{k+1/2} \tag{3.7}$$

$$c_k = -\left.\frac{\nu_3 \Delta t}{\Delta z}\right|_{k-1/2} \tag{3.8}$$

where ν_3 is the viscosity in the *z*-direction, Δt is the model time step, and Δz is the vertical grid size. The source terms in G are given by

$$G_{i+1/2,j} = I\left(\tilde{U}_{i+1/2,j}\right) - \Delta t\left\{C^n_{i+1/2,j} + D_x\left(\tilde{U}\right)_{i+1/2,j} + D_y\left(\tilde{U}\right)_{i+1/2,j} - f\tilde{V}_{i+1/2,j}\right\} \tag{3.9}$$

$$G_{i,j+1/2} = I\left(\tilde{V}_{i,j+1/2}\right) - \Delta t\left\{C^n_{i,j+1/2} + D_x\left(\tilde{V}\right)_{i,j+1/2} + D_y\left(\tilde{V}\right)_{i,j+1/2} - f\tilde{U}_{i,j+1/2}\right\} \tag{3.10}$$

where the I operator represents advective discretization, C represents baroclinic discretization, and $D_{x,y}$ represents horizontal turbulent diffusion discretization in the x and y direction, respectively. ELCOM uses a vertical mixing model to account for vertical diffusion, where the mixing operator M is defined as

$$\tilde{U}_{i,j,k} = M\left(U^n_{i,j,k}\right) \tag{3.11}$$

ELCOM uses a second-order stencil for the discretization of the horizontal diffusive terms, the diffusive term in the *x*-direction is given as

$$D_x\left(S^n_{i,j,k}\right) = \frac{\nu}{\Delta x^2}\left(S^n_{i+1,j,k} - 2S^n_{i,j,k} + S^n_{i-1,j,k}\right) \tag{3.12}$$

where S is any scalar. The baroclinic discretization term C is defined as

$$C^n_{i+1/2,j,k} = \frac{g}{\rho_0 \Delta x}\left\{\sum_{m=k}^{F} \rho'_{i+1,j,m} - \sum_{m=k}^{F} \rho'_{i,j,m}\right\}$$

where ρ' is the density perturbation from the reference value, and $k = F$ is the cell containing the free surface. The free surface discretization is given by

$$\eta^{n+1}_{i,j} = \eta^n_{i,j}\left[\frac{\Delta t}{\Delta x}\delta_x\left\{\left(\Delta Z^n\right)^T U^{n+1}\right\} - \frac{\Delta t}{\Delta y}\delta_y\left\{\left(\Delta Z^n\right)^T V^{n+1}\right\}\right] \tag{3.13}$$

where ΔZ is a vector containing the vertical grid size, and the operators δ_x and δ_y indicate discrete differences, such that $\delta_x\left(S\right) = S_{i+1/2} - S_{i-1/2}$.

The TRIM method (Casulli and Cheng, 1992) uses a linear Eulerian-Lagrangian method for the discretization of the advective and viscous terms. ELCOM uses a hybrid method which is a combination of the linear Eulerian-Lagrangian method for $CFL > 2$,

and a quadratic Eulerian-Lagrangian method for $0 < CFL < 2$. The reason for using two methods is that the linear method can be compromised by numerical diffusion, while the quadratic method requires greater computation. The linear Eulerain-Lagrangian method is essentially a three-dimensional upwind discretization scheme, while the quadratic Eulerian-Lagrangian method uses a 27-point upwind stencil. The quadratic stencil used in the Euler-Lagrange interpolation reduces artificial damping of internal waves that occurred using the linear stencil (Hodges, 2000).

Scalar Transport

ELCOM calculates scalar concentrations *C* in three stages: vertical mixing, advection, and horizontal diffusion. Vertical mixing by the Reynolds stress is given by

$$\tilde{S} = M\left(S^n\right) + S^{(C)} \tag{3.14}$$

where $S^{(C)}$ provides scalar sources. Scalar advection due to the velocity field is given by S^*, defined as

$$S^* = \tilde{S}C - \Delta t \frac{\partial}{\partial x_j}\left(\tilde{S}U_j\right) \tag{3.15}$$

where S^* is calculated over the timestep Δt. However, if $CFL > 1$, ELCOM uses a sub-time step δt, where $m\delta t = \Delta t$ and m sub-time steps are used in order to avoid numerical instabilities. Horizontal diffusion by turbulent motions is then given by

$$S^{n+1} = S^* + \frac{\partial}{\partial x_\alpha}\left\{\kappa \frac{\partial S^*}{\partial x_\alpha}\right\} + O\left(\Delta t^2\right) \tag{3.16}$$

where $O\left(\Delta t^2\right)$ is a truncation error which is second order accurate in time. ELCOM uses the Universal Limiter for Transient Interpolation Modeling of the Advective Transport Equations Quadratic Upstream Interpolation for Convective Kinematics (ULTIMATE QUICKEST) method (Leonard, 1991) for the interpolation of scalar concentrations from the cell center (where they are defined) to cell faces for use of discrete difference operators δ_x and δ_y.

Mixing Model

The vertical mixing model accounts for vertical diffusion in the model, while horizontal diffusion is calculated using a finite-difference approach. The vertical mixing model in ELCOM uses a mixed layer approach, as opposed to the traditional method of using differential equations coupling layer thickness, entrainment rates, and heat transfer. ELCOM models the vertical Reynolds stress terms in the momentum and transport equations three-dimensionally, expanding on previous one-dimensional models (e.g., Imberger and Patterson, 1981; Spigel et al., 1986; Imberger and Patterson, 1990). The mixed-layer approach dynamically defines a "mixed layer" as a vertical set of cells sharing the same density, scalar concentrations, and grid-scale velocity (Hodges, 2000). The mixed layer method showed a bias for downward entrainment and mixing, as the model is applied down the water column from the water surface to the lake bottom (Hodges et al., 2000).

A mixing time step is broken into 12 steps: 1) calculate wind energy input, 2) calculate bottom energy input from the turbulent bottom boundary layer, 3) for each column, cycle vertically from the surface to the bottom cell, 4) calculate generation of turbulent kinetic energy (TKE) by shear, 5) calculate energy required for mixing, 6) calculate total energy available if two cells mix completely, 7) calculate time for complete mixing, 8) if unstable, calculate time estimate based on convective overturn, 9) calculate mixing fraction, 10) if sufficient energy, mix the cells, 11) end cycle at bottom cell, and 12) dissipate excess mixing energy.

Data Analysis of Field Work and Model Results

Dimensionless variables such as the Wedderburn number W and the Lake number L_N integrate factors such as stratification, basin size, and forcing conditions into a single estimate. When considering forcing conditions, it is important to accurately account for the transfer of momentum (or energy) from wind shear to internal lake dynamics as part of the energy flux path as described by Imberger (1998). For seasonal field measurements, Stevens & Lawrence (1997) demonstrated that energy transferred at frequencies greater than $4 / T_i$ cannot affect baroclinic motions (where T_i is the period for the V*i*H1 mode seiche), but instead affects surface layer circulation, contributes to turbulent kinetic energy, or is immediately dissipated. Filtering attenuates peaks in the velocity, but it is required for wind events that are not constant in magnitude (Stevens & Lawrence, 1997). Therefore, all wind data were filtered using a fourth order Butterworth

filter with a cutoff frequency corresponding to one-quarter of the period for the V1H1 internal wave when calculating W and L_N.

To quantify model performance and compare simulations at different resolutions, three physical attributes were evaluated between field observations and model output: i) the frequencies of internal motions, ii) the retention of the temperature structure under forcing conditions, and iii) internal wave amplitudes. The first attribute will be used primarily to indicate the model's ability to reproduce internal motions across a wide range of frequencies. Because ELCOM is a hydrostatic model, nonlinear effects (i.e., non-hydrostatic pressures) associated with higher frequency motions cannot be physically represented by the model. The second point is important as it can indicate whether excessive numerical diffusion is acting to erode the thermocline and will therefore help to quantify numerical error in the model. The third item aims at addressing whether equal forcing conditions given to ELCOM will reproduce internal motions comparable to field observations. Additionally, a nondimensional number known as the Willmott skill will be used to quantify model predictions.

Hydrostatic models have shown to be able to reproduce basin-scale motions, but they are unable to resolve high-frequency motions due to restrictions on grid cell sizes (e.g., Hodges et al., 2000; Gomez-Giraldo et al., 2006; Botelho and Imberger, 2007; Yeates et al., 2008). Once the isotherm displacements are calculated at the thermistor chains, Welch's periodogram method can used to calculate the spectral density of an isotherm's displacement in frequency space. When computing power spectra, standard default methods given using the MATLAB build-in function *pwelch* were used. Equal weighting was given to each time measurement (segment), and a 50% overlap was used

between segments. The fast Fourier transform was determined as the larger of either the length of the data segment or 256. Power spectra can be created for each isotherm and at each thermistor chain, where the power spectrum gives the power of the signal at a particular frequency. In the case of periodic motions, peaks in the power spectra typically correlate with seiching mode frequencies.

Normalized Potential Energy

The potential energy in the water column is calculated to assess the model's ability to retain the thermocline's temperature structure over a simulation. The advantage to this approach is that the potential energy does not rely upon selecting a single isotherm to represent the entire time series (Antenucci et al., 2000). Winters et al. (1995) defined the potential energy within a fluid using a volume integral; however, here the potential energy is evaluated in the water column as opposed to the entire water body. The potential energy E_P (per unit area) is defined as

$$E_P(t) = g\int_{z_0}^{H} \rho(z,t)\, z dz \tag{3.17}$$

where z_0 is the elevation of the lake bottom, and z is defined as positive upwards. A time-series of potential energy is calculated from both field data and model output. However, values for potential energy are typically $O(10^6)$ kg/s^2 and they only by vary $O(10^2)$ kg/s^2 ; therefore, the change in potential energy from a reference value was

evaluated. Also, by evaluating changes in potential energy as opposed to the total value, results can be obtained which aim to evaluate the model's ability to reproduce changes in the temperature structure over a set time period.

The reference value was defined using the difference between the initial and minimum potential energy values calculated from field measurements. This definition was made because of the difference in magnitudes of potential energy values across simulations of different vertical grid sizes. The potential energy reference value $E_{P,0}$ for each model run is then defined as

$$E_{P,0} = E_{P,\text{model}}(0) - \left[E_{P,\text{field}}(0) - \min\left(E_{P,\text{field}}\right) \right] \tag{3.18}$$

where $E_{P,\text{model}}(0)$ is the initial potential energy value calculated using model output and the value in brackets is the reference potential energy difference based on field data $E_{P,\text{field}}$. Initial potential energy estimates based on model results were within $\pm$ 10% of the values calculated from field observations. While this difference is important, the effects of numerical error in the model affect the change in potential energy of the simulation period. The fluctuations in potential energy are then found by subtracting the reference value from the model results

$$\Delta E_P = E_{P,\text{model}} - E_{P,0} \tag{3.19}$$

To compare the potential energy values across different simulations, a time-integrated value for potential energy is calculated. By integrating ΔE_P over time, a single potential energy value can be obtained for each model run. The time-integrated potential energy values calculated from model results are normalized by the value obtained from the field data to give a dimensionless value for potential energy E_P', defined as

$$E_P' = \frac{\int \Delta E_P dt}{\int \left[E_{P,\text{field}} - \min\left(E_{P,\text{field}}\right) \right] dt} \tag{3.20}$$

The advantage to using E_P' is that results are easily analyzed. $E_P' > 1$ indicates a higher center of mass, caused by either numerical diffusion or the model overestimating mixing. $E_P' < 1$ would be the result of isotherms deepening in the model, lowering the center of mass.

Normalized Kinetic Energy

To evaluate the model's ability to reproduce internal wave amplitudes, kinetic energy is calculated based on field data and model output. Here, kinetic energy will be based on the vertical velocity w, omitting horizontal velocities u and v. The reason for defining kinetic energy using only the vertical velocity lies in the difficulty in estimating horizontal velocities from thermistor chain measurements. ELCOM can output values for

the velocity vector (u, v, w) directly, but estimating w based on thermistor chain measurements is done by tracking isotherm movements. Isotherm positions are found by linearly interpolating temperature data from the thermistor chains. Because the top and bottom of the water column are less stratified than the metalimnion (it is not uncommon for the epilimnion to be completely mixed), it can be difficult to achieve accurate isotherm depths using a linear interpolation method in these regions. Therefore, the analysis is limited to the thermocline region.

Once the isotherm positions are determined, *w* is defined simply as the time derivative. The depth-integrated kinetic energy is defined after Winters et al. (1995) as

$$E_K(t) = \frac{\rho_0}{2} \int_{z_1}^{z_2} w(t)^2 \tag{3.21}$$

where ρ_0 is a reference density, and the bounds z_1 and z_2 are defined as the top and bottom of the metalimnion, respectively. When comparing field observations to model output, a similar metalimnion thickness—or constant values for z_1 and z_2—were used. As in the expression for potential energy, *z* is defined as positive upwards. The time series of kinetic energy values are analyzed similar to potential energy by integrating in time and normalizing model results by field data estimates to provide a dimensionless value of kinetic energy E_K', defined as

$$E_K{}' = \frac{\int\int_{z_1}^{z_2} w_{\text{model}}^2 dzdt}{\int\int_{z_1}^{z_2} w_{\text{field}}^2 dzdt} \tag{3.22}$$

where w_{model} is the vertical velocity given by ELCOM and w_{field} is the vertical velocity based on isotherm depths from field data. Both velocities are functions of depth and time.

Willmott Skill Number

Additionally, a nondimensional number has been proposed which compares a physical parameter between field and model results, known as the Willmott skill WS (Willmott and Wicks, 1980; Willmott, 1981), defined as

$$WS = \frac{\sum\left(X_{\text{model}} - X_{\text{field}}\right)^2}{\sum\left(\left|X_{\text{model}} - \bar{X}_{\text{field}}\right| + \left|X_{\text{field}} - \bar{X}_{\text{field}}\right|\right)^2} \tag{3.23}$$

where X_{model} is a parameter based on model results, X_{field} is a corresponding parameter from field observations with time average $\bar{X}_{\text{field}}$. WS is a nondimensional number ranging from zero to one, where a value of one indicates perfect agreement and zero yields complete disagreement (Warner et al., 2005). The Willmott skill number can therefore be used to compare results from different parameters in the same simulation or different models directly with one another.

Willmott (1982) evaluated evapotranspiration models and found WS values of 0.82 and 0.90 using the Makkink and Blaney-Criddle models, respectively. Warner et al. (2005) estimated the performance of the Regional Ocean Modeling System (ROMS) using the Willmott skill number and found WS values of 0.85 and 0.95 for sea level at two different locations in a model, 0.92 for depth-averaged velocities, and 0.85 for salinity concentrations. Wilkin (2006) used ROMS to model ocean circulation near Cape Cod, Massachusetts and found WS values between 0.2 and 0.8 in comparing observed and modeled temperatures at different instrument locations. Liu et al. (2009) used ROMS in the River Influence on Shelf Ecosystem (RISE) project at the mouth of the Columbia River in Washington and calculated WS numbers for velocities, temperatures, and salinities in the top and bottom of the water column and near the river discharge (nearfield) and offshore (farfield). The regions were combined by averaging WS values, giving average values ranging from 0.48 to 0.97. For the model analysis of this work, Willmott skill numbers were calculated using the depth of an isotherm near the center of the metalimnion.

Summary

Chapter 3 identified the methods for conducting field observations and the procedure for implementing a three-dimensional hydrostatic model, and it presented dimensionless variables used to quantify and assess model performance. Instrument locations have been identified for three years of field work in two lakes. Also, sampling strategy and explanations involved when planning field studies were presented. Steps

were presented which outline the necessary elements for a successful simulation using ELCOM. The model grid sizes and time steps used for individual model runs, as well as the details of a particular simulation, will be presented in Chapter 4 following field analysis.

Two dimensionless energy variables have been defined based on potential and kinetic energy. These variables can be used to quantify model performance in terms of retaining the temperature structure and reproducing internal wave amplitudes. A perfect model simulation would return values of one for each of the variables. Also, a nondimensional number has been described which can be used to compare the agreement between model predictions and field observations. However, it will be shown in Chapter 4 that results will vary considerably from a perfect solution.

CHAPTER 4: RESULTS AND DISCUSSION

Introduction

Chapter 4 discusses the results from the field work and numerical modeling. Field results will be discussed in terms of their significance for generating basin-scale internal motions. Additionally, dimensionless energy variables developed in Chapter 3 will show the applicability of three-dimensional hydrostatic modeling. Model results will be presented, analyzed, and model performance will be quantified using dimensionless energy variables defined in Chapter 3.

Field Results

The conducted field work consisted of measuring temperature stratification by deploying several thermistor chains at various locations across the lake. Additionally, environmental forcing conditions were measured to determine the effects forcing has on the internal motions of a lake. Forcing parameters include wind speed and direction, solar radiation, air temperature, and relative humidity. The measured conditions will be analyzed in terms of the likely mechanisms involved in the energy flux path and the ability of a hydrostatic model to capture these mechanisms.

Ada Hayden Lake

Wind and temperature data measured from the Lake Diagnostic System (LDS) from 17 July to 1 October are shown in Figure 4.1. There are several days which experienced high winds (between 10 and 15 m/s), most notably the 18th and 26th of July, the 28th of August, and the 18th of September. More sustained wind gusts of lesser magnitudes (between 5 and 10 m/s) were experienced the 5th and 26-27th of August. Strong gusts tend to originate from the north, while calmer, more sustained winds tend to emerge from the southwest or southeast (Fig. 4.1(b)). To relate the wind forcing to the lake's stratification, the Lake number is shown to vary considerably throughout the summer from low values approaching $O(1)$ to higher values exceeding $O(10^2)$.

Measurements are shown from mid-July through the end of September, depicting the change in stratification during the summer months. As shown in Fig 4.1d, the isotherm depths begin to increase until 16 September, when air temperature (not shown) begins to decrease, halting the mixed-layer deepening. Only isotherms which are present throughout the depicted time are shown to relate internal response to external forcing. The strong stratification during the summer months leads to small isotherm displacements under observed wind forcing.

Figure 4.2 shows field results from Ada Hayden Lake in 2008, encompassing measured conditions between 22 July and 1 October. In general, conditions in 2008 depict comparable wind conditions to those observed in 2007. Similar to situations experienced in 2007, high winds could be considered exceeding 10 m/s, while more sustained winds of interest also typically exceed 5 m/s. High wind occurred on 27 and 29

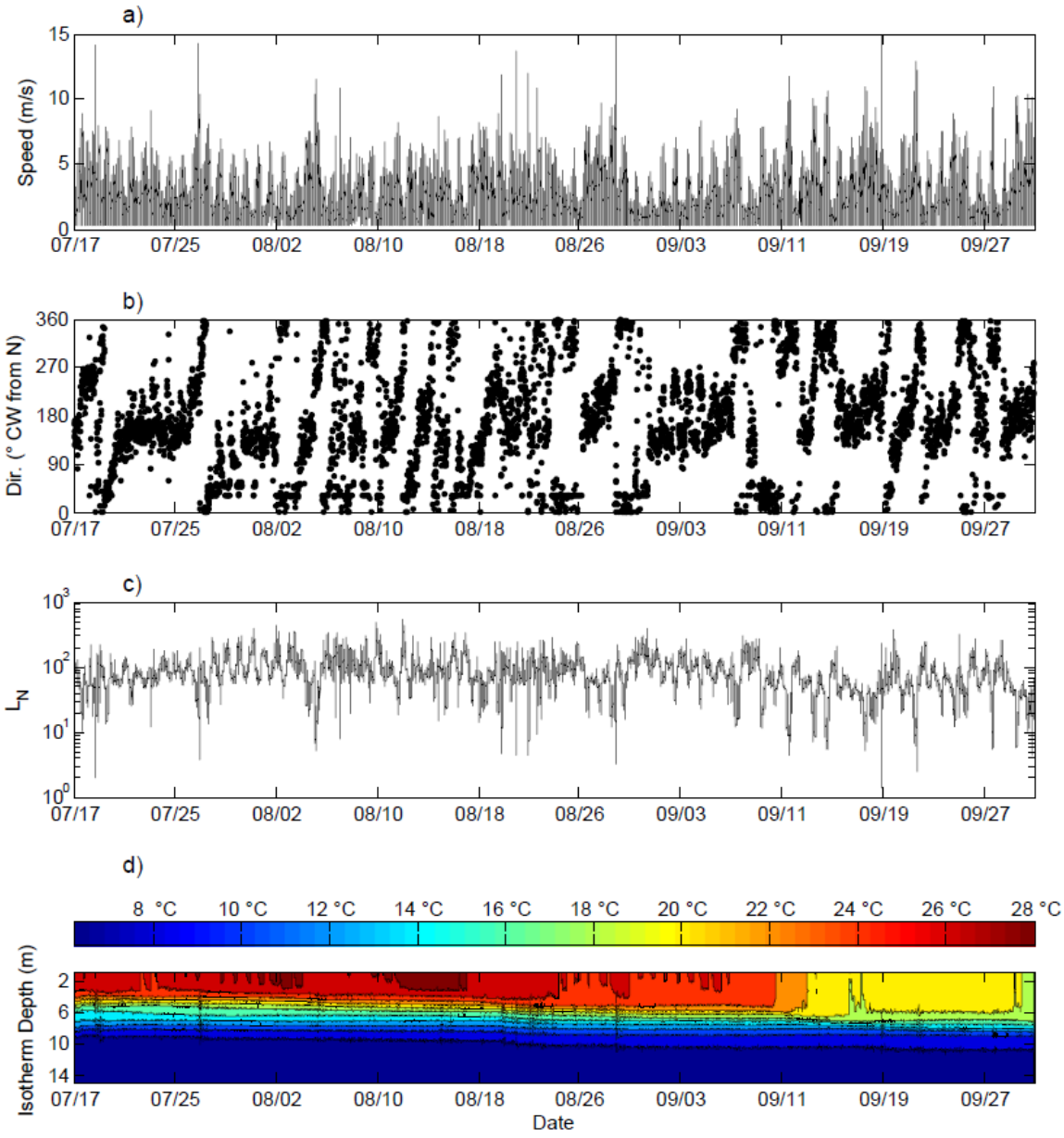

Figure 4.1. Field results from Ada Hayden Lake in 2007, as measured by the LDS: (a) wind speed measured at 2.40 m above the water surface, (b) wind direction (°) measured clockwise from north (0°), (c) Lake number calculated using filtered wind speed and temperature data from the LDS, (d) contour plot showing isotherm depths for even isotherms between 8 and 28°C.

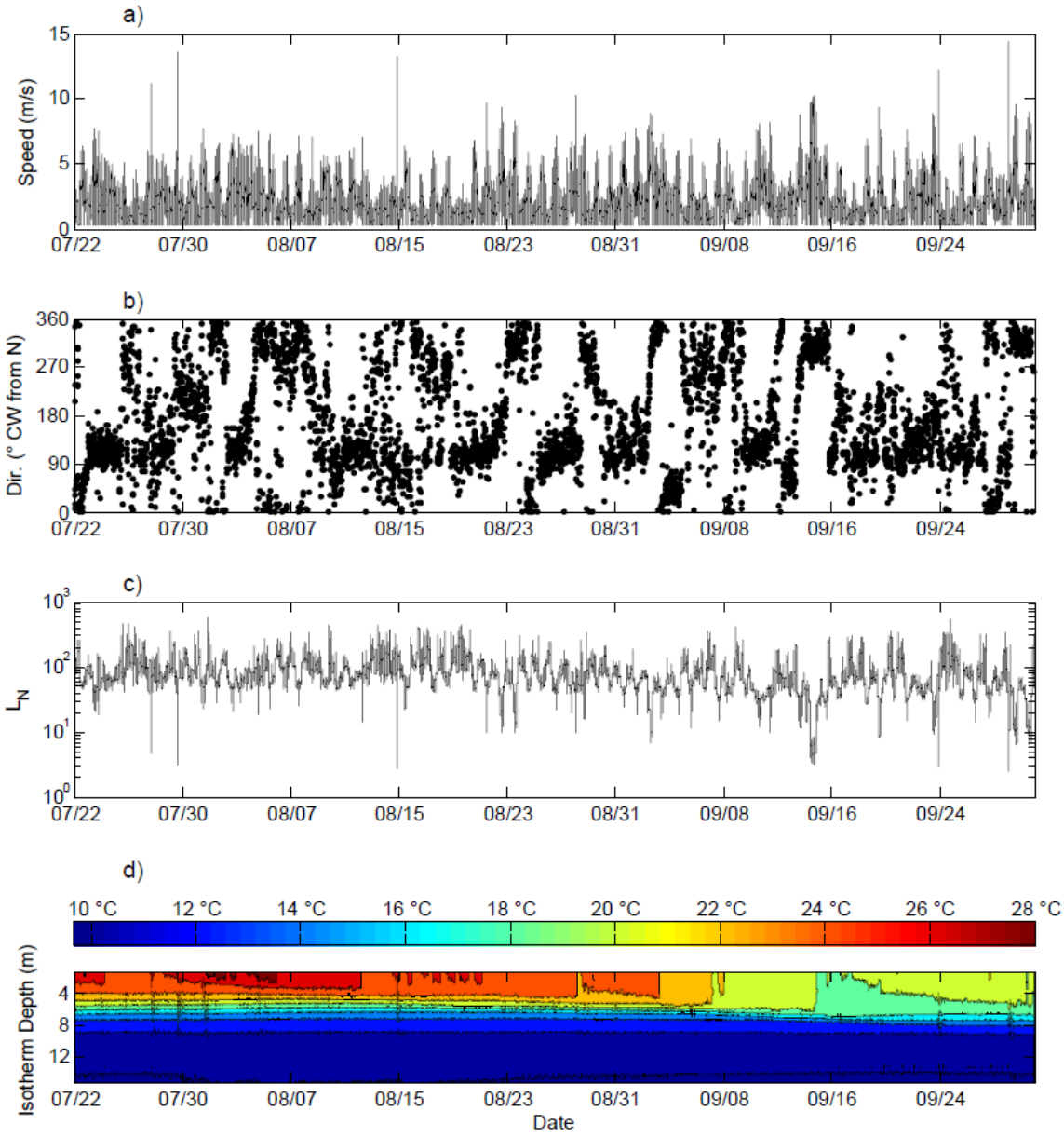

Figure 4.2. Field results from Ada Hayden Lake in 2008, as measured by the LDS: (a) wind velocity (m/s) measured at 2.10 m above the water surface, (b) wind direction (°) measured clockwise from north (0°), (c) Lake number calculated using filtered wind speed and temperature data from the LDS, (d) contour plot showing isotherm depths for even isotherms between 10 and 28°C.

July, 14 August, and 23 and 29 September, with corresponding low Lake numbers and large internal isotherm movement. More sustained conditions of lower magnitude are more frequent and can be seen on 23 and 31 July, 4 and 22 August, and 2, 14, and 19 September. These times are shown to experience moderate Lake numbers but typically not dropping much below a value of 10. Similar to the high-wind events, lower-magnitude and longer-duration winds can also be seen to result in isotherm displacement but not of the same magnitude. As in 2007, stronger winds tend to come from the northwest to north, and calmer winds are more often seen emanating from the southeast (Fig. 4.2b). The isotherm depths slowly increased until 17 September (Fig. 4.2d), similar to conditions in 2007.

Figure 4.3 shows the temperature profile as measured by the LDS for the same time periods in both 2007 and 2008, corresponding to Figures 4.1 and 4.2. The behavior of the thermal structure over the summer months in the time period shown in Figure 4.3 is quite similar between successive years. For both years, the initial surface mixed layer is approximately 3 m deep, while the metalimnion extends to a depth of approximately 8-9 m. The thermal structures on 30 September also show similarities. The base of the mixed layer deepened to approximately 6 m and the temperature in the epilimnion cooled to 19-20°C.

The differences lie in the discrepancy between the temperatures in the hypolimnion. The hypolimnion is 3-4°C warmer in 2008 as compared to 2007. Due to the comparatively warmer conditions in the hypolimnion, coupled with similar temperatures in the surfaced mixed-layer, there is consequently less stratification in 2008.

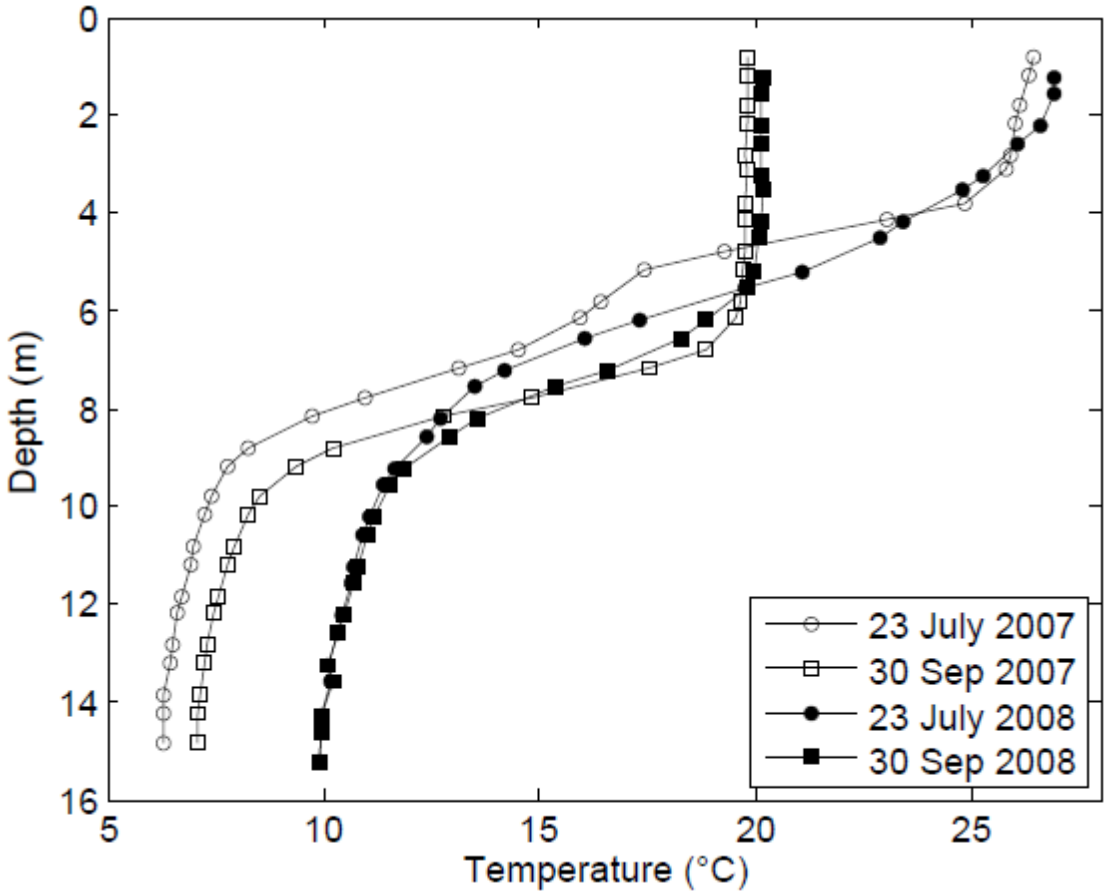

Figure 4.3. Changes in stratification in Ada Hayden Lake. Temperature profiles depicted as measured from the LDS thermistor chain in 2007 and 2008. Dates correspond to the beginning and ending of time series shown in Figures 4.1 and 4.2.

Therefore, equal forcing conditions in 2008 should theoretically yield greater isotherm movement. However, the stratification in Ada Hayden Lake was sufficiently strong to prevent complete vertical mixing throughout the water column (see Figs. 4.1d and 4.2d).

To classify the lake response to wind forcing based on stratification, the environmental conditions and basin characteristics of Ada Hayden Lake were represented

using a two-layer model (Fig. 4.4), after Horn et al. (2001). The timescales for various degeneration mechanisms (i.e., Kelvin-Helmholtz billows, supercritical bores, solitons) were calculated for varying stratification assuming a density change of 3.6 kg/m^3, a thermocline thickness of 5 m, and a turbulent boundary layer thickness of 1 m. These timescales are plotted in terms of the ratio of the amplitude of the basin-scale wave ζ_0 to the surface layer h_1 (equivalently, the inverse of the Wedderburn number W^{-1}) and the depth ratio of the surface layer to the total depth H.

Wind and temperature measurements from 2007 and 2008 were analyzed to determine the stratification (represented by the depth ratio) h_1 / H and the lake response W^{-1} due to wind forcing. The observed points were binned and given a percentage value pertaining to the relative frequency of the number of occurrences in the respective bin to the total number of occurrences (Fig. 4.4). Observed values indicate Ada Hayden Lake experiences sufficient stratification, due to the high values of the depth ratio ranging from 0.34 to 0.5. Additionally, the high values of W show resistance of the lake to internal movement caused by wind shear. The observed values lie exclusively within Regime 1, and will therefore be governed by linear wave theory. Thus, the field data indicates Ada Hayden Lake lends itself well to hydrostatic numerical models, as nonlinear steepening and non-hydrostatic pressures do not appear to be prevalent.

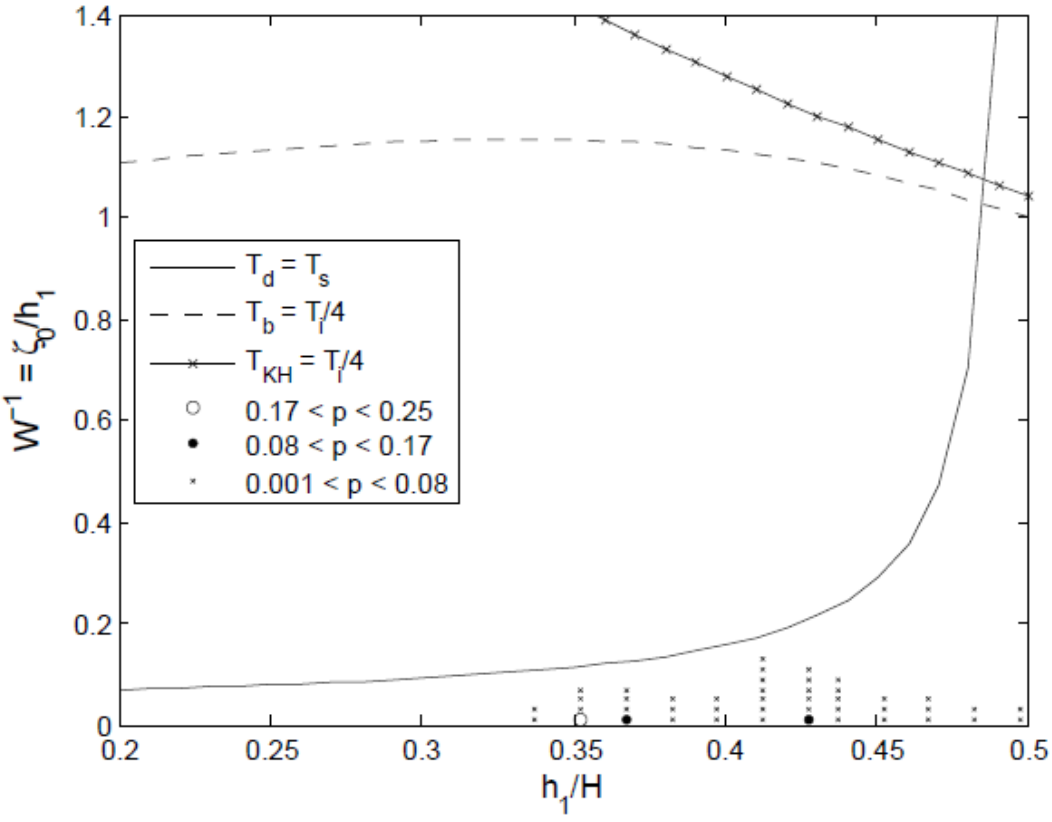

Figure 4.4 Internal wave degeneration regimes for Ada Hayden Lake plotted in terms of the amplitude ratio of the basin-scale wave $\zeta_0 / h_1 = W^{-1}$ and the depth ratio h_1 / H : damping (T_d), nonlinear steepening (T_s), supercritical flow (T_b), shear instabilities (T_{KH}), and the wave period (T_i). Observations were binned and are shown for percentage *p* of the respective bin relative to the number of observations. Linear wave theory applies to conditions given in Regime 1 ($T_d < T_s$).

West Okoboji Lake

Comparing results from Ada Hayden Lake to results from West Okoboji Lake allows the effect of differences in lake size, geometry, wind forcing, and stratification to be studied. Measurements from the LDS at West Okoboji Lake between 28 May and 23 July in 2009 are shown in Figure 4.5. Compared to field results from Ada Hayden Lake, shown in Figures 4.1 and 4.2, West Okoboji Lake tends to experience higher velocity winds, higher variability in stratification, and greater vertical isotherm displacement. Wind speeds at West Okoboji Lake often exceeded 5 m/s, with sustained gusts often exceeding 10 m/s. The wind direction was highly variable when compared to Ada Hayden Lake, but strong wind gusts tended to originate from the west to northwest, while calmer winds were most often seen from due north. Periods of small Lake numbers were quite frequent from late May through June, most notably 30-31 May, and 1, 7, 19, 21, 28, and 30 June. These periods showed significant vertical movement of the isotherms present in the water column. Particularly, high wind events in late May forced surface water to depths of over 20 m.

Figure 4.6 shows a histogram of L_N occurrences for Ada Hayden Lake and West Okoboji Lake. West Okoboji Lake experienced larger percentages of both small and large Lake numbers. The only Lake number range in which Ada Hayden Lake experienced a higher frequency of occurrence was L_N = 50-100. The implications from Figure 4.6 are this: Ada Hayden Lake was more consistent with observed lake response, with Lake numbers typically ranging from 10 to 500, while West Okoboji Lake was more

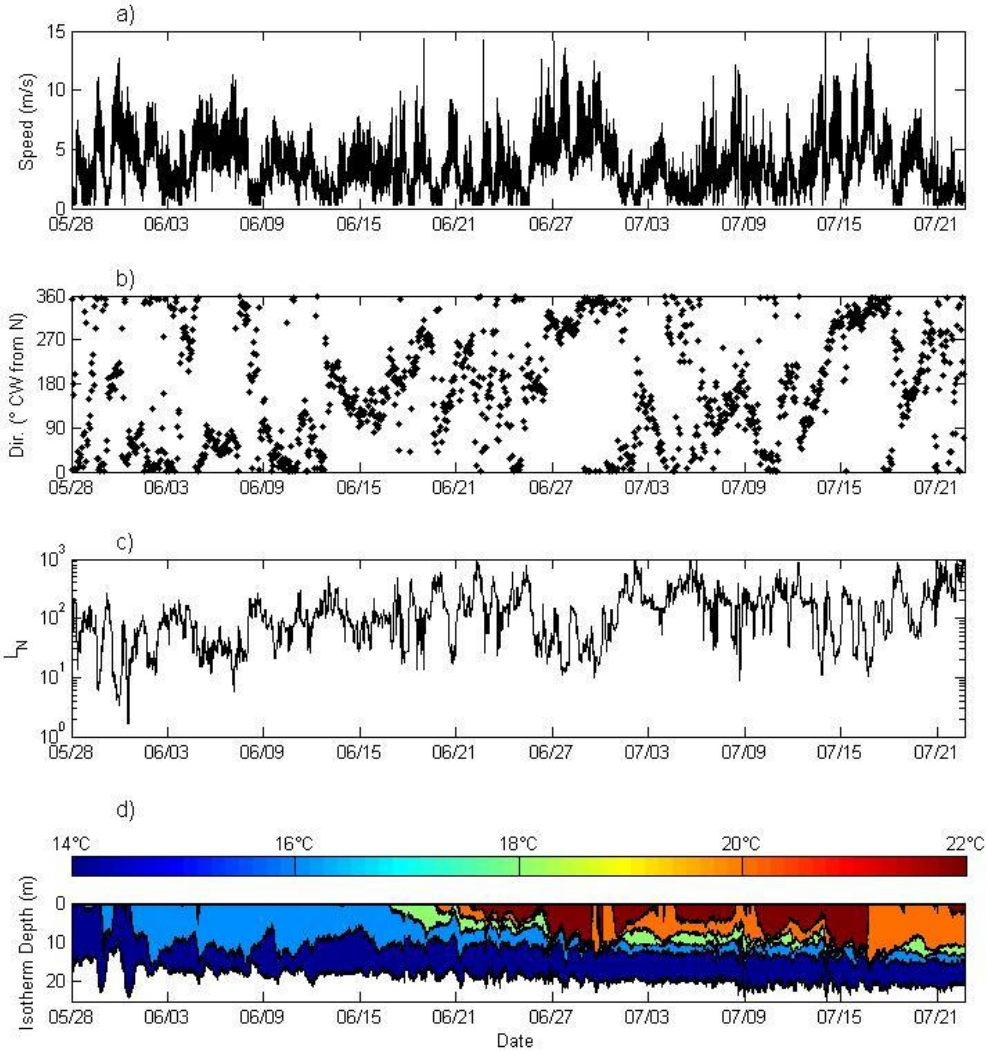

Figure 4.5. Field results from West Okoboji Lake in 2009, as measured by the LDS: (a) wind velocity (m/s) measured at 2.14 m above the water surface, (b) wind direction (°) measured clockwise from north (0°), (c) Lake number calculated using filtered wind speed and temperature data from the LDS, (d) contour plot showing isotherm depths for even isotherms between 14° and 22°C.

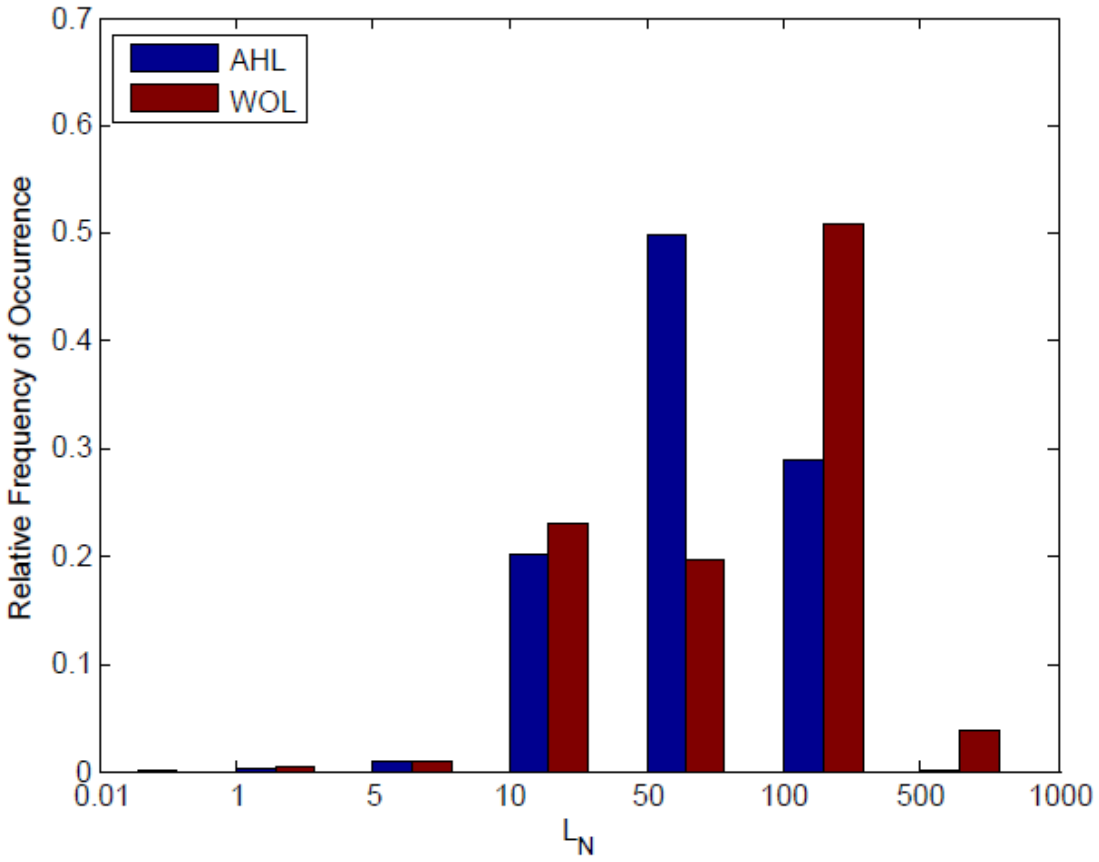

Figure 4.6. Histogram of L_N values for Ada Hayden Lake and West Okoboji Lake.

variable; it had higher occurrences in both Lake number values less than one and greater than 500.

Figure 4.7 shows the temperature profile as measured at the LDS for various time periods in 2009 corresponding to Figure 4.5. The behavior of the West Okoboji Lake's thermal structure was quite different than seen in Ada Hayden Lake. Initially, there was weak stratification with 2.5-3°C separating the temperatures at the surface from those at a depth of 25 m. The temperature profile at 29 May lacks the typical layered-structure seen

in Ada Hayden Lake (Fig.4.3) and could be considered linearly stratified. As the summer progressed, solar radiation heated the surface water, while wind-induced mixing eroded the stratification. The high velocity winds at West Okoboji prevented a surface mixed layer from fully forming until mid July. At this time, the base of the mixed-layer

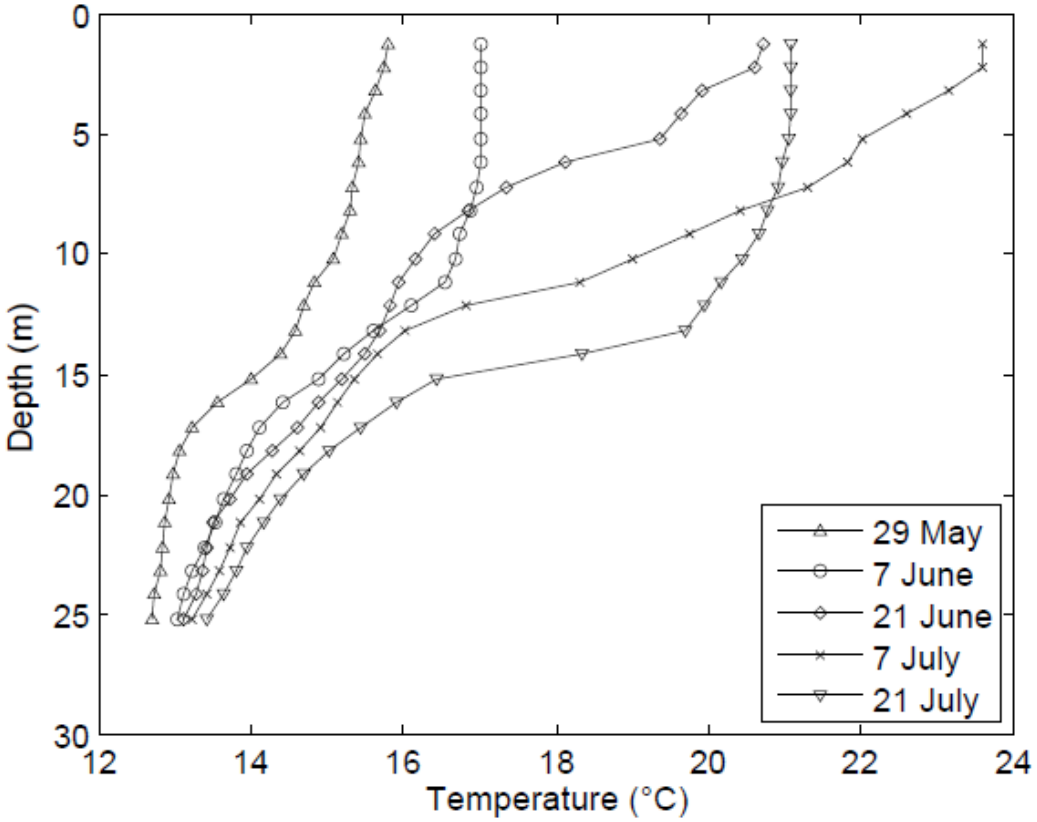

Figure 4.7. Changes in stratification in West Okoboji Lake. Temperature profiles depicted as measured from the LDS thermistor chain in 2009. Changes are shown for five periods over the course of two months.

extended to over 10 m, while the metalimnion extended to a depth between 16 and 19 m. Because of weak stratification, internal motions occurred throughout the water column, as shown in Figure 4.5d.

As previously discussed for Ada Hayden Lake, internal wave degeneration timescales were determined for West Okoboji Lake by representing the lake as a two-layer model to determine the lake response under different stratifications and wind events (Fig. 4.8). The density profiles for West Okoboji Lake were more linear than seen for Ada Hayden Lake, resulting in difficulties when using two-layer model for. However, these time periods of near linear stratification were few and most often observed early in the summer. Analysis was restricted to times where a two-layer structure could be approximated. Field observations were analyzed to determine the stratification and the lake response. The percentage and spread of the binned data is less condensed when compared to the results from Ada Hayden Lake. West Okoboji Lake experienced varying degrees of stratification, with depth ratios varying between 0.25 and 0.45. Additionally, it appears the lake experienced nonlinear wave activity, as evidenced by the greater number of occurrences in Regime 2.

While these nonlinear waves cannot be physically represented through hydrostatic modeling, Hodges et al. (2006) proved that under forcing conditions appropriate for the formation of nonlinear waves, numerical hydrostatic models can accurately reproduce basin behavior for times less than the time required for the onset of steepening τ_s, defined as

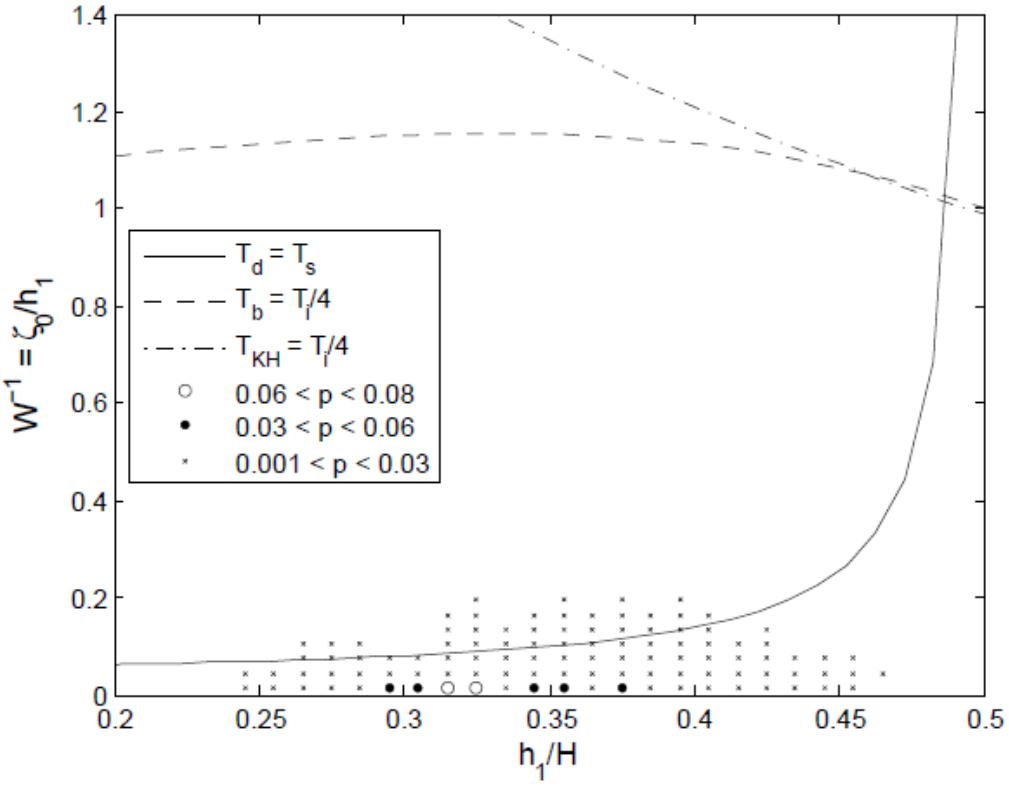

Figure 4.8 Internal wave degeneration regimes for West Okoboji Lake plotted in terms of the amplitude ratio of the basin-scale wave $\zeta_0 / h_1 = W^{-1}$ and the depth ratio h_1 / H: damping (T_d), nonlinear steepening (T_s), supercritical flow (T_b), shear instabilities (T_{KH}), and the wave period (T_i). Observations were binned and are shown for percentage *p* of the respective bin relative to the number of observations. Linear wave theory applies to conditions given in Regime 1 ($T_d < T_s$).

$$\tau_s = \frac{1}{6\zeta_0}\frac{h_1 h_2}{|h_1 - h_2|}T \tag{4.1}$$

where ζ_0 is the initial wave amplitude, T is the period of the gravest mode, and h_1 and h_2 are the depths of the upper and lower layers, respectively. The gravest mode is the lowest mode, here taken to be the first baroclinic mode, or the V1H1 seiche.

Additionally,nonlinear waves can be dissipated in the time it would take for steepening to occur (Hodges et al., 2006). It is therefore initially assumed that using measured field conditions from both Ada Hayden and West Okoboji Lakes, a hydrostatic model should be able to replicate and resolve the internal motions registered by the thermistor chains. Model results will then be checked to validate the use of a hydrostatic model. The three time periods chosen for modeling are described in detail in the next section.

Simulation Events and Results

Three separate events were chosen for numerical simulation using the Estuary, Lake, and Coastal Ocean Model (ELCOM). The events provide ELCOM with varying forcing conditions and stratification for two different lakes, grouped together using the Lake number. Conditions within the time periods consist of i) large L_N, ii) moderate L_N, iii) and small L_N (Table 4.1).

Table 4.1. Summary of simulation events. h_1/H is a measure of the relative top layer thickness when representing the stratification using a two-layer model. Stratification and forcing conditions for simulations 1-3 are combined using L_N (range of values and averages are given). AHL = Ada Hayden Lake, WOL = West Okoboji Lake.

Simulation	Time Period	Lake	h_1/H	L_N Range (Avg)
1	7-12 Aug. 2007	AHL	0.35	3-553 (115)
2	30 July-4 Aug. 2008	AHL	0.35	6-495 (89)
3	6-18 July 2009	WOL	0.32	0.01-275 (31)

Simulation 1: High Lake Number

The first event to be simulated consists of 7-12 August 2007 at Ada Hayden Lake. This period experienced relatively calm wind and was sufficiently stratified to limit internal motions. The initial stratification and mode shape is shown in Figure 4.9. Figure 4.9 shows the thermocline depth to be approximately 6 m when representing the lake as a two-layer system. When considering a three-layer temperature structure, a metalimnion of finite thickness exists, with the top and bottom at depths of approximately 4 and 9 m, respectively. The normal mode equation (2.11) given by Münnich et al. (1992) yields a phase speed c_n for a V1H1 internal wave of approximately 0.3 m/s and a wave period of 1.3 hours. Once the phase speed is known, the horizontal grid size and time step can be related using the expression for the CFL condition (3.1). A total of 56 simulations was run for this event, with different grid sizes in the horizontal (Δx), vertical (Δz), and model time steps (Δt) which correspond with Δx (Table 4.2).

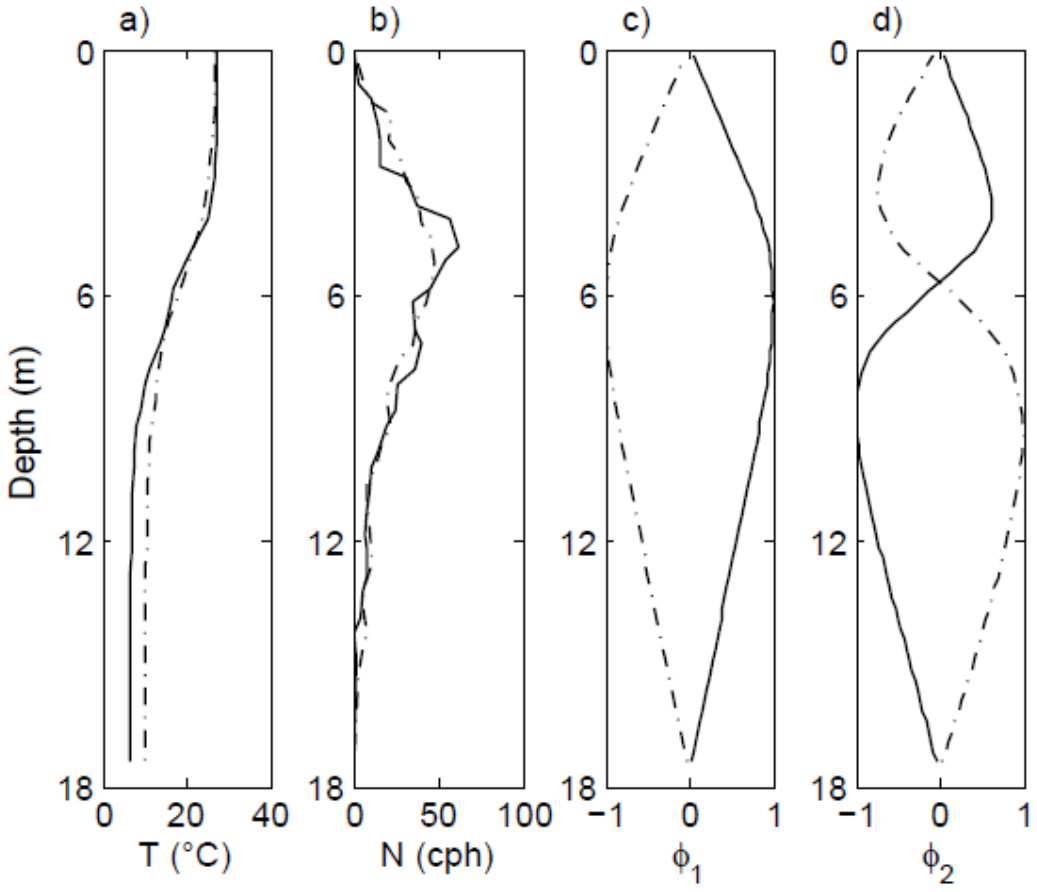

Figure 4.9. Profiles for Ada Hayden Lake using measurements at the LDS thermistor chain from 7 Aug 2007 (–) and 30 July 2008 (· – ·). (a) Temperature profile used for computing the vertical modes, (b) buoyancy frequency based on (a). (c) and (d) show the mode shape for the first and second vertical mode, respectively.

Table 4.2. ELCOM resolutions for Simulation 1 model runs. Here Δx gives the horizontal grid size such that $\Delta x = \Delta y$, Δz is the vertical grid size, and Δt is the model time step.

Δx (m)	Δz (cm)	Δt (s)	Δx (m)	Δz (cm)	Δt (s)	Δx (m)	Δz (cm)	Δt (s)
10	50	10	35	20	40	55	40	60
"	60	"	"	50	"	"	50	65
15	10	15	"	60	"	60	10	65
"	10	"	40	30	45	"	30	"
"	30	"	"	50	"	"	40	"
"	40	"	"	60	"	"	50	"
"	60	"	"	70	"	"	60	"
20	50	20	"	90	"	"	70	"
"	60	"	45	10	50	"	90	"
"	70	"	"	20	"	65	20	70
"	80	"	"	40	"	"	30	"
25	20	25	"	50	"	"	40	"
"	25	"	"	60	"	70	20	80
"	40	30	50	30	55	"	30	75
"	50	30	"	40	"	"	40	"
"	60	25	"	50	"	"	50	"
30	10	30	"	60	"	75	30	85
"	30	"	55	20	60			
"	60	"	"	30	"			

Model results are compared to field observations for the locations of both the LDS and T-Chain 52. Figures 4.10 and 4.11 show the model results for a 15 m horizontal grid size and 0.1 m vertical grid size. Model results at the LDS (Fig. 4.10) show ELCOM reproduced most of the observed vertical motions, most notably the early morning of 7 and 8 August, and the afternoon/evening activity on 9 and 11 August. The presence of

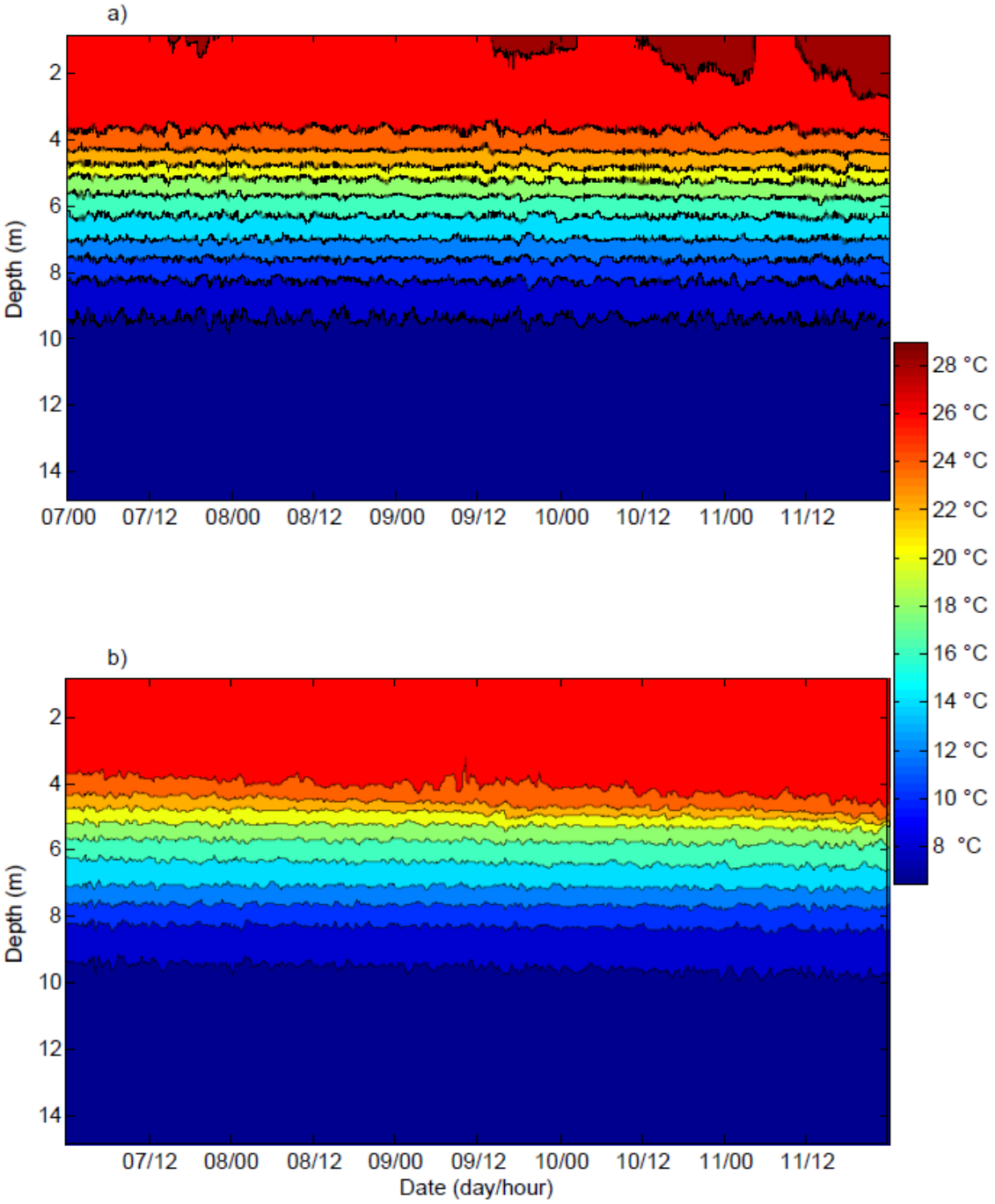

Figure 4.10. Time series temperature profile plot for Simulation 1, measured by the LDS for a) field data and b) ELCOM output at 15 m horizontal grid cell size and 0.1 m vertical grid cell size.

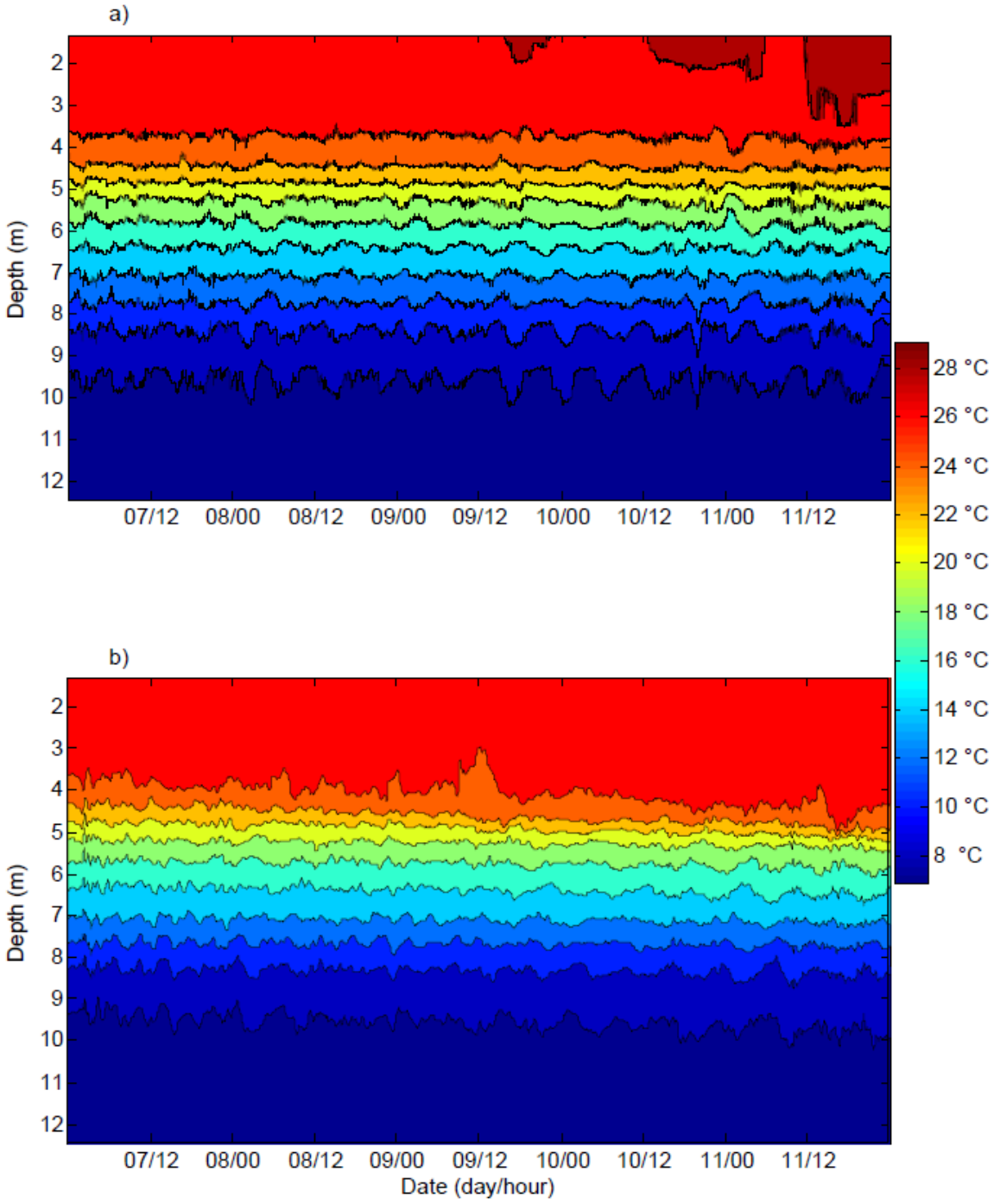

Figure 4.11. Time series temperature profile plot for Simulation 1, measured by T-Chain 52 for a) field data and b) ELCOM output at 15 m horizontal grid cell size and 0.1 m vertical grid cell size.

the 28 °C isotherm is not reproduced in ELCOM, most likely because of computational errors in the non-penetrative long-wave radiation that heats the surface-mixed layer (Hodges et al., 2000). Long-wave radiation, which is emitted from clouds and atmospheric water vapor, is estimated in ELCOM using cloud cover, air temperature, and humidity. Because cloud cover was not measured, ELCOM estimated long-wave radiation for zero cloud cover. While this would underpredict some heating in the surface mixed layer, the depth of the base of the mixed layer appeared to slightly deepen throughout the simulation. The comparison between field observations and model output at the location of T-Chain 52 (Fig. 4.11) shows similar results in the reproduction of internal motions. Vertical motions tended to be more pronounced at T-Chain 52. Most of the motion is located between the 4-9 m depth previously identified within the metalimnion, as would be expected by inspecting the buoyancy profile.

The same event was modeled at a coarser vertical resolution with a 0.6 m vertical grid cell size; but with the same 15 m uniform horizontal grid and the same 15 s model time step. Results from the LDS (Fig. 4.12) and T-Chain 52 (Fig. 4.13) show lower frequency vertical motion and a thickening of the metalimnion by the spreading of the temperature contours. At the end of the simulations, the metalimnion thickness was 4.7 and 5.4 m for Δz = 0.1 and 0.6 m, respectively. ELCOM's ability to resolve higher frequency motions is limited by the cell size (Hodges et al., 2000). This metalimnion thickening is characteristic of numerical diffusion, which leads to the erosion of the thermocline and isopycnal spreading. Figure 4.13b shows the 26°C isotherm surfacing midday on 9 August from the model output, but no such movement is seen in the field data. This isotherm surfacing could be caused by error in the surface thermodynamic

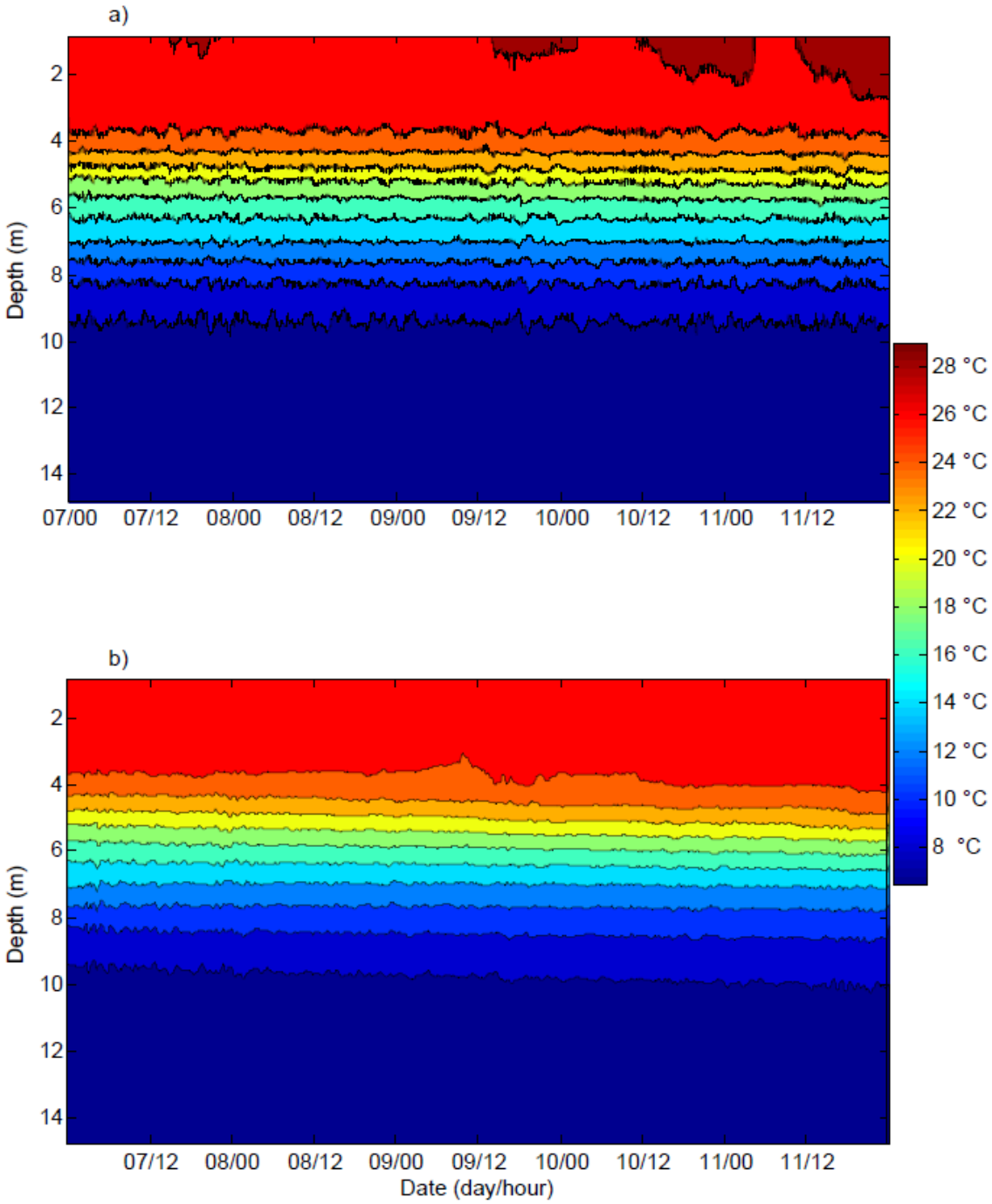

Figure 4.12. Time series temperature profile plot for Simulation 1, measured by the LDS for a) field data and b) ELCOM output at 15 m horizontal grid cell size and 0.6 m vertical grid cell size.

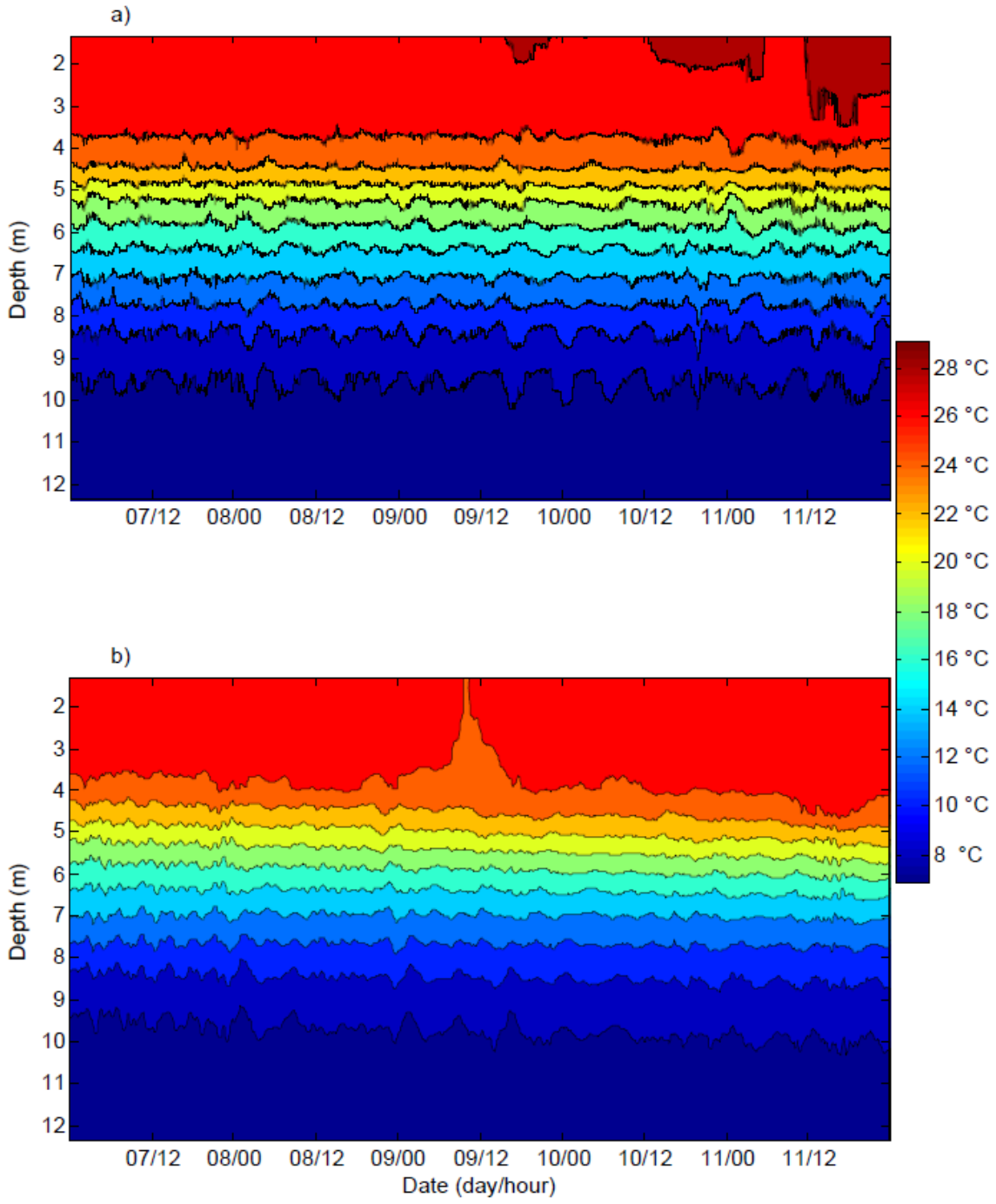

Figure 4.13. Time series temperature profile plot for Simulation 1, measured by T-Chain 52 for a) field data and b) ELCOM output at 15 m horizontal grid cell size and 0.6 m vertical grid cell size.

model. Similar results, in terms ELCOM predicting the surfacing of isotherms not observed in the field, can be seen in the literature (e.g., Fig. 12 in Hodges et al., 2000 and Fig. 11 in Yeates et al., 2008), although no discussion concerning the discrepancy was provided.

Hodges et al. (2006) gave empirical relationships for numerical diffusivity (2.61) and numerical viscosity (2.63). These relationships show both numerical error terms scaled inversely to the gradient Richardson number $Ri_g^{-1/3}$. After Yeates et al. (2008), the Lake number L_N can be substituted for Ri_g by using the relationship $Ri_g \sim L_N^2$ given by Imberger (2004). Therefore, $L_N^{-2/3}$ can be used to estimate numerical diffusion and numerical viscosity during a model run.

Figure 4.14a shows values for $L_N^{-2/3}$ computed from measured wind speed. As numerical diffusion and viscosity have been shown to scale with $L_N^{-2/3}$, magnitudes of E_P and E_K are not of as much interest as the behavior between field and model results. ΔE_P is used as the total potential energy in the water column is much larger than comparatively small changes caused by internal waves and diurnal heating. A normalized time series of ΔE_P is shown in Figure 4.14b. To assess the total amount of vertical fluid movement throughout a simulation period, $\sum E_K$ is used (Fig. 4.14c). A strong wind event can be seen shortly after the start of the simulation on 7 August. This increase in $L_N^{-2/3}$ appears to not negatively affect the model's performance initially in terms of potential energy. However, the model slightly overpredicted the internal

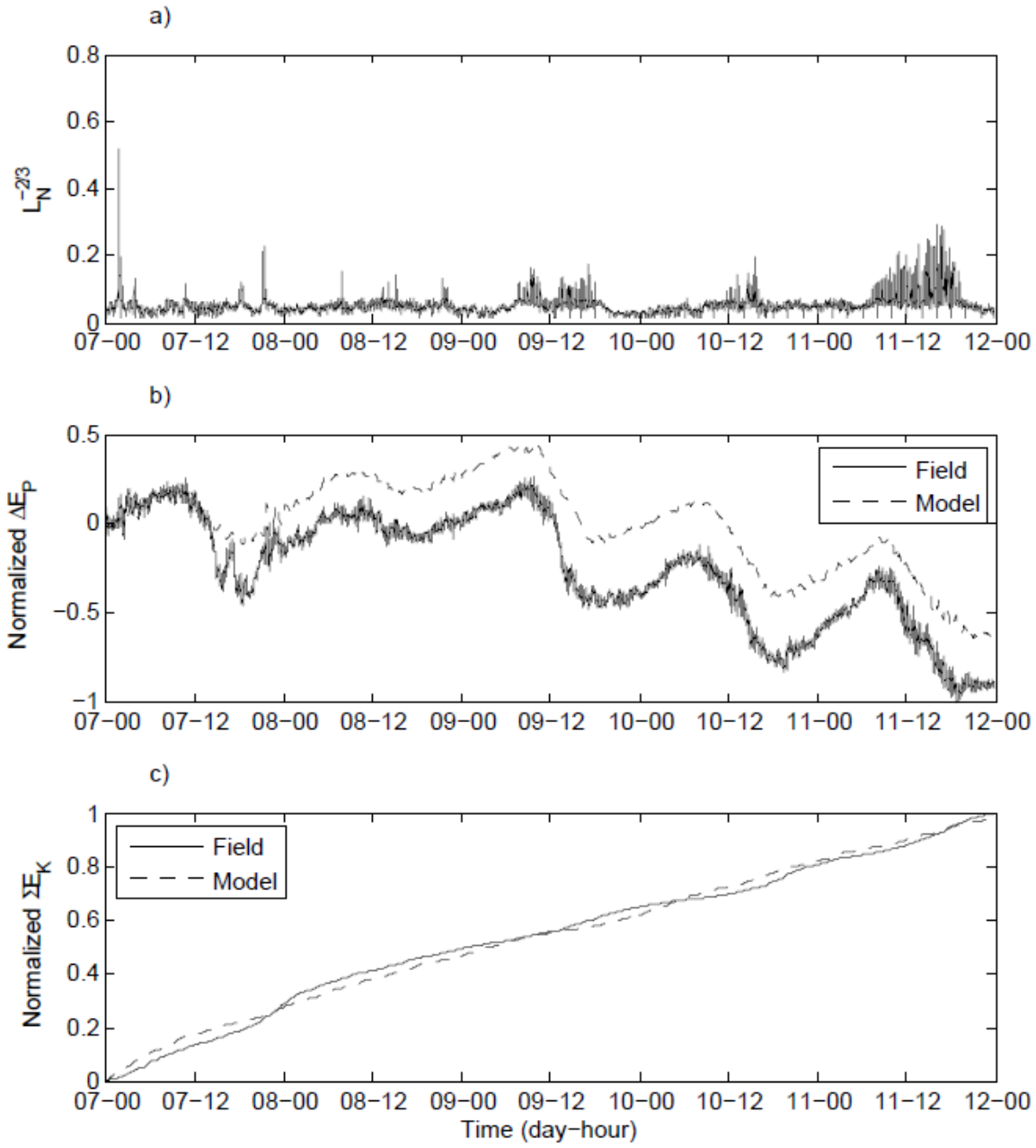

Figure 4.14. The effect of L_N on numerical diffusion and viscosity during Simulation 1 measured by the LDS. a) Time series of $L_N^{-2/3}$, b) change in potential energy, and c) cumulative sum of kinetic energy. Model results shown used Δx = 10 m and Δz = 0.5 m.

motions as the model yielded higher kinetic energy values (Fig. 4.14c). A second wind even in the evening of 7 August caused a slight increase in $\sum E_K$ and fluctuations in E_P in the field data. The model failed to register the increase in E_K, evidenced by the field kinetic energy sum overtaking the model results (Fig. 4.14c).

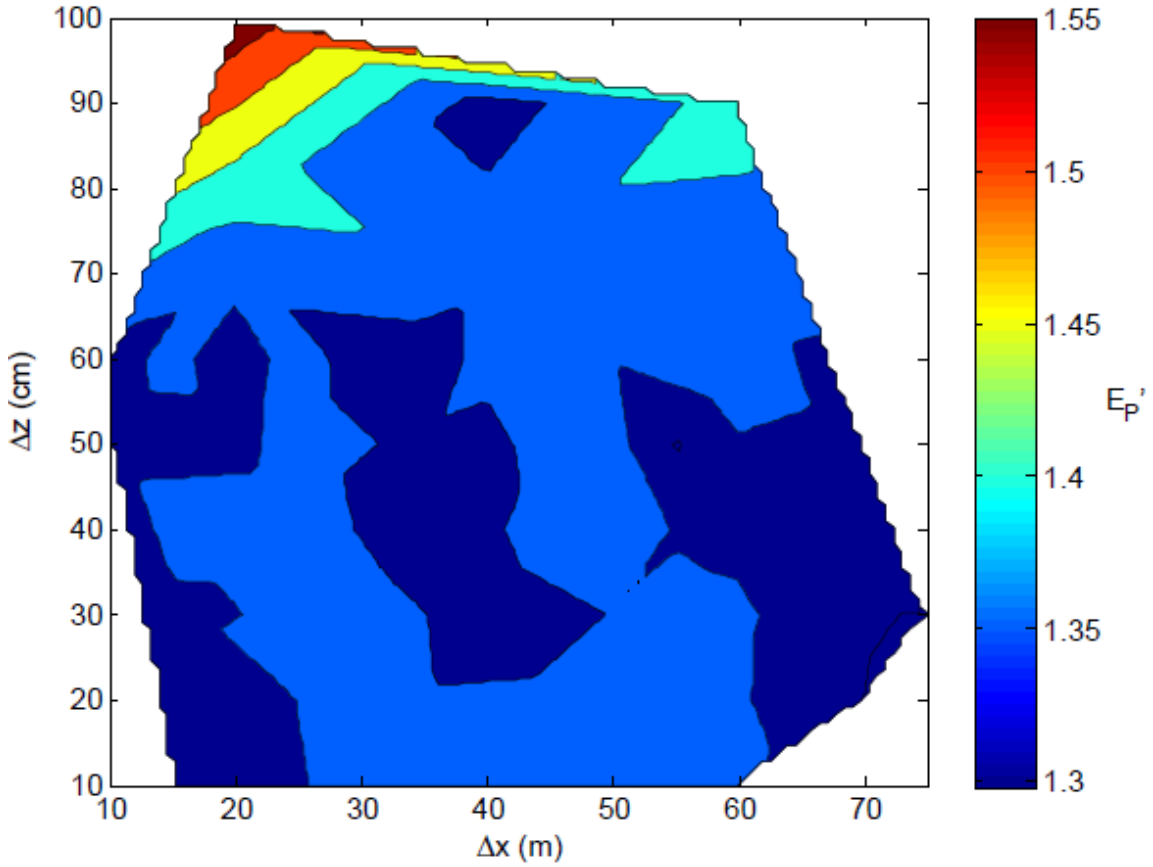

Figure 4.15. Normalized time-integrated potential energy from Simulation 1, measured by the LDS. Horizontal and vertical grid cell size is given by Δx and Δz, respectively.

Additionally, ELCOM began to show elevated potential energy values for the remainder of the simulation. ELCOM appears to accurately predict the trends in potential energy fluctuations (Fig. 4.14b) and almost match kinetic energy values exactly (Fig. 4.14c). However, ELCOM did show error in reproducing the thermal structure of the

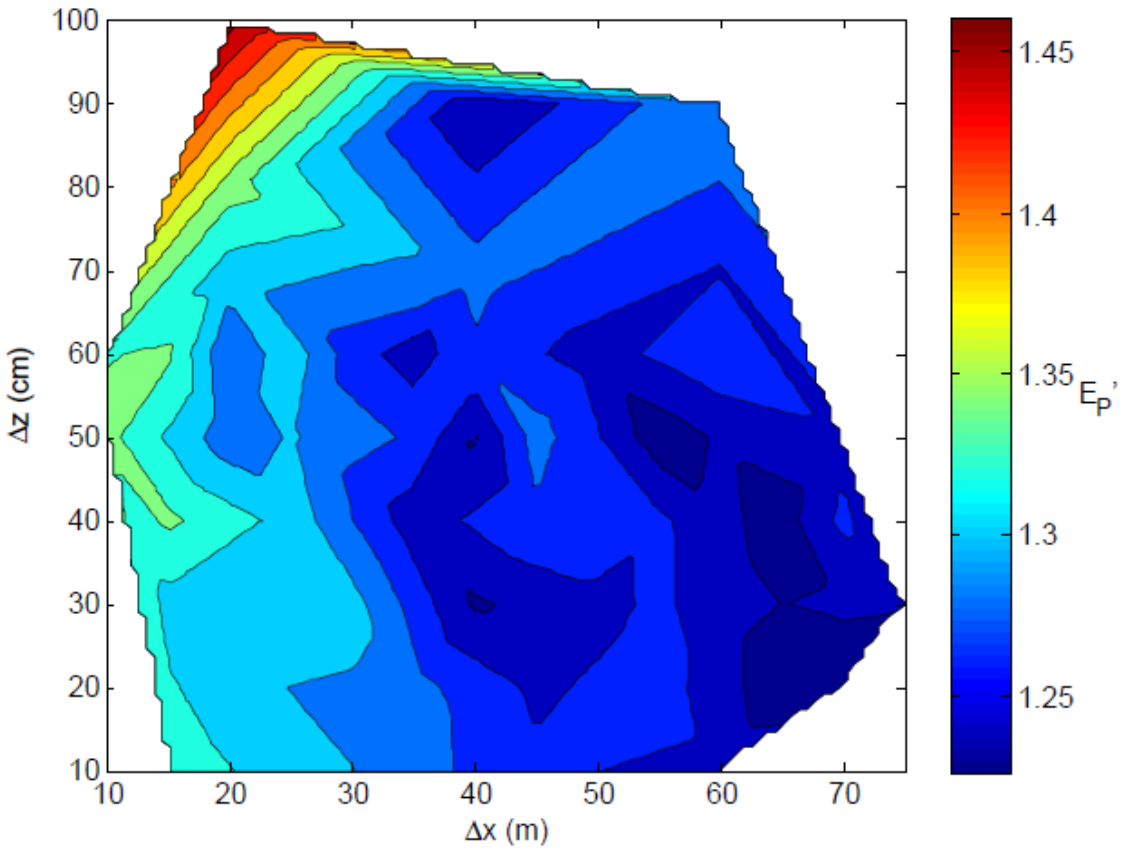

Figure 4.16. Normalized time-integrated potential energy from Simulation 1, measured by T-Chain 52. Horizontal and vertical grid cell size is given by Δx and Δz, respectively.

lake, indicated by the elevated potential energy values. High potential energy values in the model output could be caused by elevated mixing or numerical diffusion.

The normalized potential energy E_P' (3.20) results are shown for the values measured by the LDS (Fig. 4.15) and T-Chain 52 (Fig. 4.16). $E_P' > 1$ indicates the model producing a higher center of mass within the water column, while lower values indicate a lower center of mass. A higher center of mass could be the result of either elevated mixing in the model or numerical diffusion. Figure 4.15 shows E_P' values greater than one throughout all simulations, ranging from approximately 1.3 to 1.55. The best model results for the location of the LDS occur for lower horizontal grid sizes (between 10 and 40 m), and vertical grid cell sizes varying between 0.3 and 0.6 m. Interestingly, there appears to be a realm between Δx = 20-30 m and Δz = 0.2-0.4 m where there is an increase in normalized potential energy. High E_P' values occur for high vertical grid sizes of 0.8 m or higher. The results from T-Chain 52 (Fig. 4.16) are quite similar compared to the LDS. In general, the lower the vertical grid size, the better the model performance. However, lower values for the horizontal grid resulted in an increase in potential energy. Therefore, best model results in terms of maintaining the thermal structure appear to be Δx = 40 m and Δz = 0.3 m based on the results in Figs. 4.15 and 4.16.

The normalized time-integrated kinetic energy results E_K' (3.22) are shown in Figures 4.17 and 4.18 for profiles at the LDS and T-Chain 52, respectively. Model results at the LDS location show best agreement with field observations for small

horizontal and grid cell sizes, but are relatively insensitive to changes in the vertical grid. Particularly, the best results are found from models with a horizontal cell size of 15 - 20 m and vertical cell size of 0.2 - 0.6 m. This region recovered over 50% of the total depth-integrated kinetic energy. Increasing the horizontal grid cell size resulted in a decrease of total

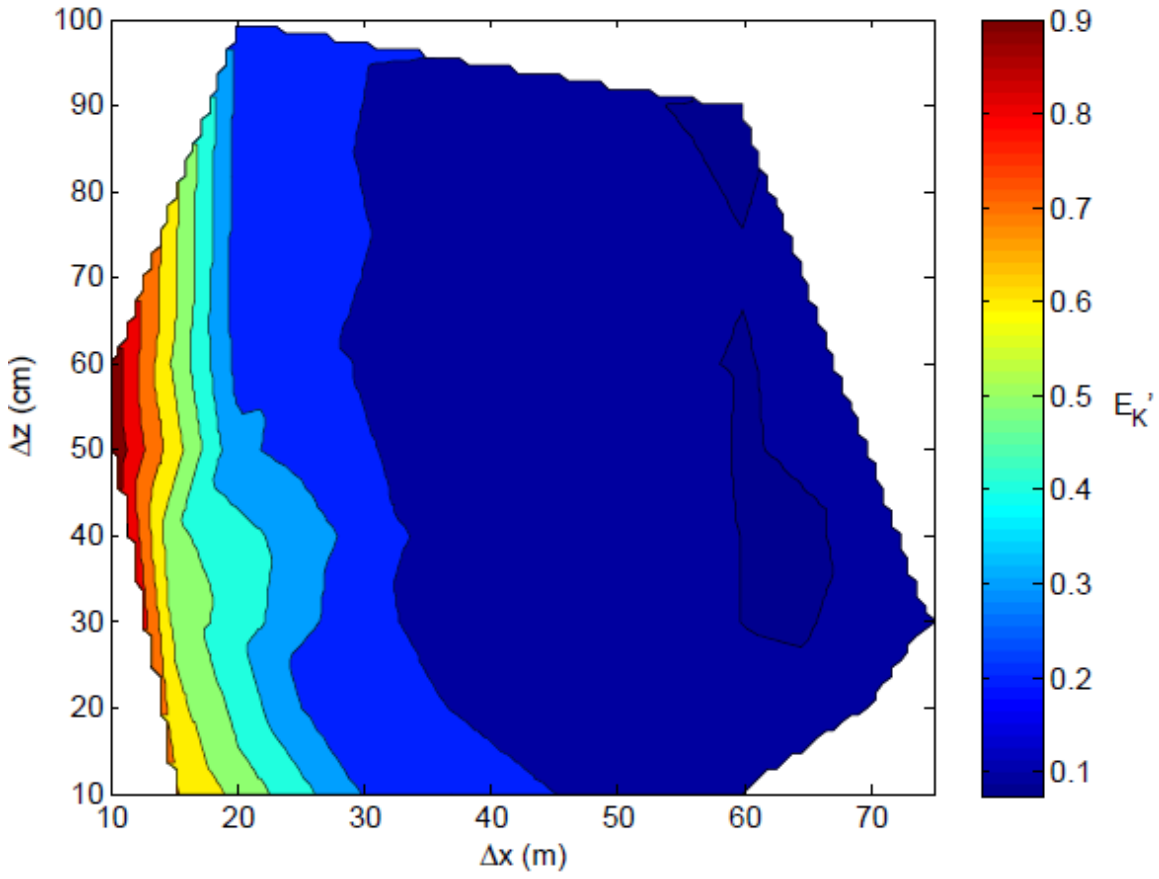

Figure 4.17. Normalized time-integrated kinetic energy from Simulation 1, measured by the LDS. Horizontal and vertical grid cell size is given by Δx and Δz, respectively.

kinetic energy reproduced in the model, with Δx values greater than 40 m yielding values less than 10% measured in the field. Figure 4.18 gives similar results for model performance as measured at the location of T-Chain 52; low horizontal grid sizes appear to reproduce similar amplitude internal motions. However, unlike conditions at the LDS, Fig 4.18 shows a concentrated area of higher kinetic energy values for Δx = 60 - 70 m and Δz = 0.1 - 0.3 m.

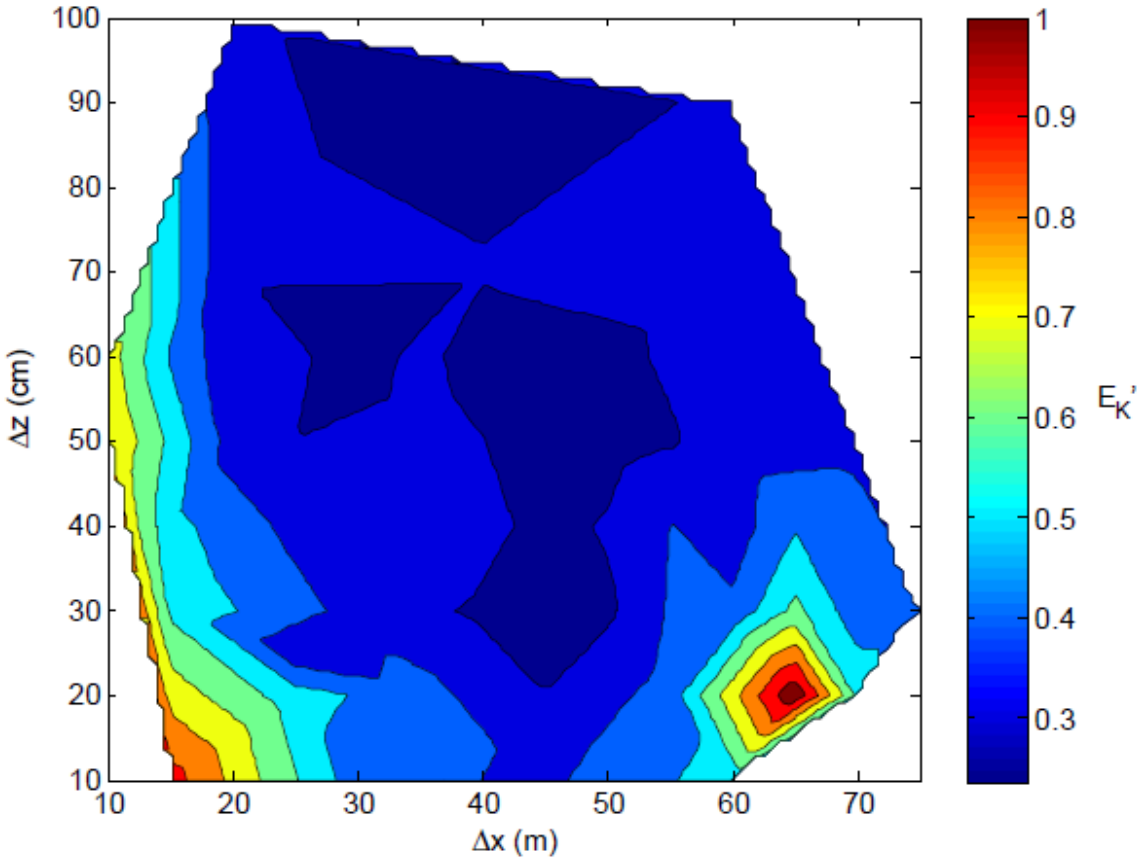

Figure 4.18. Normalized time-integrated kinetic energy from Simulation 1, measured by T-Chain 52. Horizontal and vertical grid cell size is given by Δx and Δz, respectively.

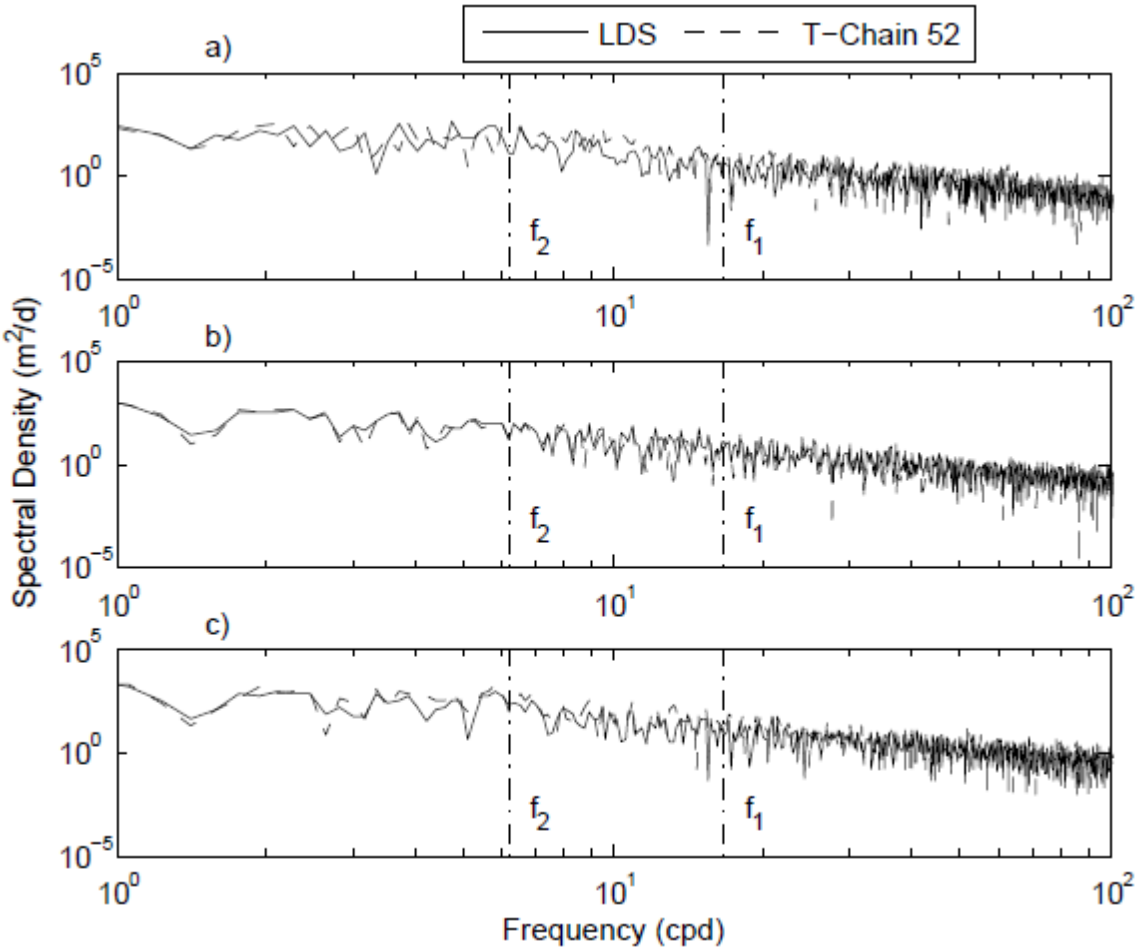

Figure 4.19. Displacement power spectra calculated from field data at Ada Hayden Lake during Simulation 1 for a) 25°C, b) 17°C, and c) 12°C isotherms. Power spectra shown for isotherm displacements measured from the LDS and T-Chain 52. The frequencies for the V1 and V2 mode internal wave are shown as f_1 and f_2, respectively.

To determine if there is a dominant internal wave frequency, a displacement power spectra was calculated for the 25, 17, and 12°C isotherms (Fig. 4.19). The isotherms chosen were to represent the top, middle, and bottom of the metalimnion (see

Fig. 4.9 for the temperature structure of the lake). The results from the spectral analysis show no dominant frequencies at either the V1 or V2 mode seiche, simply a steady decline in spectral density with increasing frequency. To compare model results to field

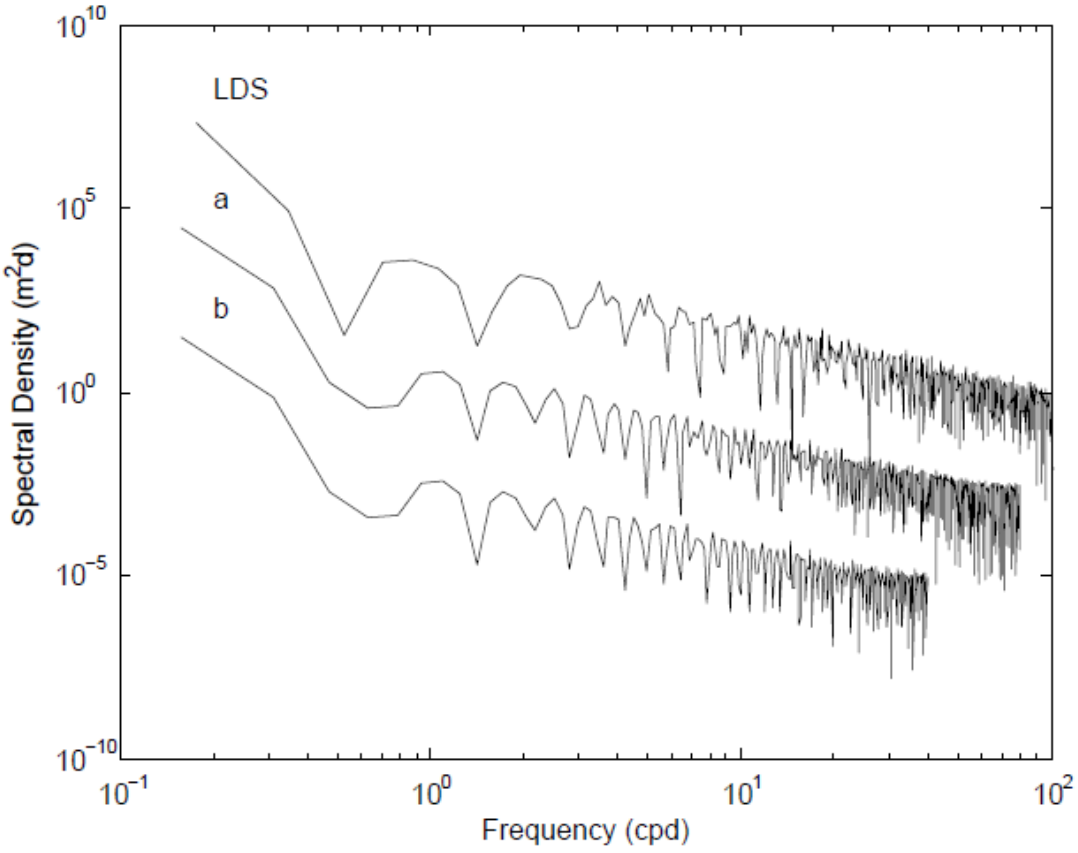

Figure 4.20. Spectral density of the displacement of the 17°C isotherm during Simulation 1. Isotherm displacement measured by the LDS and calculated using model output with a) Δx = 15 m, Δz = 0.3 m, and b) Δx = 30 m, Δz = 0.3 m. The vertical offset for each spectra is 10^3, beginning with a).

results, spectral density of the displacement of the 17°C isotherm from both field and model results are shown in Figure 4.20. Spectral density based on model results match well with the field results, except for higher frequencies. Because the CFL was held fixed at 1/3 throughout all simulations, increases in the horizontal grid size saw a similar increase in model time step.

Figure 4.21 shows the comparison of the 17°C isotherm between field observations and model results. The observed and modeled isotherm depths are plotted together, where a perfect model prediction would result with all points along the 1:1 line. However, a large amount of the points lie above the 1:1 line, indicating ELCOM overpredicting the isotherm depths. A WS value of 0.38 is shown for this particular simulation. WS values for all model runs are shown in Figure 4.22 as a function of grid size. Skill assessment results from the LDS (Fig. 4.22a) show, in general, higher WS values. The best results with WS values exceeding 0.55 were found for Δx = 40-60 m and Δz =0.1-0.2 m. Results at T-Chain 52 (Fig 4.22b) show lower model agreement, with largest WS value of approximately 0.4-0.43 found at grid sizes of Δx = 10-20 m and Δz = 0.5-0.65 m.

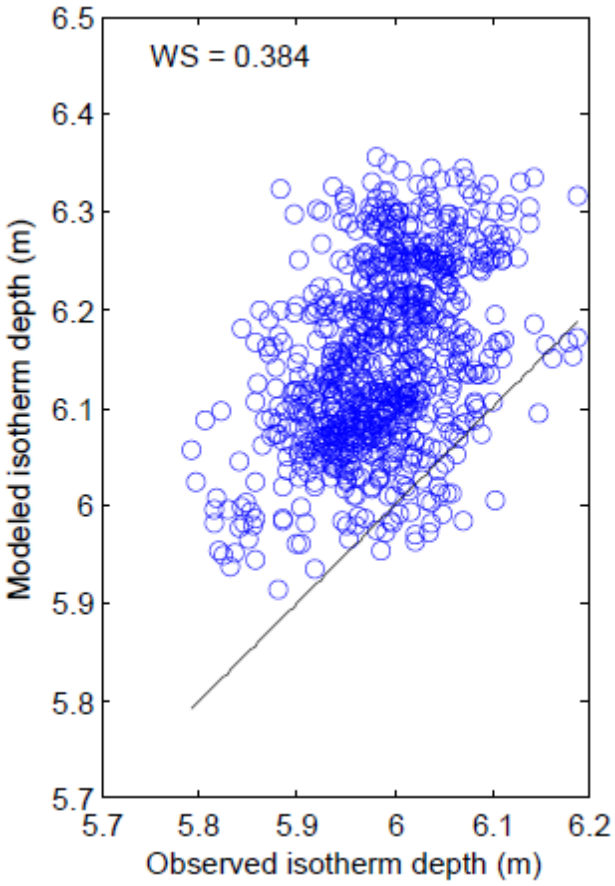

Figure 4.21. Observed and modeled 17°C isotherm depth for Simulation 1 (blue circles) with Δx = 15 m and Δz = 0.6 m. The Willmott skill number and 1:1 line is shown in black.

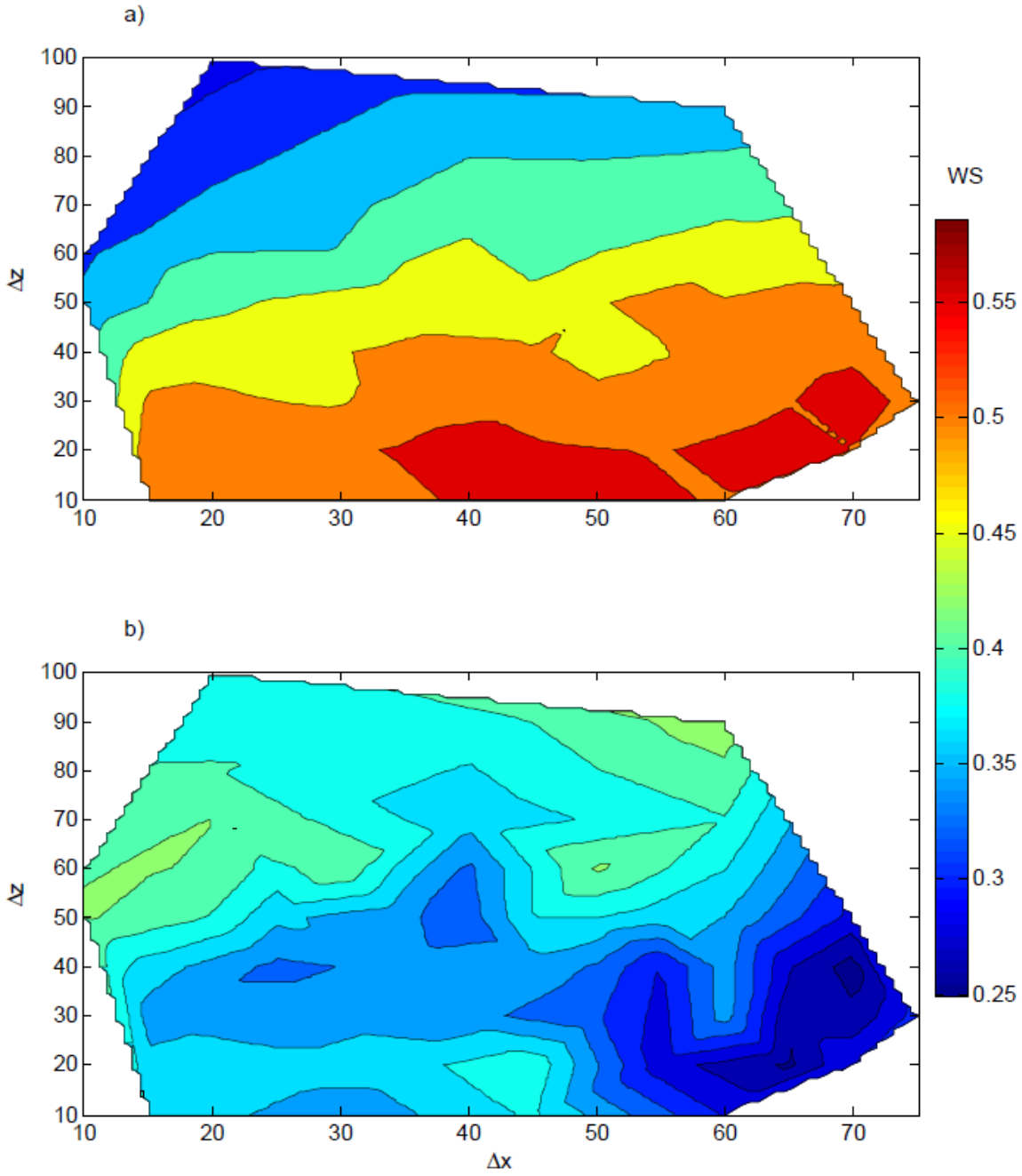

Figure 4.22. *WS* from Simulation 1, values shown for grid sizes in the horizontal (Δx) and vertical (Δz) from a) LDS and b) T-Chain 52.

Simulation 2: Moderate Lake number

The second simulated event occurs between 30 July and 4 August 2008 at Ada Hayden Lake. The five day period comprising the second simulation is identical to the duration of the first event. Likewise, the initial thermal structure is similar to conditions of the first event (see Fig. 4.9); epilimnetic water is of similar temperature, but the hypolimnion was warmer in 2008. The modal amplitudes in Figure 4.9c-d show similar trends: a surface-mixed layer and a weakly stratified hypolimnion, with a strongly stratified metalimnion of finite thickness. The phase speed c_n was estimated using (2.11) as 0.3 m/s with a wave period of 1.5 hours. A total of 58 simulations was run for this event, with different resolutions in the horizontal (Δx) and vertical (Δz), using different model timesteps (Δt). The model resolutions are shown in Table 4.3.

Model results are compared to field observations by comparing the vertical temperature structure at the locations of the LDS, T-Chain 52, and T-Chain 53 (see Fig. 3.1 for instrument locations). Figures 4.23-25 show model temperature output for Δx = 10 m, Δz = 0.1 m, and Δt = 10 s. Results at the LDS (Fig. 4.23) reproduce the isotherm movement seen on 31 July fairly well, but the model produces a steady deepening of the metalimnion throughout the simulation. Hodges et al. (2000) attributed the metalimnion deepening to errors in the mixing model: ELCOM neglects entrainment time, which allows the model to predict a deeper wind mixed layer. As seen in Simulation 1, ELCOM did not accurately predict the water temperature near the surface. Field observations show a warming and cooling cycle which is absent in the model. The

Table 4.3. ELCOM resolutions for model runs of Simulation 2. Here Δx gives the horizontal grid size such that $\Delta x = \Delta y$, Δz is the vertical grid size, and Δt is the model time step.

Δx (m)	Δz (cm)	Δt (s)	Δx (m)	Δz (cm)	Δt (s)	Δx (m)	Δz (cm)	Δt (s)
10	10	10	25	85	30	55	15	65
"	50	"	"	95	"	"	25	"
"	75	"	35	15	40	"	35	"
"	100	"	"	25	"	"	45	"
15	15	15	"	35	"	"	55	"
"	25	20	"	45	"	"	65	"
"	35	"	"	55	"	"	75	"
"	45	"	"	65	"	"	85	"
"	55	"	"	75	"	"	95	"
"	65	"	"	85	"	65	15	80
"	75	"	"	95	"	"	25	"
"	85	"	45	15	55	"	35	"
"	95	"	"	25	"	"	45	"
25	15	30	"	35	"	"	55	"
"	25	"	"	45	"	"	65	"
"	35	"	"	55	"	"	75	"
"	45	"	"	65	"	"	85	"
"	55	"	"	75	"	"	95	"
"	65	"	"	85	"			
"	75	"	"	95	"			

amplitude of the internal wave was underestimated by ELCOM, which can be attributed to numerical dissipation. The large amplitude motion on 31 July predicted by ELCOM was approximately 78% of the results measured in the field. Hodges et al. (2000) cited numerical damping of the Kelvin wave during simulations of Lake Kinneret, while Gomez-Giraldo et al. (2006) observed an approximate 20% reduction in internal wave amplitude caused by numerical dissipation due to the no-normal-flow boundary condition

applied to a coarse grid model. Therefore, the observed damping is similar to values given in the literature.

The model results at the thermistor chain locations are similar to those depicted at the LDS. Figure 4.24 shows the comparison between field observations and model output at the location of T-Chain 52. As was seen at the LDS, the internal wave oscillations on 31 July are reproduced by ELCOM, but the overall magnitude is underestimated. Field data shows the 22 and 24°C isotherms rising by approximately 1 m, that motion is damped in the model. Figure 4.25 shows that T-Chain 53 experienced more internal wave activity, both in the duration of activity on 31 July and on 3 August. The surface temperature fluxes are not correctly reproduced: field observations show surface heating from 31 July - 3 August that was not present in the model. ELCOM predicted upward movement of the 24°C isotherm beginning 2 August at both thermistor chain locations. This surfacing was not observed in the field, perhaps indicating errors in the mixing model, the wind momentum model, or in the numerical scheme.

Figure 4.26a shows values for $L_N^{-2/3}$ computed from measured wind speed. As numerical diffusion and viscosity have been shown to scale with $L_N^{-2/3}$, magnitudes of E_P and E_K are not of as much interest as the behavior between field and model results. As previously discussed, ΔE_P is used as the changes due to internal wave perturbations are small, and is shown in Figure 4.26b. Similarly, E_K values tend to be small as velocities in the column tend to be slow. To gain a feeling of the total amount of vertical fluid movement throughout a time period, $\sum E_K$ is shown in Figure 4.26c. A low L_N event occurred on 31 July, and while field observations show a marked increase in

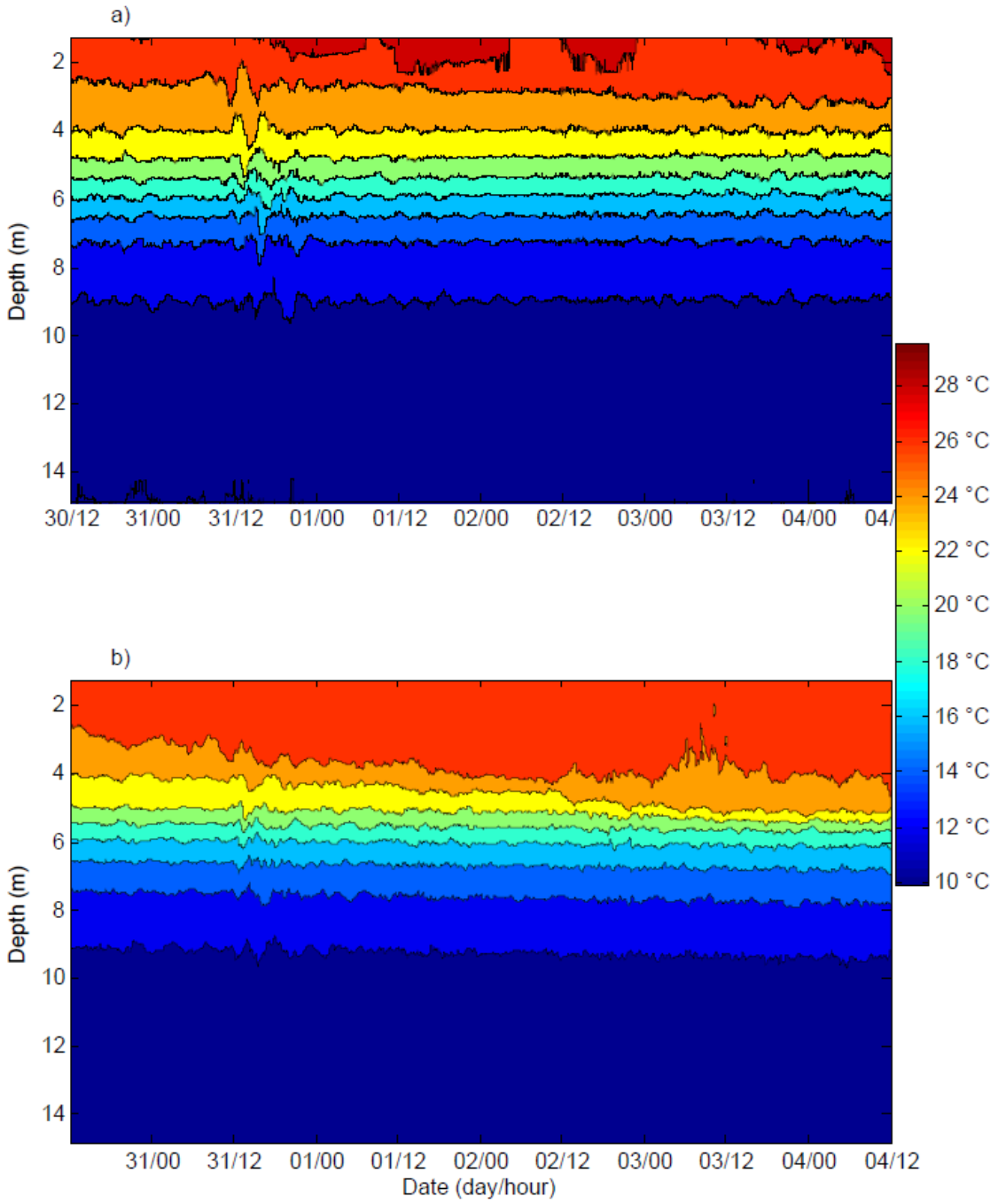

Figure 4.23. Time series temperature profile plot for Simulation 2, measured by the LDS for a) field data and b) ELCOM output at 10 m horizontal grid cell size and 0.1 m vertical grid cell size.

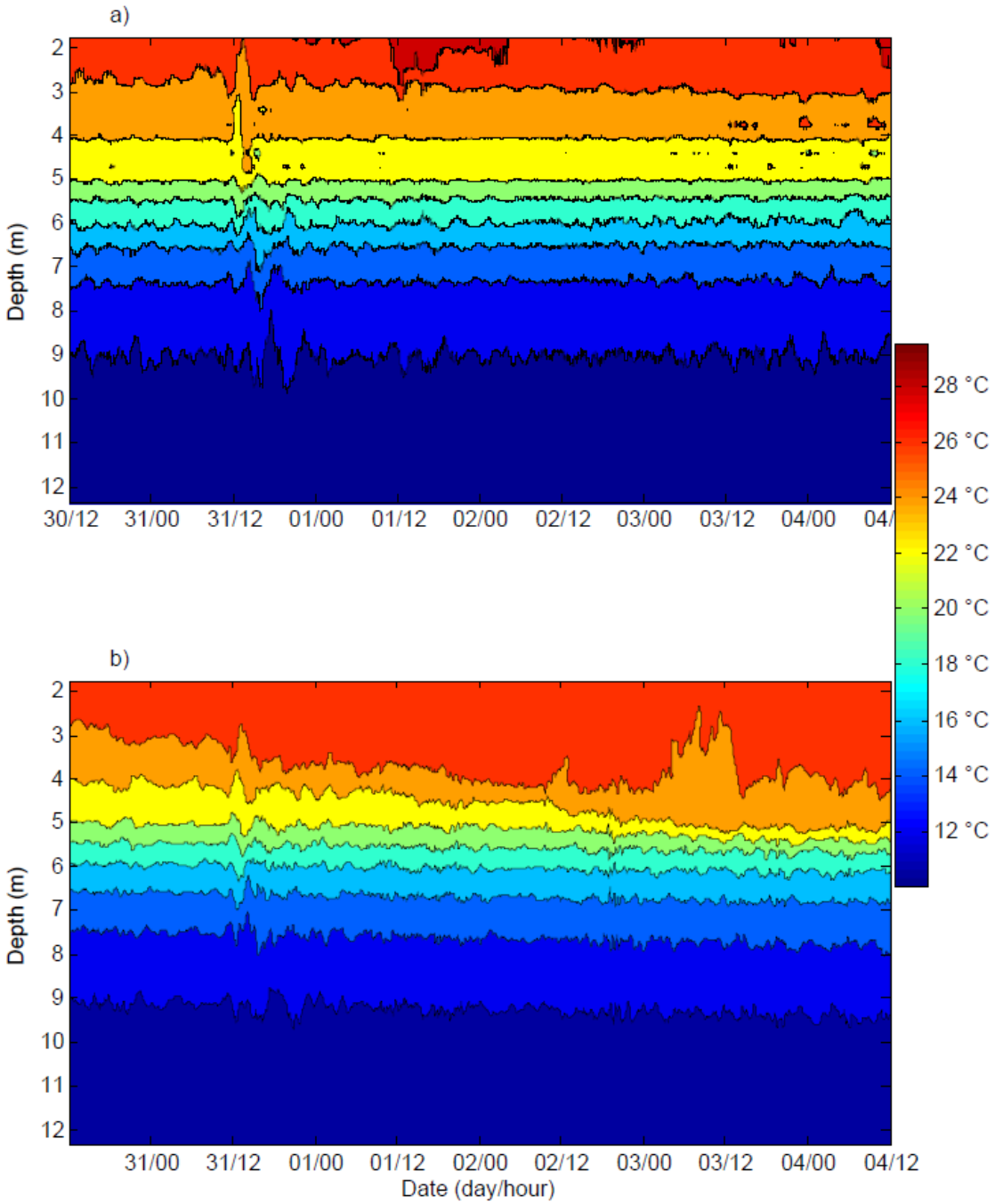

Figure 4.24. Time series temperature profile plot for Simulation 2, measured by T-Chain 52 for a) field data and b) ELCOM output at 10 m horizontal grid cell size and 0.1 m vertical grid cell size.

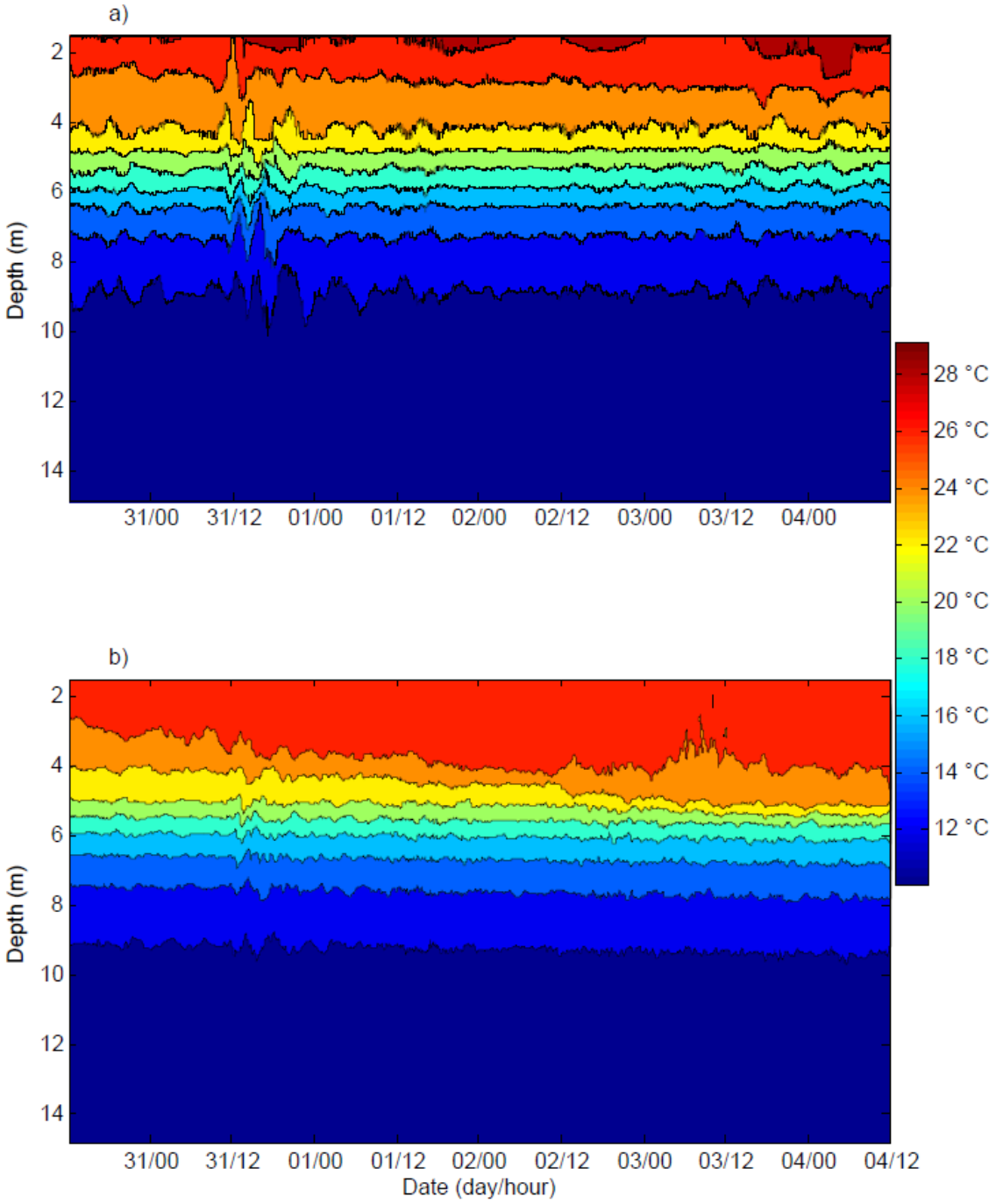

Figure 4.25. Time series temperature profile plot for Simulation 2, measured by T-Chain 53 for a) field data and b) ELCOM output at 10 m horizontal grid cell size and 0.1 m vertical grid cell size.

movement, ELCOM registered very little change. Again, strong winds act to set up internal wave action periodically throughout 1-4 August, causing oscillations measured by the LDS, but the model shows little increase in $\sum E_K$.

Additional model runs for Simulation 2 support the results previously discussed: numerical viscosity appears to damp internal wave amplitudes and drives the isotherms in the metalimnion down, lowering the center of gravity. This results in a decrease in both E_P' and E_K'. Results for E_P' are shown in Figures 4.27-29 for the LDS, T-Chain 52, and T-Chain 53, respectively. Figure 4.27 shows that for the simulations at small grid sizes, model results show a deepening of isotherms in the metalimnion. At higher values of Δz, this deepening effect is reduced, and the model more closely matches field observations in terms of the retention of a vertical thermal structure. Figure 4.28 shows similar results for T-Chain 52; small grid sizes result in lower E_P' values, and larger values for Δz give results much closer to one. Figure 4.29 shows better model performance for T-Chain 53 than compared to the results in Figure 4.28. Smaller grid sizes do show values less than one; however, there is a region for Δz = 0.3 - 0.6 m for Δx = 10 m which gives E_P' values close to one.

Results for E_K' are shown in Figures 4.30-32 for the LDS, T-Chain 52, and T-Chain 53, respectively. All three plots show similar results: kinetic energy is most accurately reproduced for small Δx and Δz and least precisely for higher Δz values. However, small horizontal grid cells do provide acceptable results for Δz = 0.1 - 0.6 m,

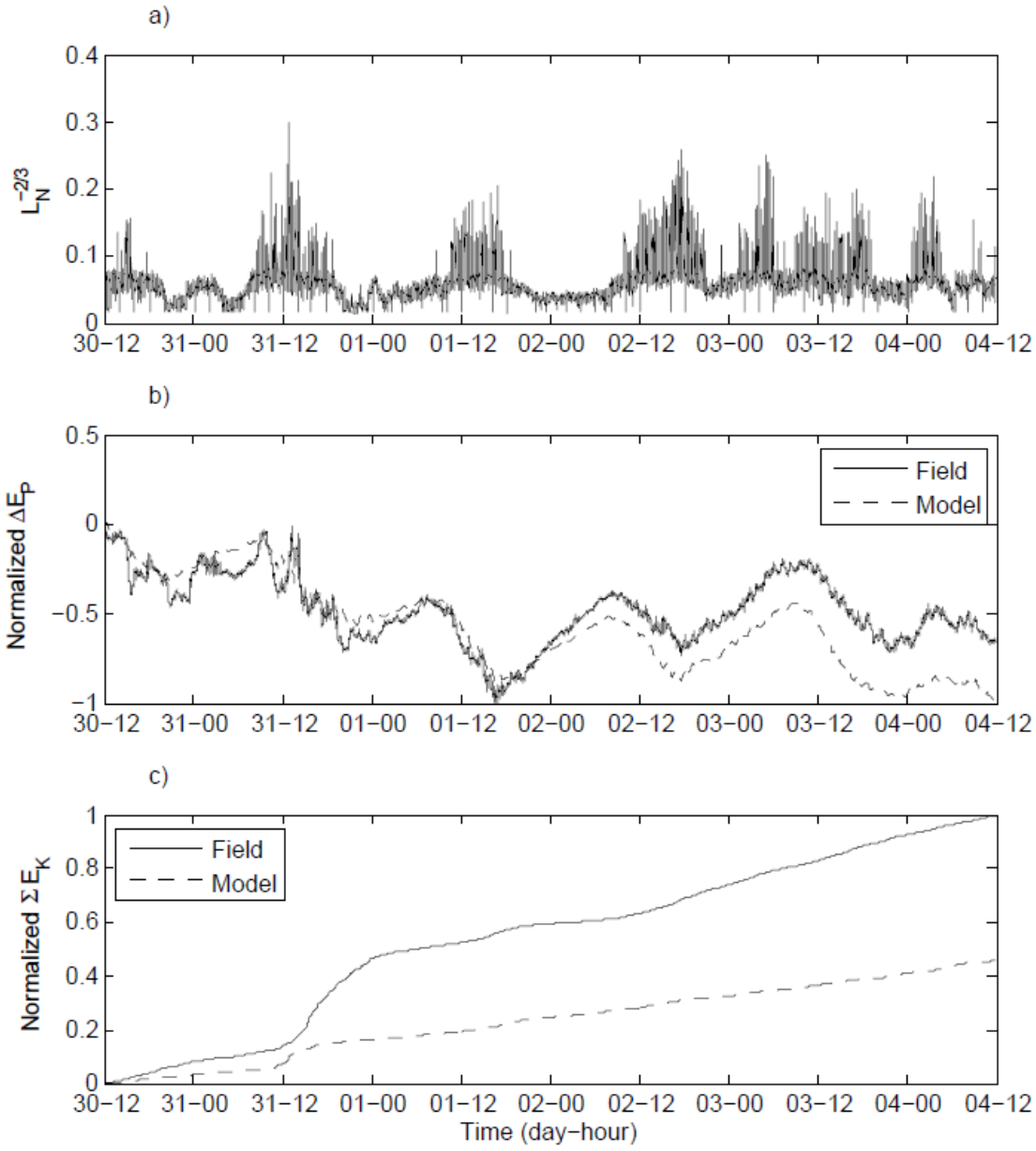

Figure 4.26. The effect of L_N on numerical diffusion and viscosity during Simulation 2 measured by the LDS. a) Time series of $L_N^{-2/3}$, b) change in potential energy, and c) cumulative sum of kinetic energy. Model results shown used Δx = 10 m and Δz = 0.5 m.

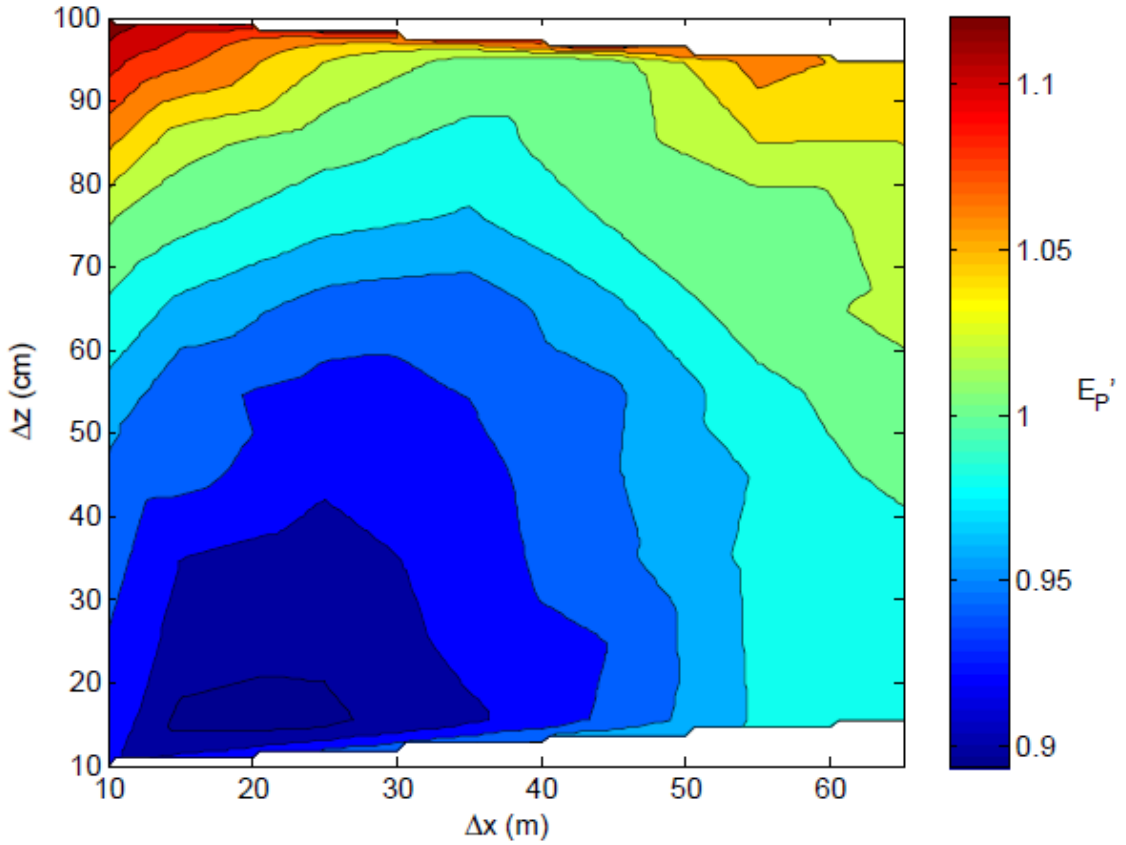

Figure 4.27. Normalized time-integrated potential energy for Simulation 2 measured at the LDS. Horizontal and vertical grid cell size is given by Δx and Δz, respectively.

indicating that E_K' is more sensitive to changes in Δx than Δz. Considering the best case model prediction, ELCOM underestimates by approximately 30%. This underestimation has implications for transport of scalars in the water body (i.e., dissolved oxygen, phytoplankton, nutrients, etc.) Therefore, considering both the reproduction of

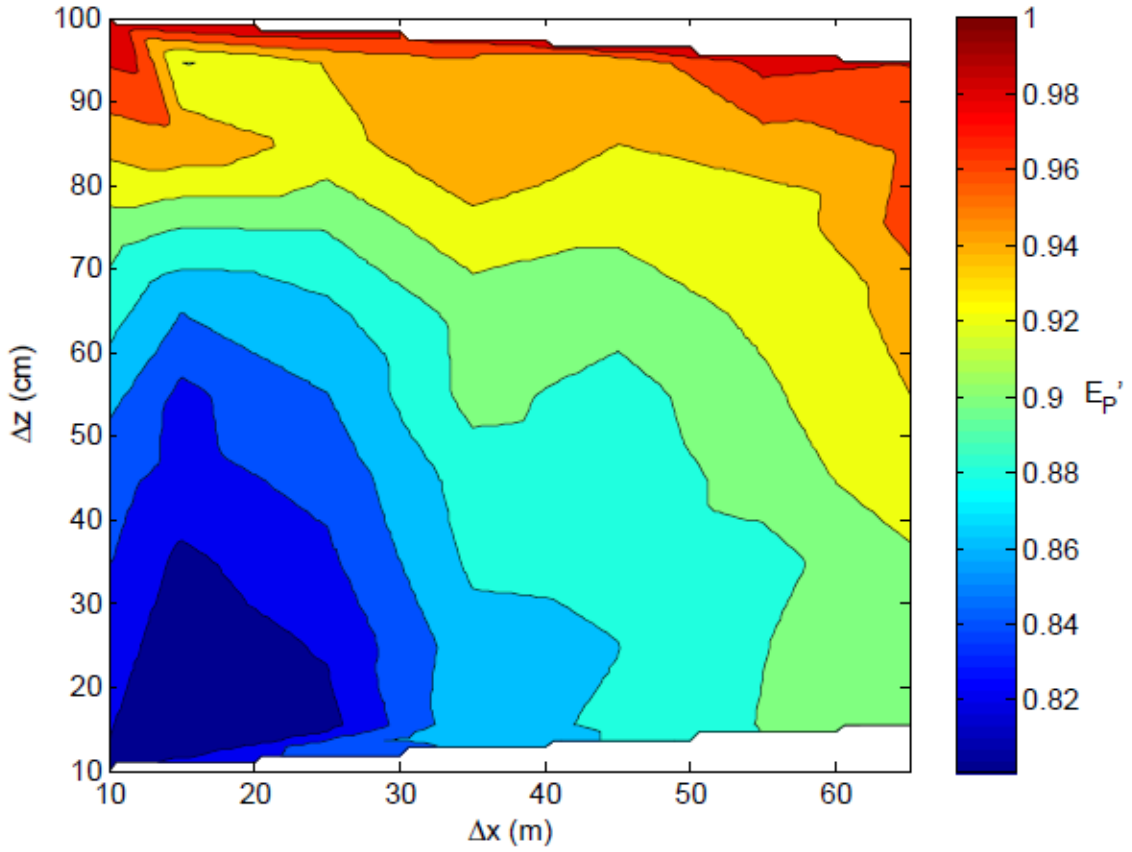

Figure 4.28. Normalized time-integrated potential energy for Simulation 2 measured at T-Chain 52. Horizontal and vertical grid cell size is given by Δx and Δz, respectively.

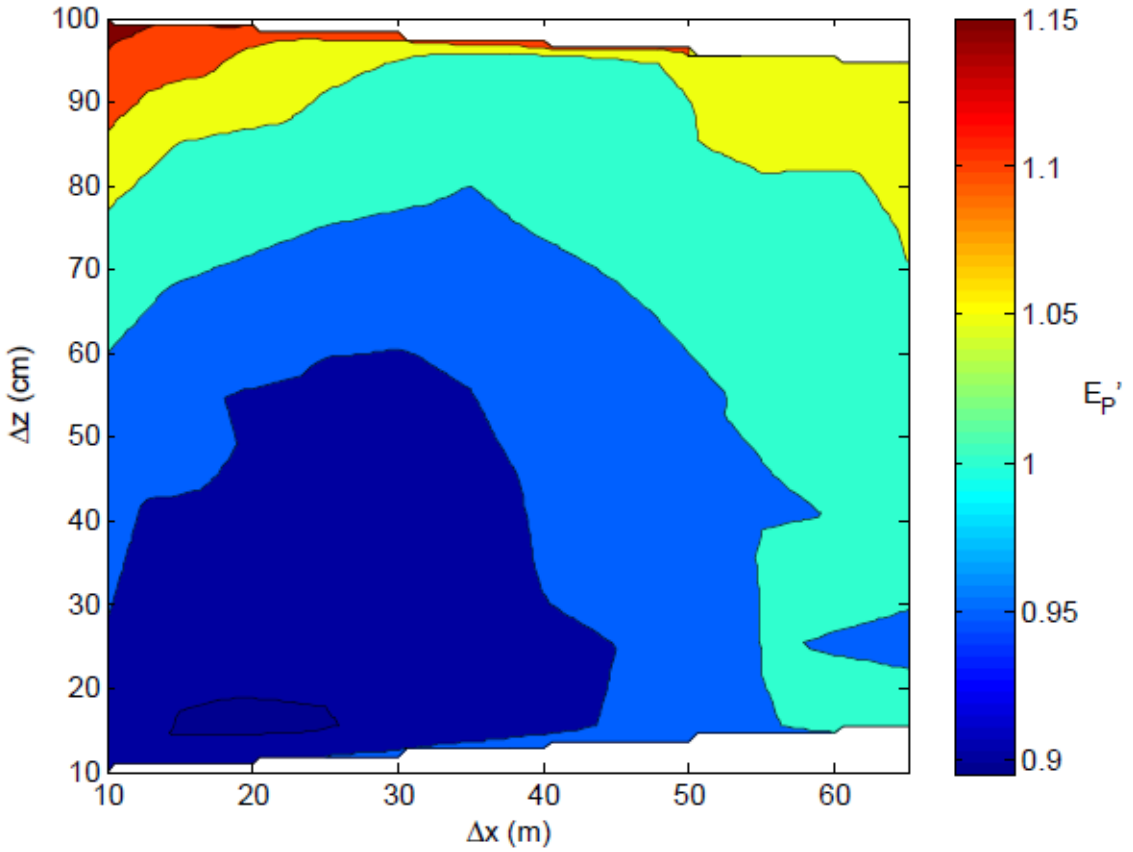

Figure 4.29. Normalized time-integrated potential energy for Simulation 2 measured at T-Chain 53. Horizontal and vertical grid cell size is given by Δx and Δz, respectively.

the internal wave amplitude and maintaining stratification, ELCOM performed best for simulations using Δx = 10 m and Δz = 0.5 - 0.6 m.

Comparing the results from Simulations 1 and 2 offer very different results based on grid size: Δx = 20 m and Δz = 0.1 - 0.2 m yields the best results for Simulation 1 while Δx = 10 m and Δz = 0.5 - 0.6 m provided accurate results for Simulation 2. These

regions were chosen in an attempt to balance errors in potential and kinetic energy values. The region identified for Simulation 1 contains minimal increases in E_P' (approximately 1.35 in Fig. 4.15 and 1.25 in Fig. 4.16) and maximum values for E_K' (approximately 0.6 in Fig. 4.17 and 0.7 in Fig. 4.18). Similarly, the region identified in

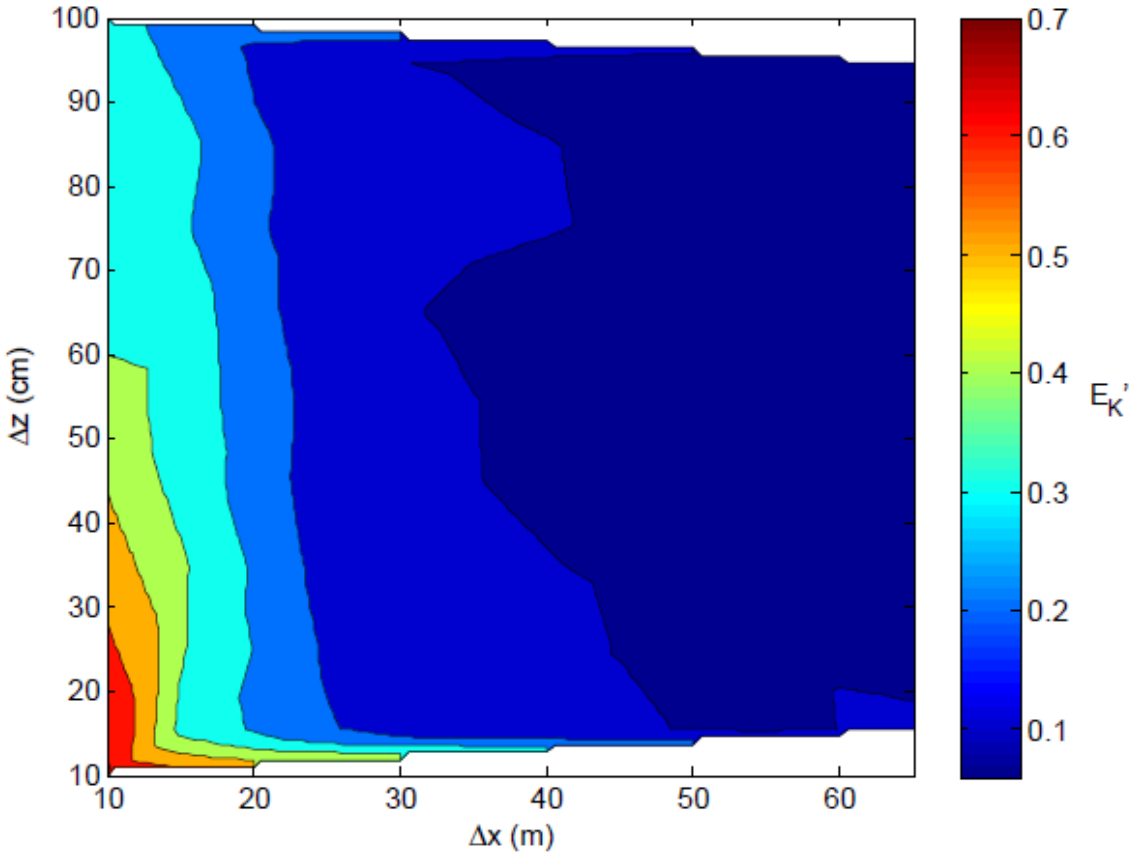

Figure 4.30. Normalized time-integrated kinetic energy for Simulation 2 measured at the LDS. Horizontal and vertical grid cell size is given by Δx and Δz, respectively.

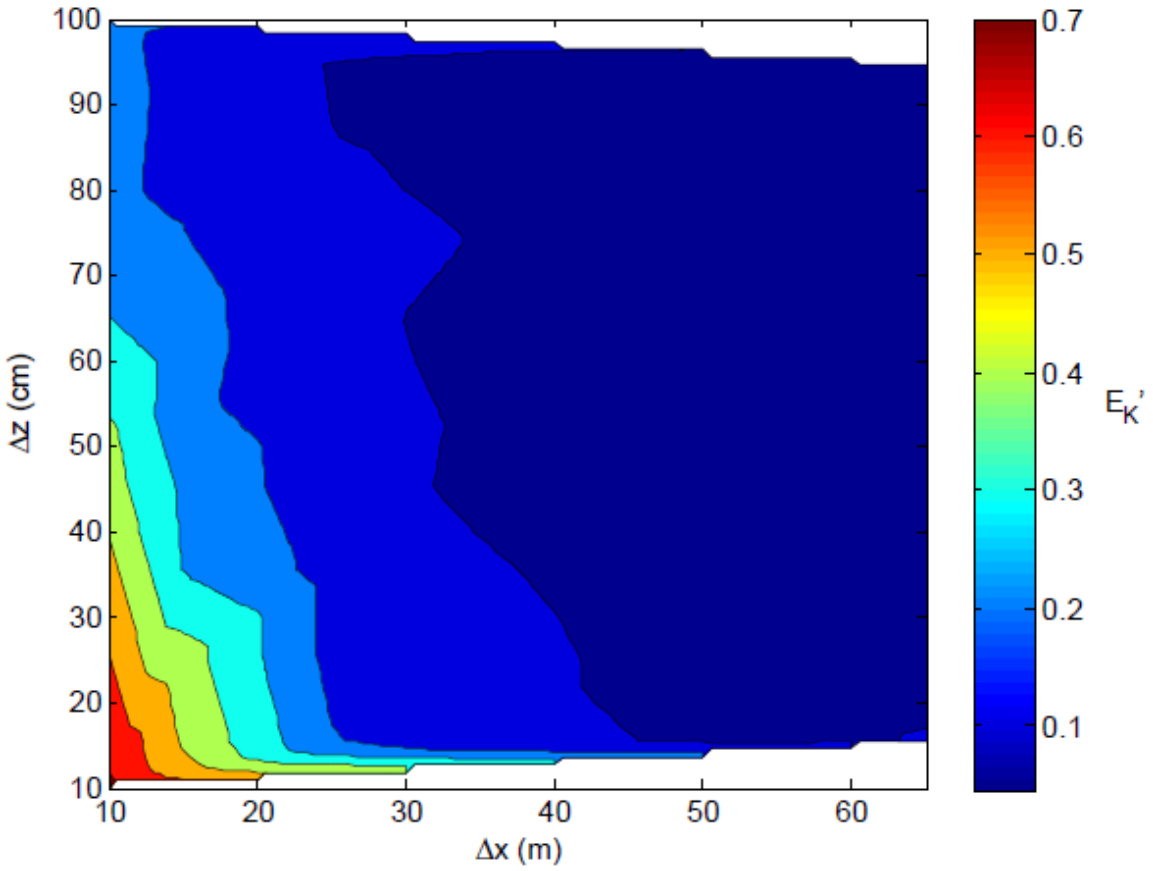

Figure 4.31. Normalized time-integrated kinetic energy for Simulation 2 measured at T-Chain 52. Horizontal and vertical grid cell size is given by Δx and Δz, respectively.

Simulation 2 gives E_P' values closest to one (approximately 0.96 in Fig. 4.27, 0.87 in Fig. 4.28, and between 0.95 and 1 in Fig. 4.29) and the highest values for E_K' (approximately 0.4 in Fig. 4.30, 0.3 in Fig. 4.31, and 0.4 in Fig. 4.32). None of the model runs for Simulation 2 recovered E_K' values close to 100%. This could be due to model

errors in calculating momentum input, in the vertical mixing model, or damping due to numerical viscosity in the advection scheme.

To assess ELCOM's ability to reproduce internal vertical motions, power spectra of the displacement of the 17°C isotherm were calculated from both field and model results (Fig. 4.33). The model power spectra match field results at low frequencies, particularly in reproducing the troughs in the spectral density at 0.6 and 1.3 cpd.

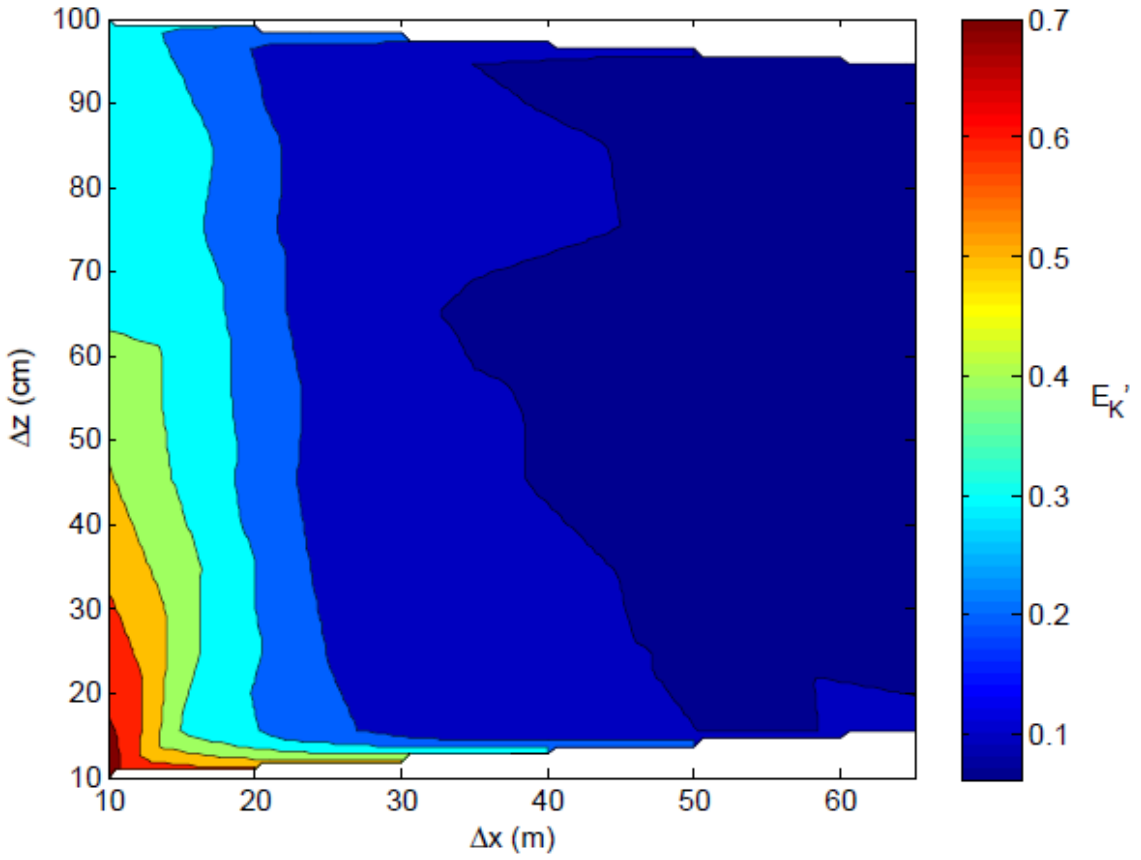

Figure 4.32. Normalized time-integrated kinetic energy for Simulation 2, measured by T-Chain 53. Horizontal and vertical grid cell size is given by Δx and Δz, respectively.

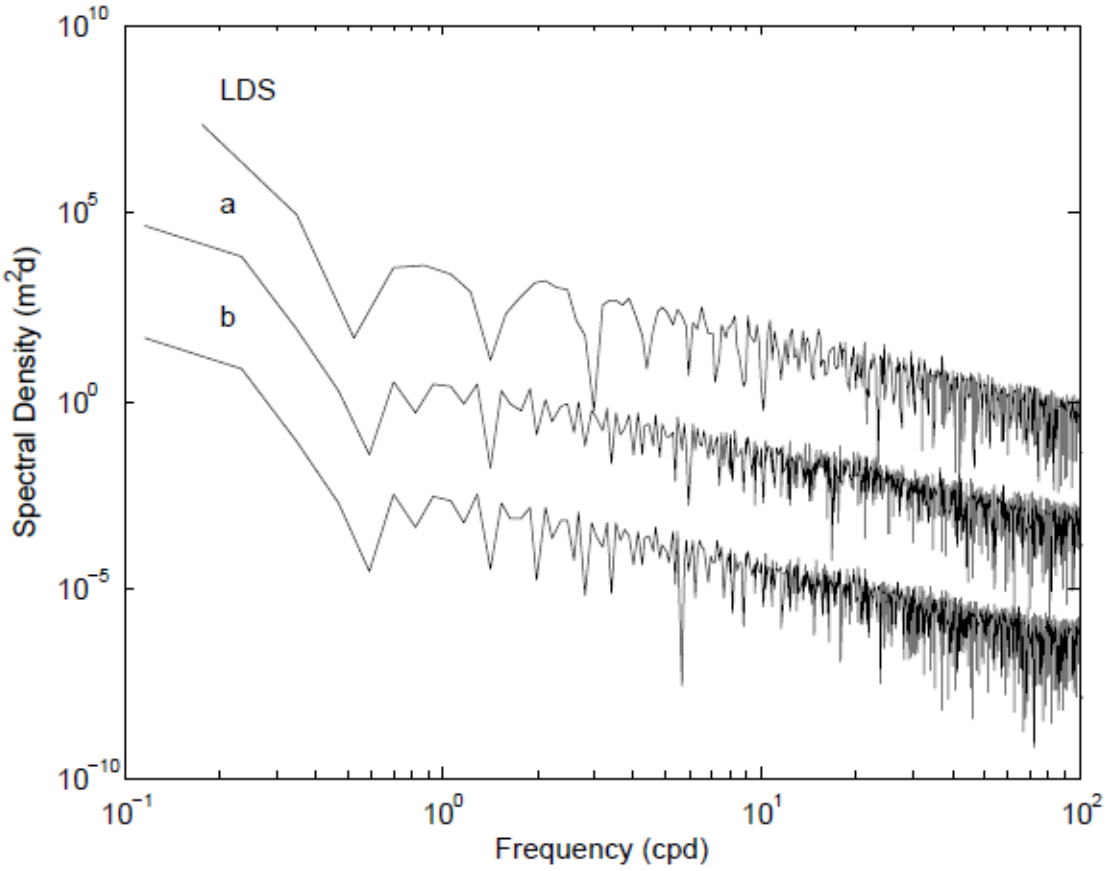

Figure 4.33. Spectral density of the displacement of the 17°C isotherm during Simulation 2. Isotherm displacement measured by the LDS and calculated using model output with a) Δx = 10 m, Δz = 0.1 m, and b) Δx = 10 m, Δz = 0.5 m. The vertical offset for each spectra is 10^3, beginning with a).

Figure 4.34 shows the comparison of the 17°C isotherm between field observations and model results. A large amount of the points lie above the 1:1 line, indicating ELCOM overpredicting the isotherm depths, as in Simulation 1. *WS* values for all model runs are shown in Figure 4.35 as a function of grid size. Skill assessment

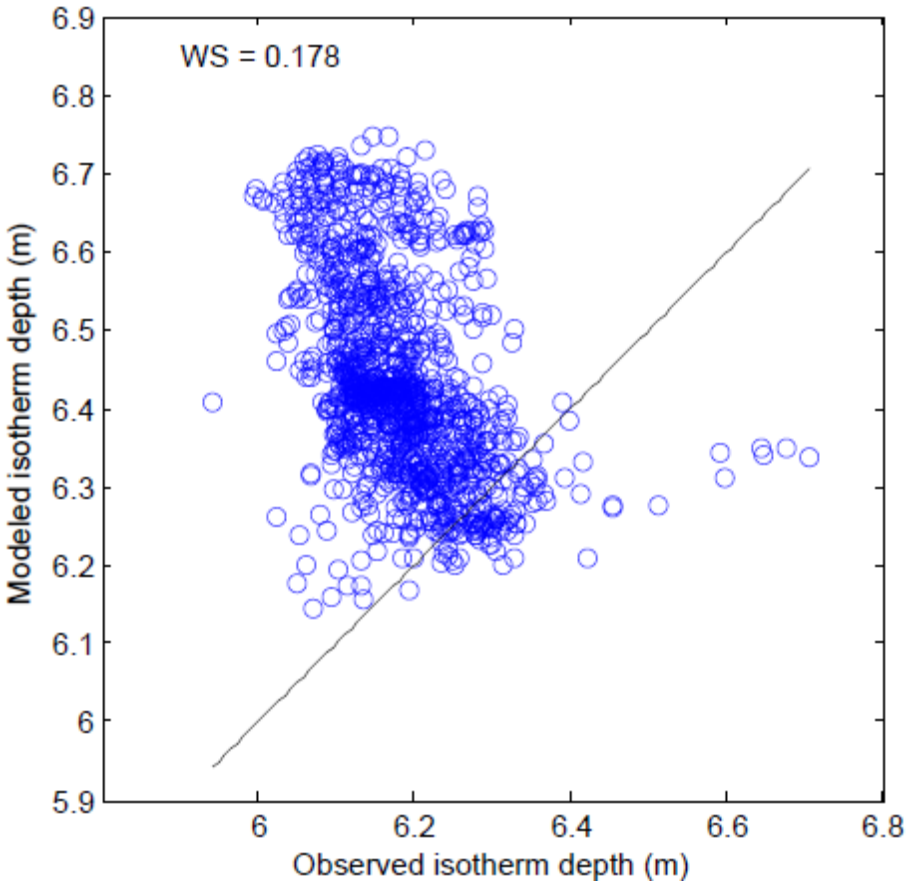

Figure 4.34. Observed and modeled 17°C isotherm depth for Simulation 2 (blue circles) with Δx = 10 m and Δz = 0.5 m. The Willmott skill number and 1:1 line is shown in black.

results from the LDS (Fig. 4.35a) show highest *WS* values of approximately 0.24 for small vertical grid sizes of Δz =0.1-0.2 m and a wider range in the horizontal grid size with Δx =10-30 m. Results from T-Chain 52 (Fig 4.35b) show slightly different results in that the region of best skill is for $\Delta z = 0.2 - 0.4$ m and Δx =15-25 m yielding *WS* = 0.21-0.22. This region corresponds to a coarser vertical grid than identified in Figure

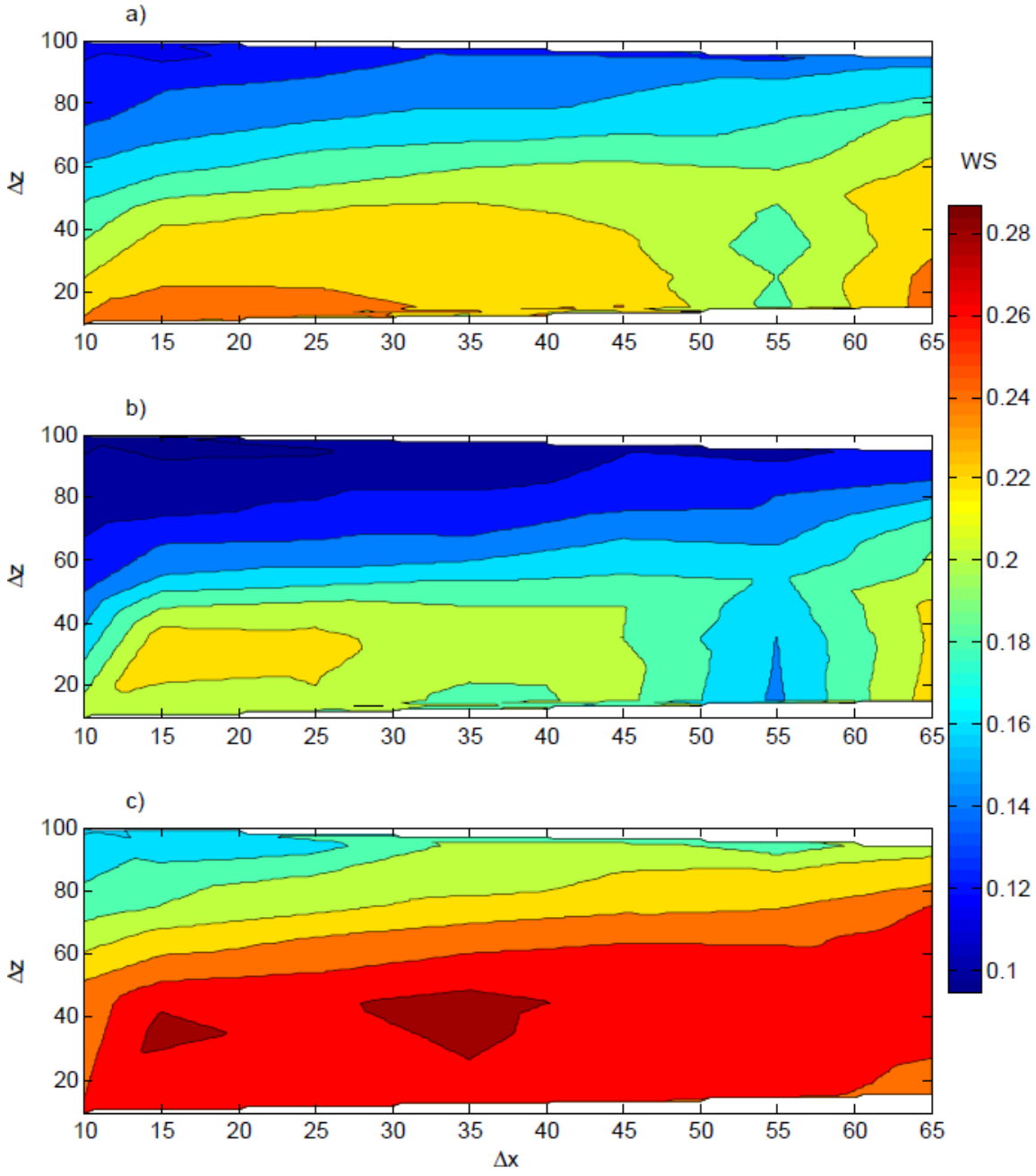

Figure 4.35. *WS* from Simulation 2, values shown for grid sizes in the horizontal (Δx) and vertical (Δz) from a) LDS, b) T-Chain 52, and c) T-Chain 53.

4.35a. The results shown in Figure 4.35c for T-Chain 53 are similar to the results from T-Chain 52, except higher WS values of 0.26-0.28 for $\Delta z = 0.2 - 0.4\,\text{m}$ and Δx =15-35 m.

Simulation 3: Low Lake number

The third simulation period consists of 6-18 July 2009 at West Okoboji Lake. This period experienced stronger winds than Ada Hayden Lake with less stratification, resulting in greater internal wave amplitudes. The initial stratification and mode shape is shown in Figure 4.36. The LDS was deployed in 25 m deep water; however, the deepest section of West Okoboji Lake approaches 43 m. To fill in the missing temperature data at depths greater than 25 m, data were obtained from Iowa State University Limnology Laboratory, which measured temperature to a depth of 40 m. The phase speed c_n corresponding to the temperature profile in Figure 4.36 was calculated as 0.28 m/s and the wave period is approximately 13 hours. A total of 56 simulations was run for this event, with different grid sizes in the horizontal (Δx), vertical (Δz), and model time steps (Δt) (Table 4.4).

Model results are compared to field observations for Simulation 3 for the locations of both the LDS and T-Chain 52. ELCOM reproduced internal motions but did not accurately match temperatures in both the surface layer and hypolimnion (Fig. 4.37). Field measurements showed surface heating from 11-14 July; while ELCOM did give some periodic heating, the result was not to the same extent as observed in the field. Additionally, the 14°C isotherm was measured to oscillate at a depth of approximately 20

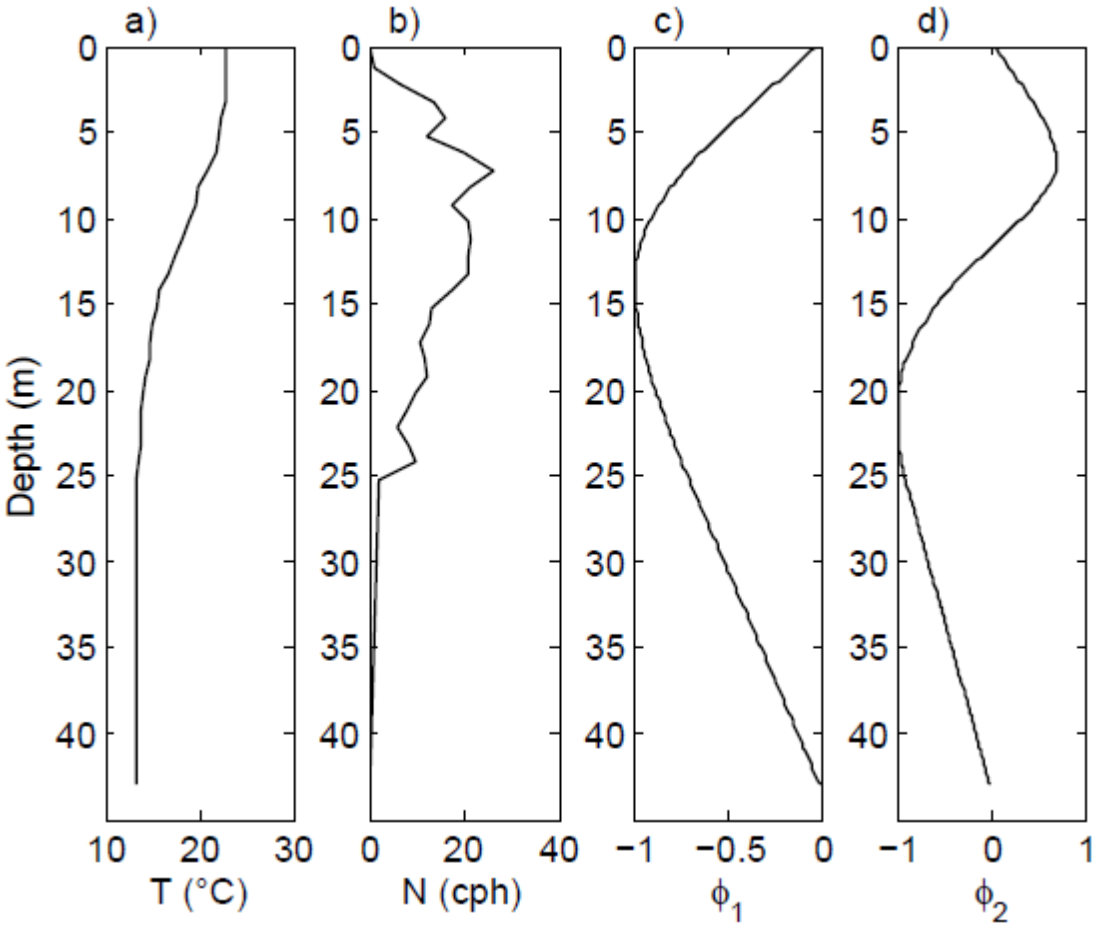

Figure 4.36. Profiles for West Okoboji Lake using field measurements from the LDS thermistor chain for Simulation 3 (a) Temperature profile used for computing the vertical modes, (b) buoyancy frequency based on (a). (c) and (d) show the mode shape for the first and second vertical mode, respectively.

m throughout the simulation period. However, ELCOM shows the isotherm to deepen past 25 m beginning 9 July. The metalimnion also appears to thicken. More precisely, the 20°C isotherm was shallower in the model results than measured in the field, while

Table 4.4 ELCOM resolutions for model runs of Simulation 3. Here Δx gives the horizontal grid size such that $\Delta x = \Delta y$, Δz is the vertical grid size, and Δt is the model time step.

Δx (m)	Δz (cm)	Δt (s)	Δx (m)	Δz (cm)	Δt (s)	Δx (m)	Δz (cm)	Δt (s)
50	50	60	100	100	120	250	175	300
"	60	"	"	110	"	"	200	"
"	70	"	"	120	"	300	120	350
"	80	"	"	130	"	350	50	425
"	90	"	"	140	"	"	60	"
"	100	"	"	150	"	"	70	"
"	110	"	"	175	"	"	80	"
"	120	"	"	200	"	"	90	"
"	130	"	150	50	180	"	100	"
"	140	"	"	60	"	"	110	"
"	150	"	"	70	"	"	120	"
"	175	"	"	80	"	"	130	"
"	200	"	"	90	"	"	140	"
75	50	90	"	100	"	"	150	"
"	60	"	"	110	"	"	175	"
"	70	"	"	120	"	"	200	"
"	80	"	"	130	"	450	50	550
"	90	"	"	140	"	"	60	"
"	100	"	"	150	"	"	70	"
"	110	"	"	175	"	"	80	"
"	120	"	"	200	"	"	90	"
"	130	"	250	60	300	"	100	"
"	140	"	"	70	"	"	110	"
"	150	"	"	80	"	"	120	"
"	175	"	"	90	"	"	130	"
"	200	"	"	100	"	"	140	"
100	50	120	"	110	"	"	150	"
"	60	"	"	120	"	"	175	"
"	70	"	"	130	"	"	200	"
"	80	"	"	140	"			
"	90	"	"	150	"			

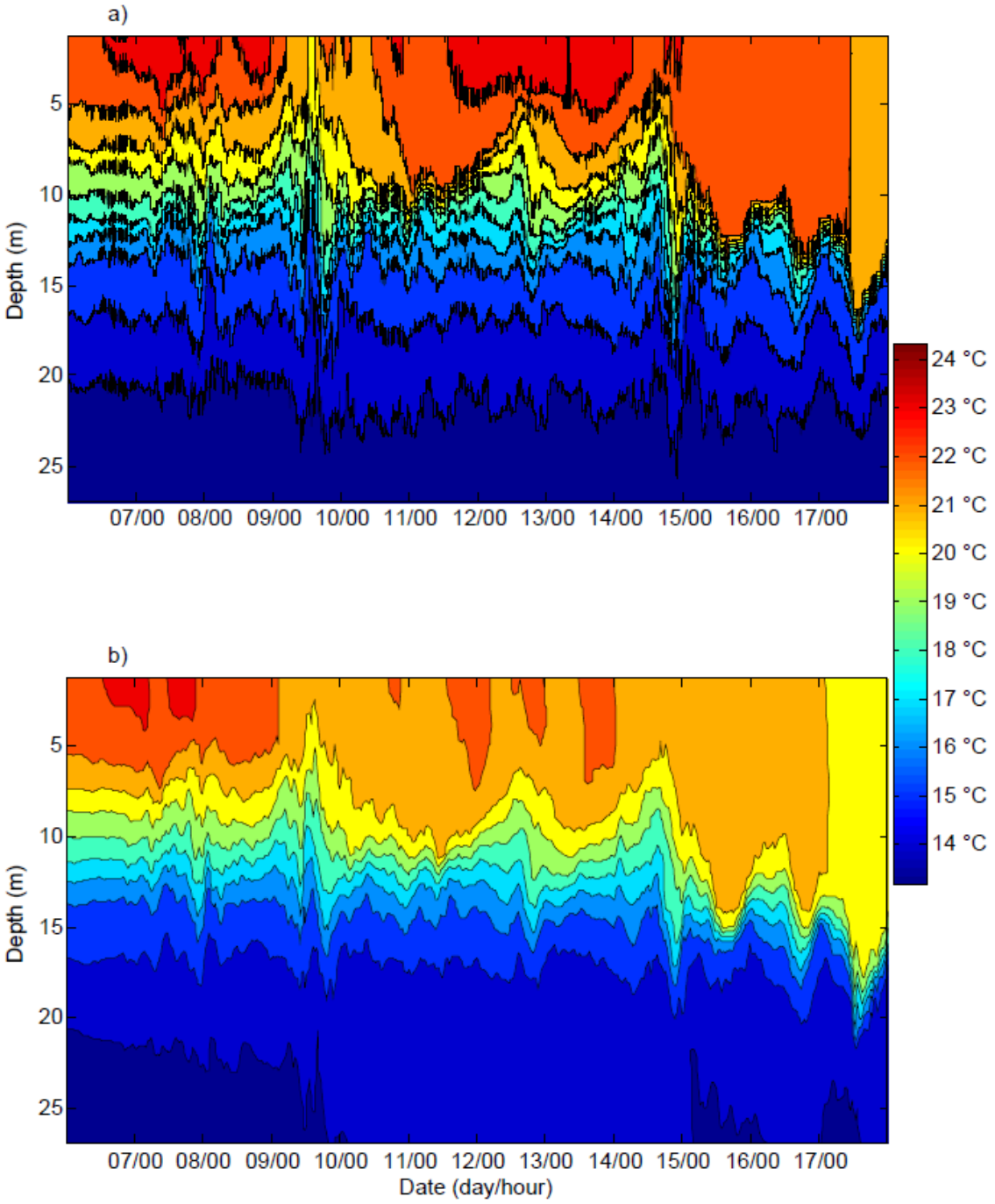

Figure 4.37. Time series temperature profile plot for Simulation 3, measured by the LDS for a) field data and b) ELCOM output at 50 m horizontal grid cell size and 1 m vertical grid cell size.

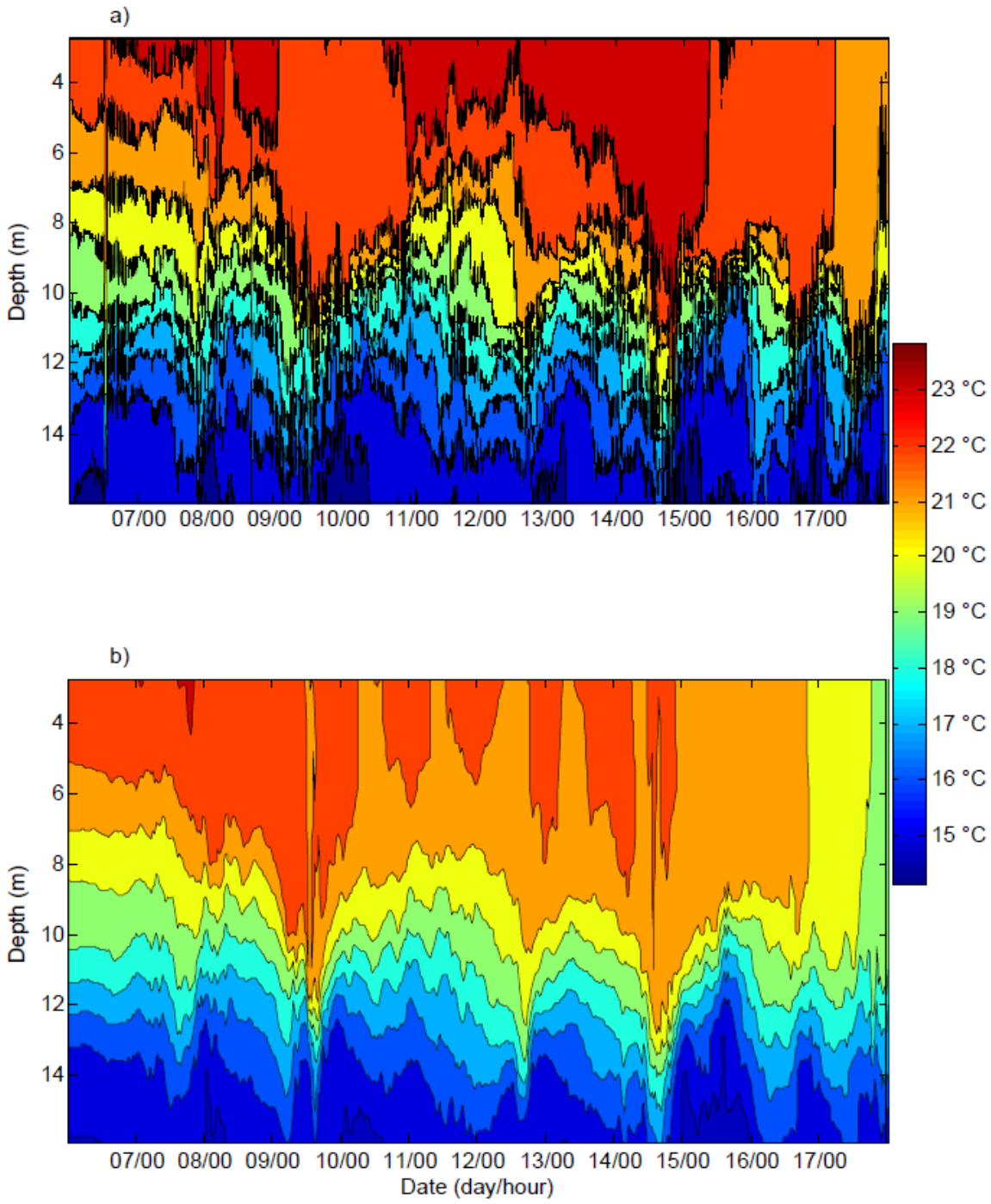

Figure 4.38. Time series temperature profile plot for Simulation 3, measured by T-Chain 52 for a) field data and b) ELCOM output at 50 m horizontal grid cell size and 1 m vertical grid cell size.

the 15°C isotherm was deeper according to the model. The results from T-Chain 52 (Fig. 4.38) are similar to those measured by the LDS. The internal wave motions are reproduced in terms of phase, but the amplitudes appear to be slightly damped. As was the case at the LDS, ELCOM underestimated surface heating, resulting in the surface layer approximately 1°C cooler than was measured in the field. The model predicts much of the low-frequency motion but not the high-frequency oscillations, probably because Δt > 15 s, the sampling time of the thermistor chains. Figure 4.39 shows how L_N, ΔE_P, and $\sum E_K$ vary with time.

Overall, the potential energy based on model results appears to match field observations quite well (Fig. 4.39b). Towards the end of the simulation, a spiked increase in L_N causes an increase in the potential energy. The kinetic energy is not as accurately modeled (Fig. 4.39c), as the model shows a consistent underestimation. Therefore, numerical diffusion and numerical dissipation appear to affect the model results: the model is initially damped and stratification is well modeled, but under strong forcing conditions associated with a decrease in L_N in the model shows elevated diffusion and an increase in kinetic energy.

Values for E_P' measured at the LDS are shown in Figure 4.40 for simulations using different resolutions. The results show best model performance for Δx in the range of 50-100 m and Δz between 1-2 m. The worst results are for Δx = 250 m for all vertical grid sizes. Potential energy begins to decrease again for a horizontal grid greater than 300 m. The results from E_P' values calculated from T-Chain 52 are shown in Figure

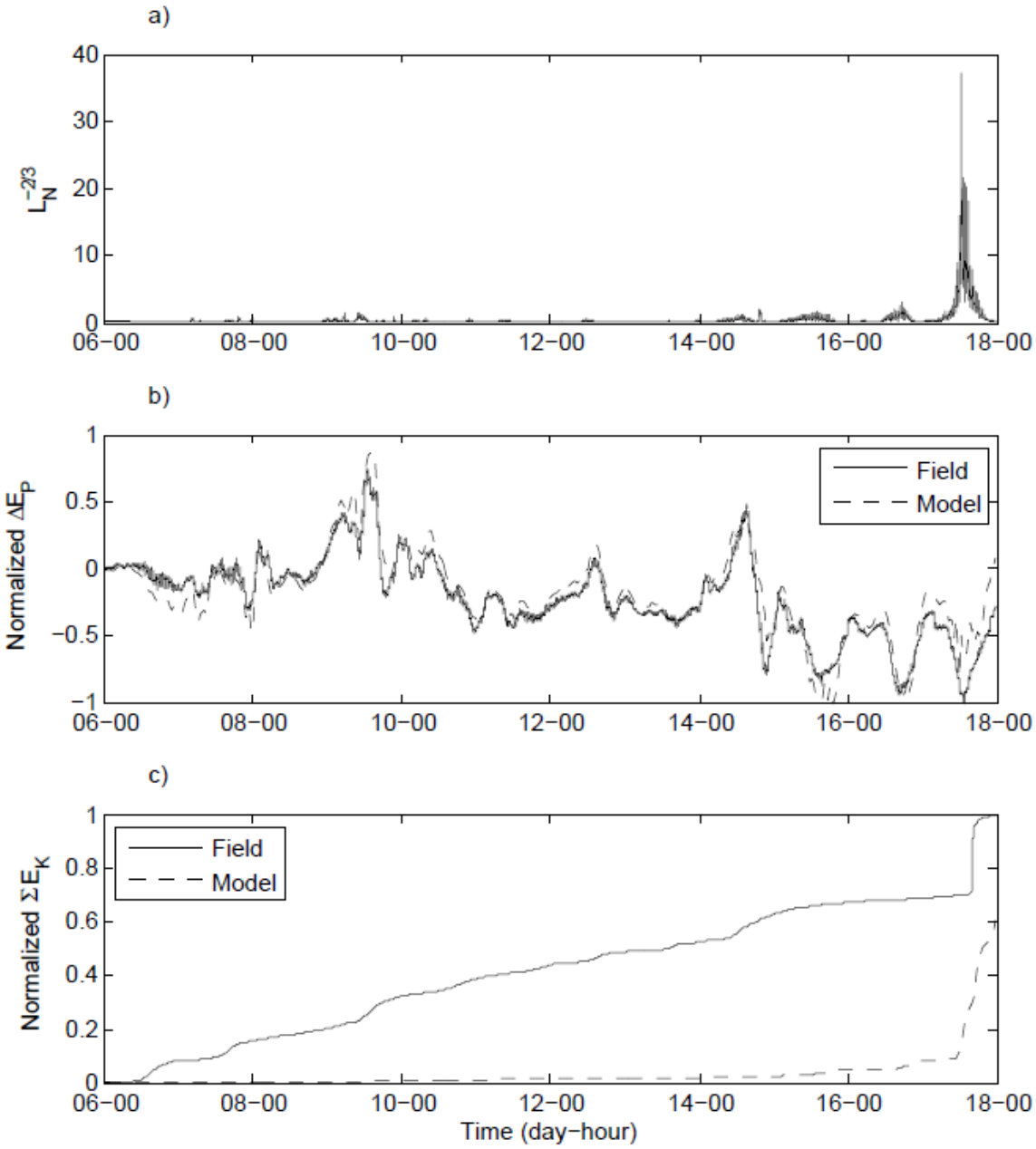

Figure 4.39. The effect of L_N on numerical diffusion and viscosity during Simulation 3 measured by the LDS. a) Time series of $L_N^{-2/3}$, b) change in potential energy, and c) cumulative sum of kinetic energy. Model results shown used Δx = 50 m and Δz = 1 m.

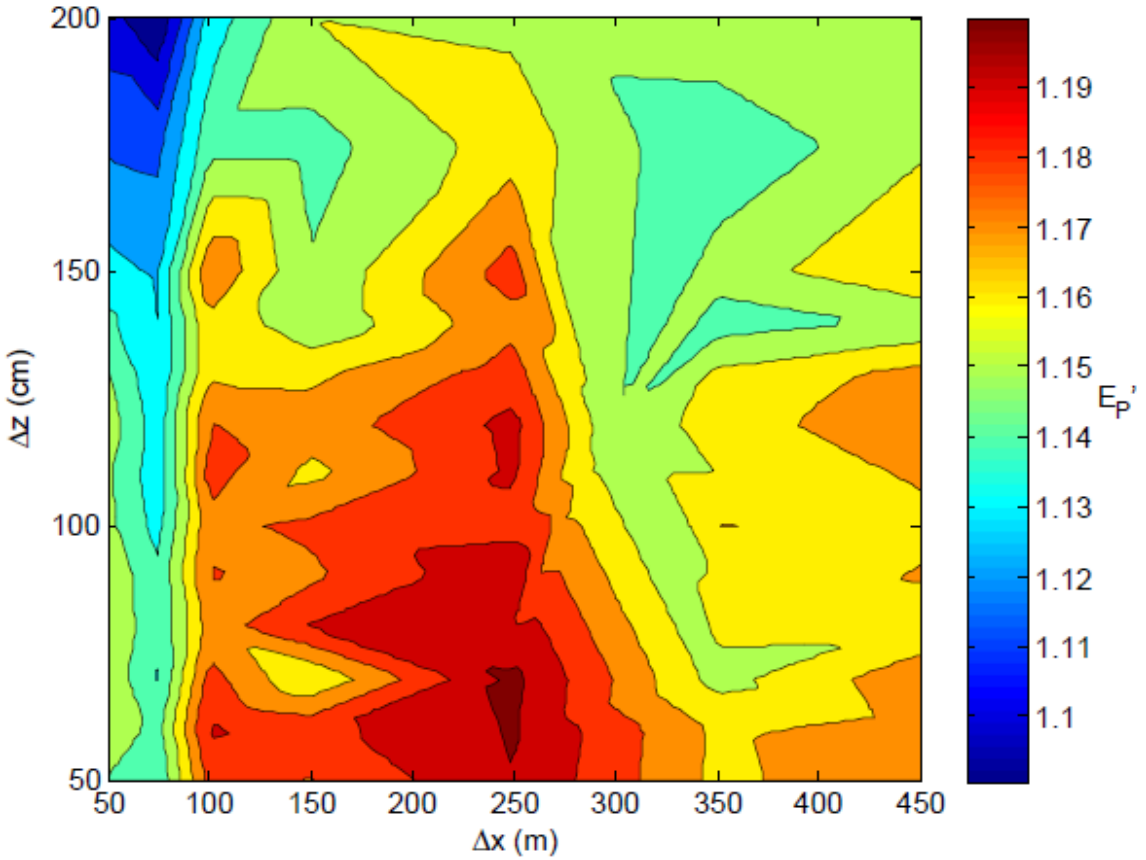

Figure 4.40. Normalized time-integrated potential energy for Simulation 3 at the LDS. Horizontal and vertical grid cell size is given by Δx and Δz, respectively.

4.41. Here, ELCOM performs best for high vertical grid sizes, similar to the results calculated from the LDS. The results appear to be almost independent of the vertical resolution for a set Δx with near constant values along Δx = 75, 200, 300, 350, and 400m. Only until the vertical grid size is in the range of 1-1.5 m does the vertical resolution appear to become important. Examining both Figures 4.40-41, the best results are for high horizontal resolution with a vertical grid cell size of 1-1.25 m. For results

from both the LDS and T-Chain 52, the model agreement is within 10-30% of field observations.

Values for E_K' are shown in Figures 4.42 and 4.43 for the LDS and T-Chain 52, respectively. Both figures have similar results in terms of the effect of horizontal grid size: between 10-70% of the kinetic energy is recovered, with smaller Δx yields higher values of E_K'. The difference between the two figures is the effect Δz has on the results.

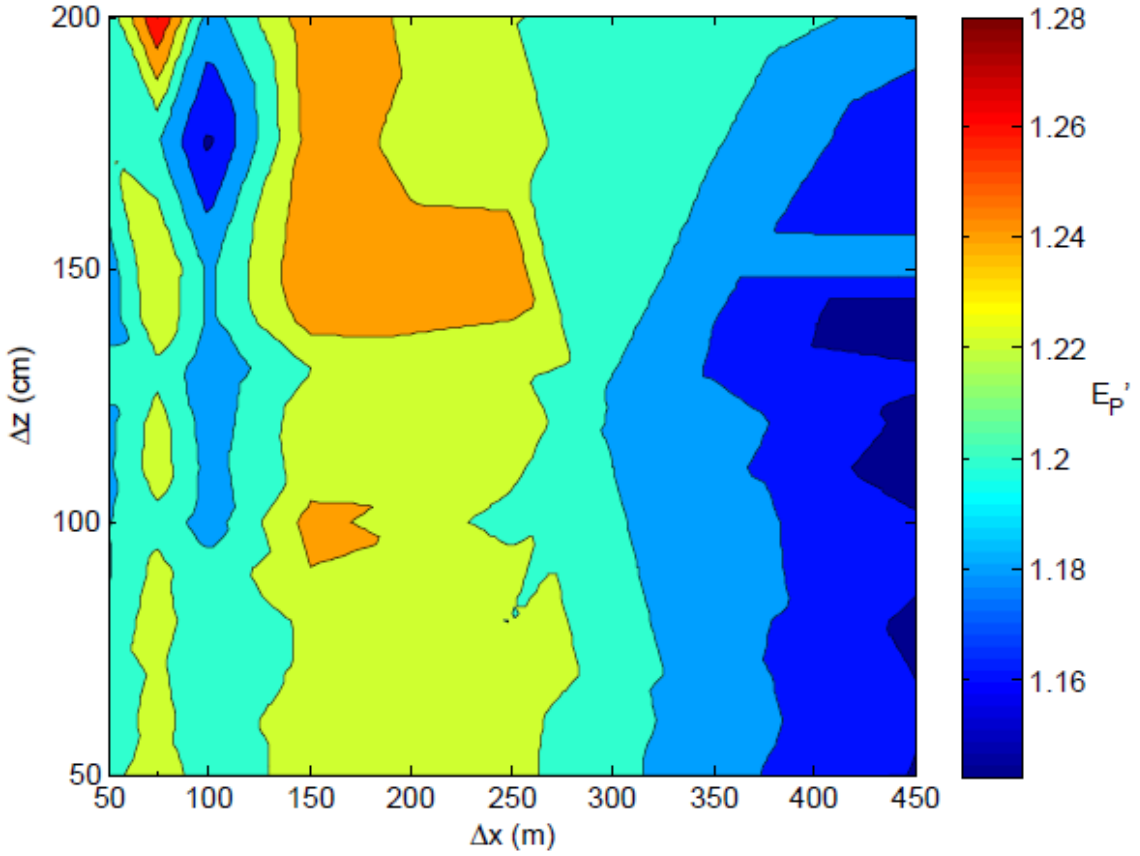

Figure 4.41. Normalized time-integrated potential energy Simulation 3 at T-Chain 52. Horizontal and vertical grid cell size is given by Δx and Δz, respectively.

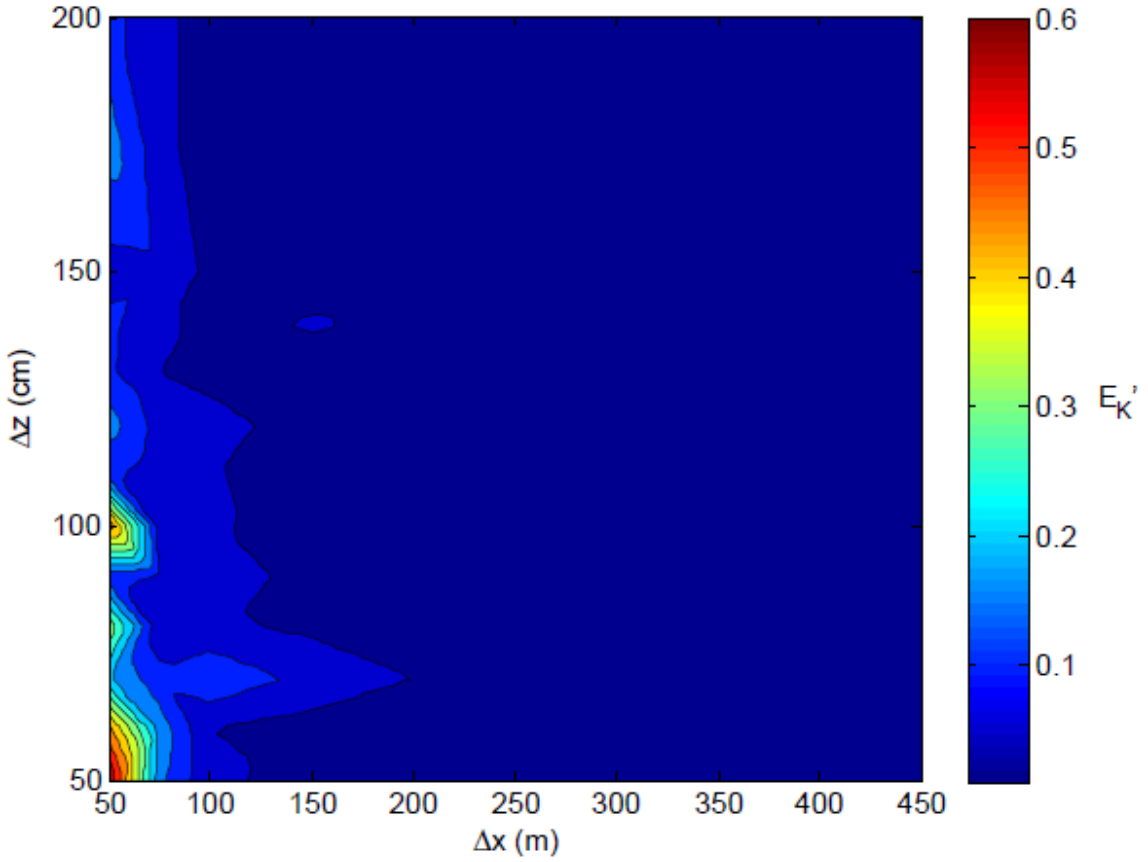

Figure 4.42. Normalized time-integrated kinetic energy for Simulation 3 at the LDS. Horizontal and vertical grid cell size is given by Δx and Δz, respectively.

Figure 4.42 shows concentrated areas where upwards of 60% of the kinetic energy is reproduced. These areas are along Δx = 50 m and a vertical grid cell size of 0.5 and 1 m. Figure 4.39 shows similar areas, but less concentrated in terms of vertical resolution. For small vertical grid size, results are acceptable, but the model performed best for Δz = 1-1.5 m. Therefore, considering both the recovery of kinetic energy and limiting the effects

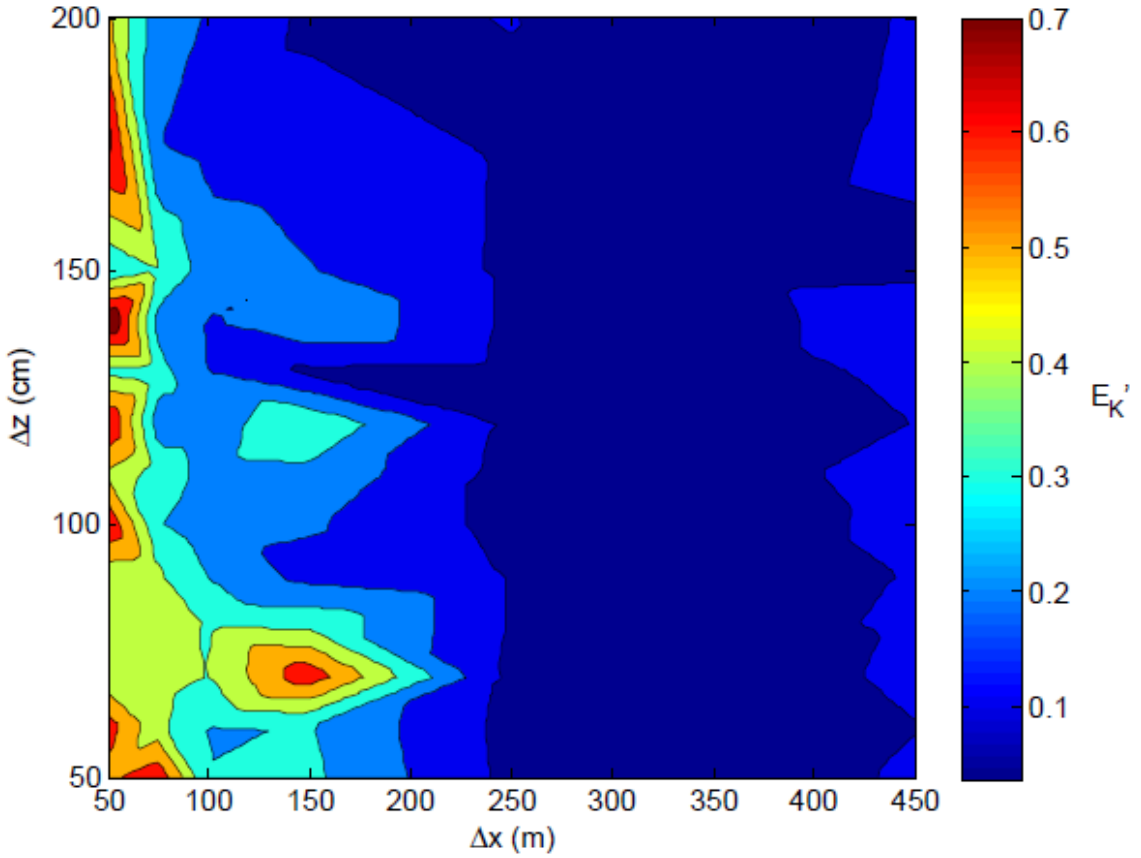

Figure 4.43. Normalized time-integrated kinetic energy for Simulation 3 at T-Chain 52. Horizontal and vertical grid cell size is given by Δx and Δz, respectively.

of diffusion, best model results were obtained for a find horizontal grid with a vertical grid between 1-1.25 m.

Simulation 3 provided different results than either of the first two events. There was much more variability in the potential energy plots: best results at finer horizontal grid sizes, shifting to higher potential energies in the approximate range of Δx = 150 - 250 m, then decreasing $E_P{}'$ values with increases in Δx. The kinetic energy plots

behaved similarly to both previous simulations: lower horizontal grid sizes gave the best recovery of kinetic energy. Simulations 2 and 3 had similar regions where the model most closely agreed with field observations: the smallest horizontal grid size used (Δx = 10 m for Simulation 2 and Δx = 50 m in Simulation 3) and vertical grid sizes slightly

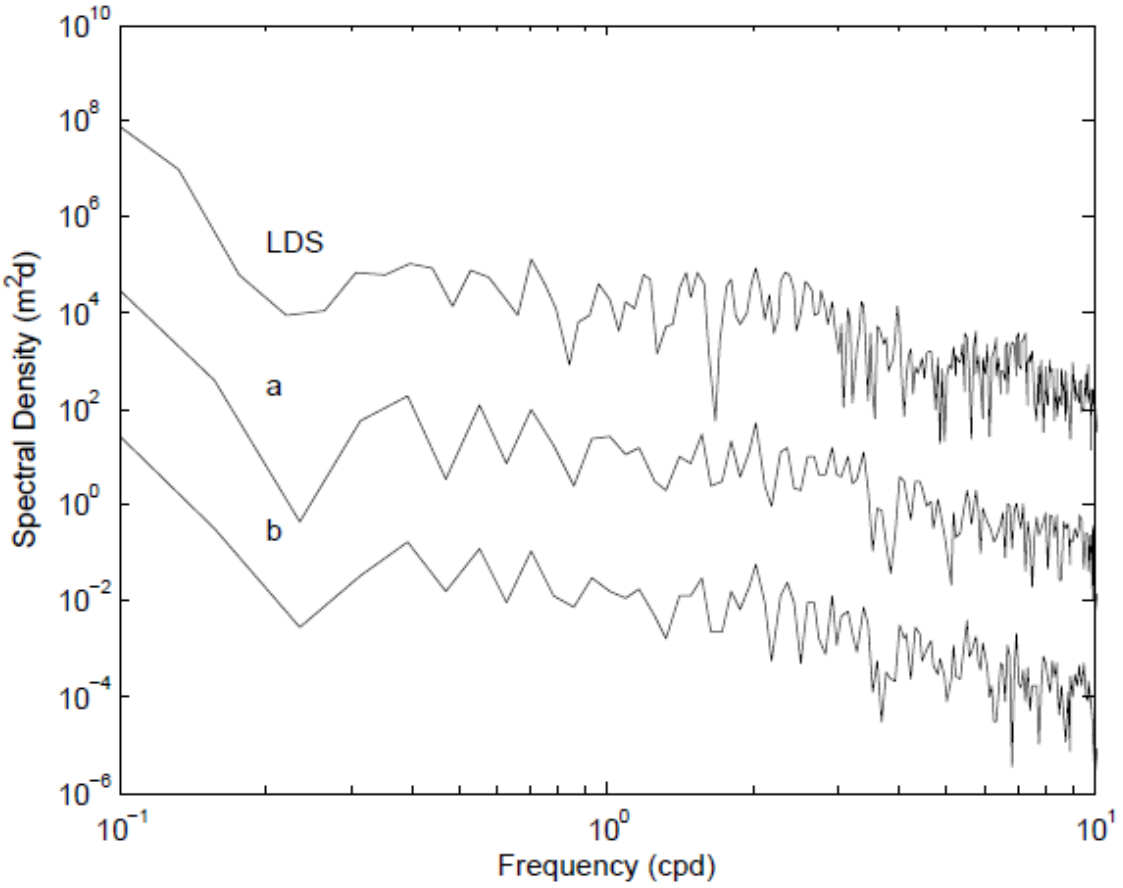

Figure 4.44. Spectral density of the displacement of the 18.5°C isotherm during Simulation 3. Isotherm displacement measured by the LDS and calculated using model output with a) Δx = 50 m, Δz = 0.5 m, and b) Δx = 50 m, Δz = 1.5 m. The vertical offset for each spectra is 10^3, beginning with a).

larger than the minimum values (Δz = 0.5 - 0.6 m for Simulation 2 and Δz = 1 - 1.25 m for Simulation 3). This is in contrast to Simulation 1, where the vertical grid size was minimized and the horizontal grid size was increased.

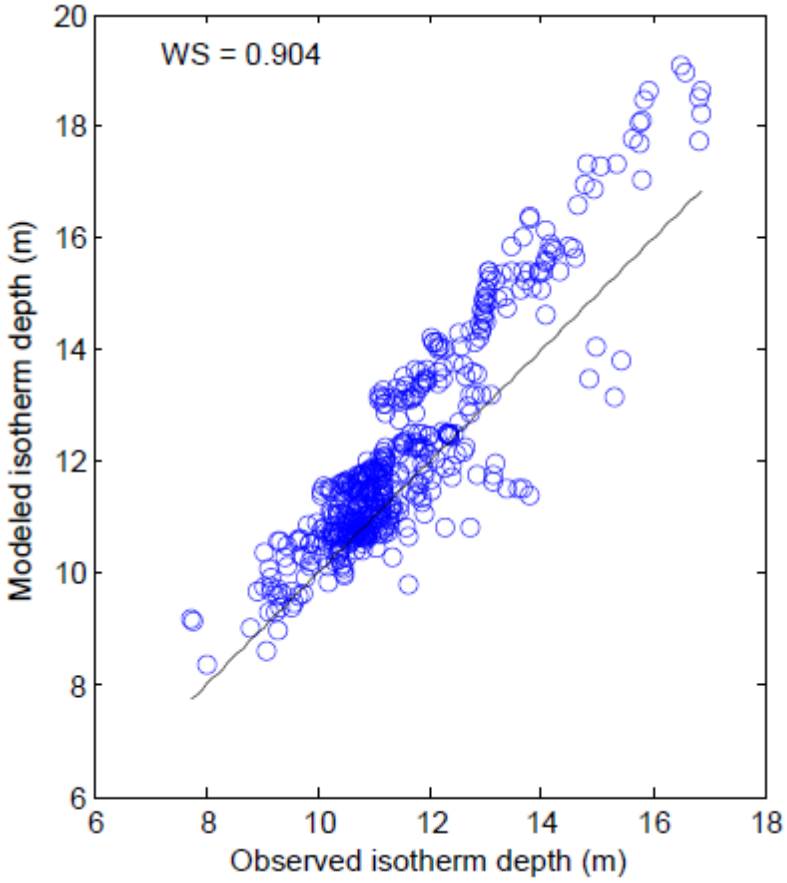

Figure 4.45. Observed and modeled 18.5°C isotherm depth for Simulation 3 (blue circles) with Δx = 50 m and Δz = 1 m. The Willmott skill number and 1:1 line is shown in black.

Power spectra were calculated for Simulation 3 from both field data and model output (Fig. 4.44). Spectral density based on model results match well with the field results, especially for frequencies lower than 3 cpd. At higher frequencies, the spectral density is limited by ELCOM's time steps, which varied from 60-550 s. However, given that the frequency of the V1H1 wave is approximately 2 cpd, motions at basin-scale frequencies were accurately modeled.

Figure 4.45 shows the comparison of the 18.5°C isotherm between field observations and model results. Many of the points lie close to the 1:1 line or parallel with a similar slope, indicating accurate model predictions of the isotherm depth. The WS value of 0.9 shown in Figure 4.45 is much higher than 0.38 and 0.18 from model runs of Simulation 1 and 2, respectively. WS values for all model runs are shown in Figure 4.46 as a function of grid size. Skill assessment results from the LDS (Fig. 4.46a) show highest WS values between 0.85 and exceeding 0.9 in a region given by Δz =0.5-1 m and Δx =50-400 m. Results from T-Chain 52 (Fig 4.46b) show WS =0.85 for Δx =100 m and Δz =0.5-1 m.

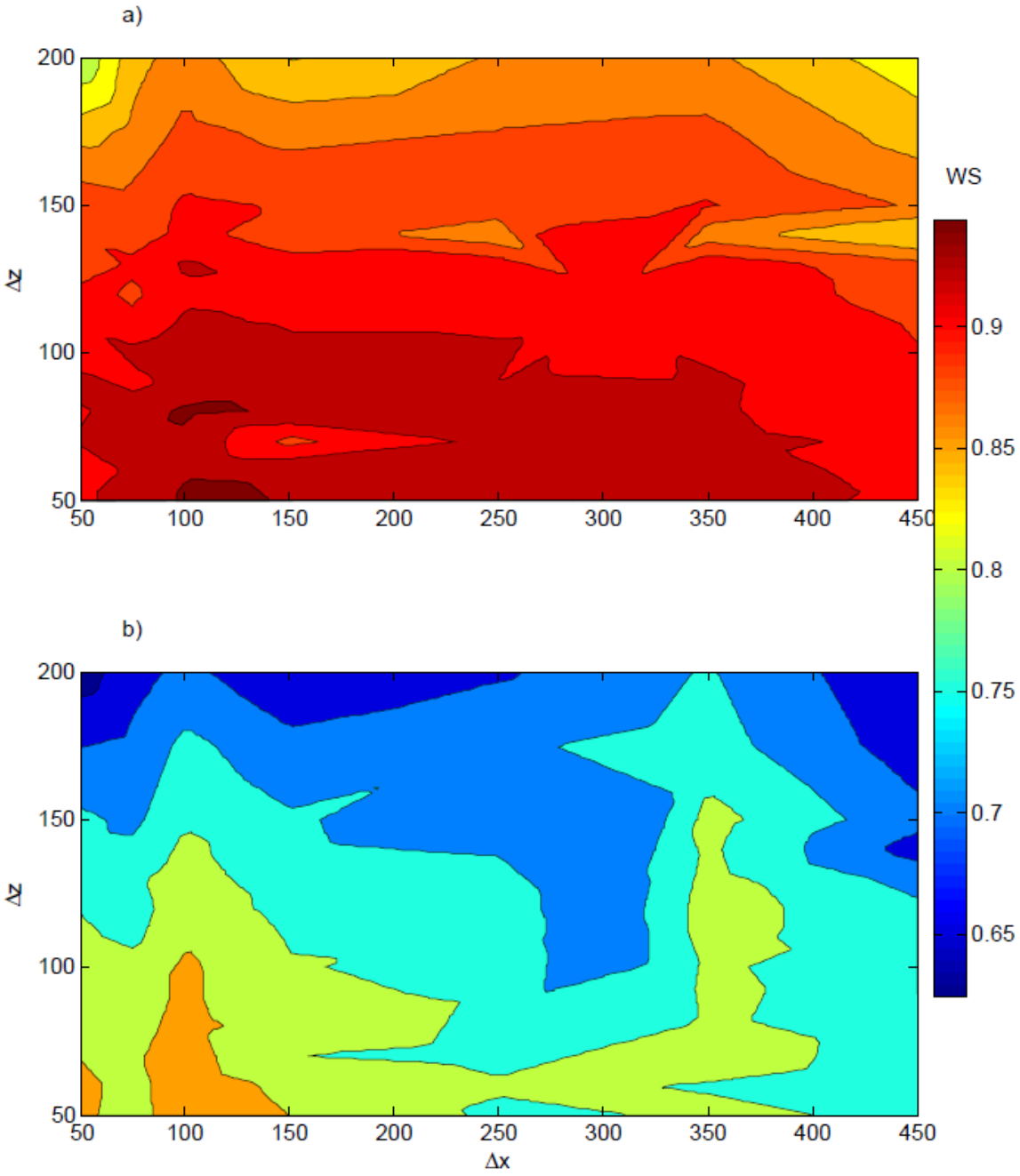

Figure 4.46. Willmott skill numbers for model runs of Simulation 3, values shown for grid sizes in the horizontal (Δx) and vertical (Δz) from a) LDS and b) T-Chain 52.

Combining Simulation Results

The three simulation events provided different results which were quantified by the reproduction of various forms of energy. Simulation 1 was affected by numerical dissipation, but dominated by numerical diffusion. Results from Simulation 2 showed excessive numerical dissipation and a decrease in potential energy due to the deepening of isotherms in the metalimnion. Simulation 3 was adversely affected by both numerical dissipation and numerical diffusion. To analyze the overall results from multiple locations, scaling the grid sizes by length scales collapses the data. The results from each simulation are combined by scaling the horizontal and vertical grid cell size by the wavelength λ and total depth H, respectively (Table 4.5). The wavelength was estimated as twice the basin length for each lake. The scaling yields the model resolution in the horizontal $\lambda / \Delta x$ and vertical $H / \Delta x$ directions. These resolutions correspond to the number of cells used to resolve the wave (or the number of points per wavelength or depth, respectively).

Based on the combined results from Simulation 1 (Fig. 4.47), under high L_N conditions, model performance was best for a horizontal resolution ($\lambda / \Delta x$) of approximately 75-120 and a vertical resolution ($H / \Delta z$) between 120-175 in order to minimize increases in potential energy and maximize the vertical movement and frequency of isotherm displacements. Errors in potential energy in this selected region were between 30-35%, and the kinetic energy was within 10-40% of field observations. Additionally, Willmott skill numbers for this region varied from 0.35-0.5.

Table 4.5. Scaling parameters and model grid resolution results. The horizontal lengthscale is represented by wavelength λ and the total depth H is used for the vertical lengthscale. Horizontal $\lambda / \Delta x$ and vertical $H / \Delta z$ grid resolutions are identified which produce the best model performance.

Simulation	λ (m)	H (m)	$\lambda / \Delta x$	$H / \Delta z$
1	1500	17.4	75-120	120-175
2	1500	17.4	120-150	40-160
3	15000	43	250-300	35-50

The results from Simulation 2 are shown in Figure 4.48. Because Simulation 2 experienced isotherm deepening in the metalimnion, E_P' values less than one would indicate model error in representing the depth of the base of the mixed-layer. Therefore, E_P' values closer to one are desirable. The region given by $\lambda / \Delta x$ = 120-150 and $H / \Delta z$ = 40-160 provides the best results: E_P' values between 0.95-1, E_K' between 0.4-0.7, and WS values between 0.22-0.26. The trend in potential energy results is more sensitive to vertical resolution (Fig. 4.48a), while the model's horizontal resolution has a larger effect on kinetic energy (Fig 4.48b). Overall, Simulation 2 better conserved the thermal structure over the model run time—although the depth of the surfaced mixed layer was overpredicted—while damping was an issue at coarser resolutions. The model skill was less than seen in Simulation 1, however the lower WS values could be

attributed to the larger difference in isotherm depths, which were more closely modeled in Simulation 1.

Figure 4.49 shows the combined results from Simulation 3. The results show much less of a clear trend than the results from the first two simulations. The potential energy results (Fig. 4.48a) show best results for $\lambda / \Delta x$ = 40, 150, and 300. For higher horizontal resolution ($\lambda / \Delta x$ = 300), a coarser vertical resolution of $H / \Delta z$ = 25-50 gives

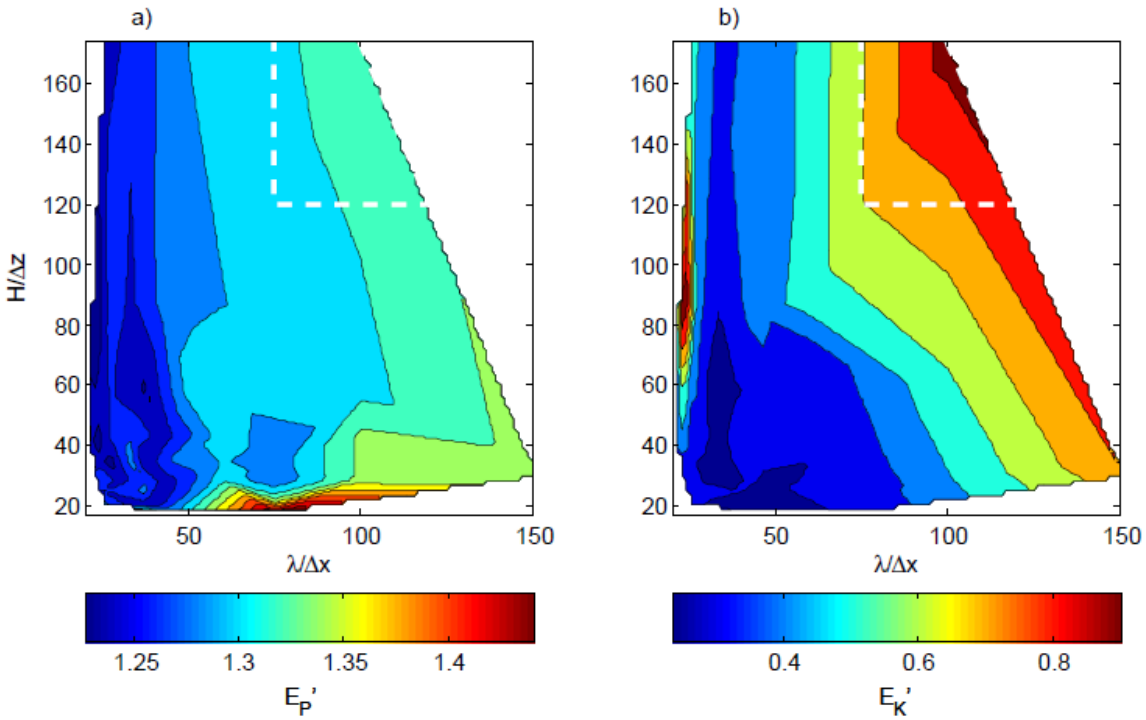

Figure 4.47. Combined normalized energy results from Simulation 1 given for a range of horizontal ($\lambda / \Delta x$) and vertical ($H / \Delta z$) grid resolutions for a) potential energy and b) kinetic energy. Region of best model performance is indicated with white dashed line.

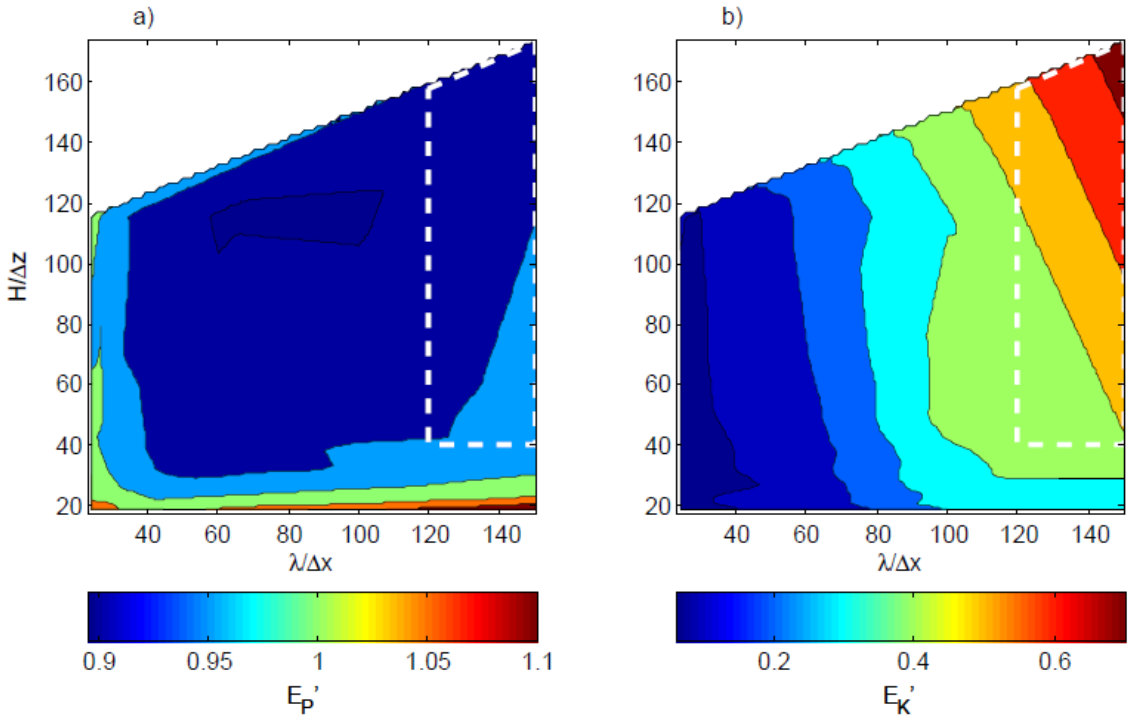

Figure 4.48. Combined normalized energy results from Simulation 2 given for a range of horizontal ($\lambda / \Delta x$) and vertical ($H / \Delta z$) grid resolutions for a) potential energy and b) kinetic energy. Region of best model performance is indicated with white dashed line.

the least increase in E_P'. The E_K' results show a clear trend for better results using higher horizontal resolutions; $\lambda / \Delta x$ = 250-300 and $H / \Delta z$ = 30-45 and 65-85 are regions in which kinetic energy is maximized. Overall, the results from Figure 4.48 show best model performance for a higher horizontal resolution of 300 and across the entire vertical resolution. However, a smaller region with a coarser vertical resolution of 35-50 was selected with the following results: errors in potential energy are within 17-21% of field values, kinetic energy errors are within 35-50%, and skill values between 0.8-0.9.

The Willmott skill values were much closer to one for Simulation 3 than the first two simulations. The range in *WS* values is large, but similar to the 0.2-0.8 range given by Wilkin (2006) when comparing temperature values. Other studies had higher skill assessment results (i.e., 0.85 and 0.95 in Warner et al., 2005); however, these values were based on parameters such as water surface elevations, which fluctuate much less than isotherm displacements. The resolution values identified for all three simulations are shown in Table 4.5.

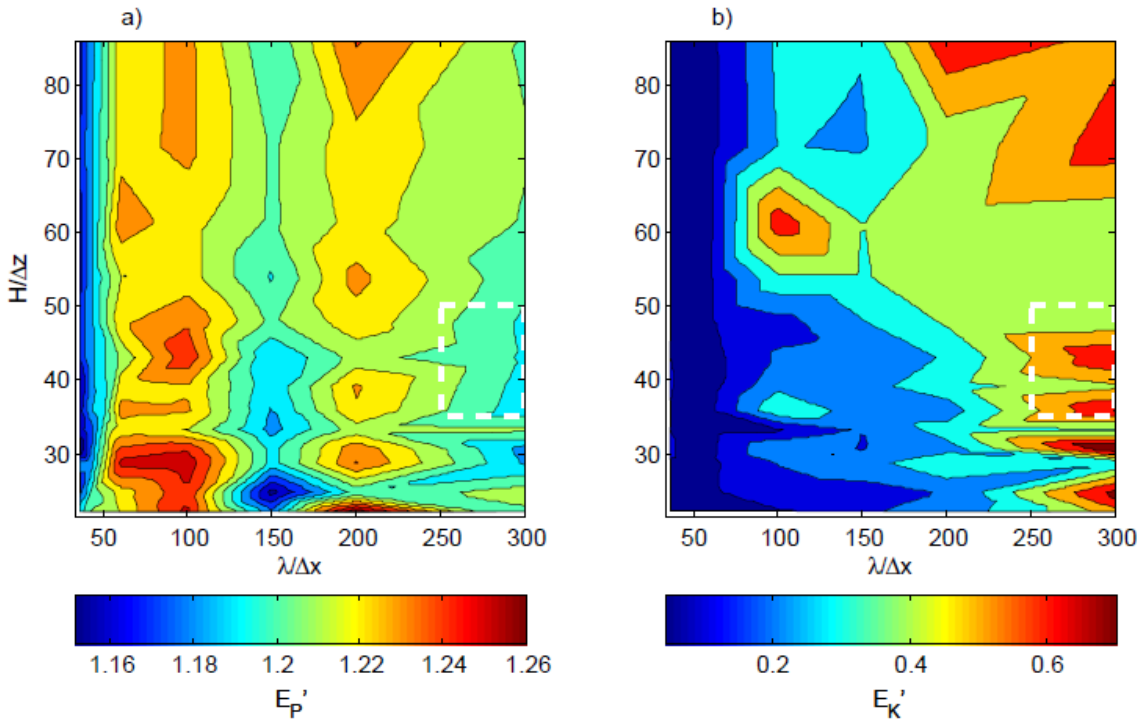

Figure 4.49. Combined normalized energy results from Simulation 3 given for a range of horizontal ($\lambda / \Delta x$) and vertical ($H / \Delta z$) grid resolutions for a) potential energy and b) kinetic energy. Region of best model performance is indicated with white dashed line.

Figure 4.47-49 provide results for simulations at different L_N conditions. However, integrating analyses from multiple simulations would yield results which are independent of the stratification and forcing conditions. Simulations 1 and 3 behaved similarly in that both experienced increases in E_P', while Simulation 3 also experienced sufficient damping. Additionally, these two events encompassed the most extreme of the conditions modeled: Simulation 1 modeled high L_N conditions while Simulation 3 experienced large amplitude motions due to low L_N. Figure 4.50 shows the results of combining the two simulations.

To maximize model performance, a region was selected which minimized E_p' and maximized E_K'. This region was given by the approximate resolution ranges of $\lambda / \Delta x$ = 150-225 and $H / \Delta z$ = 95-140. This region, indicated in Figure 4.50, resulted in a 25% error in both E_P' and E_K' estimates. Additionally, this region is on the border of the results from Simulation 1 for horizontal resolution and Simulation 3 for vertical resolution. Therefore, it could be considered to be weighted approximately equally by the results from each simulation.

Hodges et al. (2006) scaled numerical diffusion and numerical viscosity to produce a scaling factor Γ which separates a model into a diffusion-dominated vs. a dissipation-dominated regime, based on the horizontal and vertical resolution. To compare the results from this work to the literature, Γ values were calculated for each of the three simulations based on the resolutions previously defined (Fig. 4. 51).

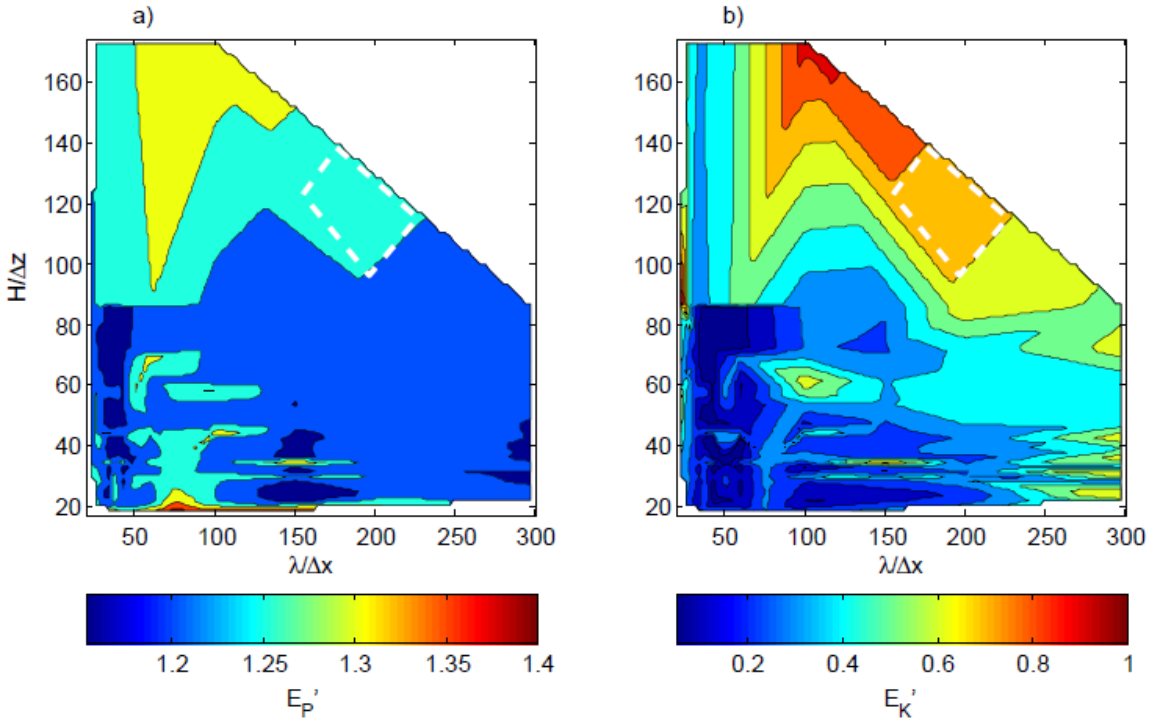

Figure 4.50. Combined normalized energy results from Simulations 1 and 3 given for a range of horizontal ($\lambda / \Delta x$) and vertical ($H / \Delta z$) grid resolutions for a) potential energy and b) kinetic energy. Region of best model performance is indicated with white dashed line.

The results shown in Figure 4.51 indicate that the simulations were modeled in almost exclusively the dissipation-dominated regime. Moreover, the region identified in Figure 4.50 for optimum model performance corresponds to a range of Γ = 22 - 34, approximately 3 - 4 times the critical value of Γ = 8.5. A dissipation-dominated regime is desirable from a modeling standpoint, as numerical diffusion will erode stratification in the system (Hodges et al., 2006).

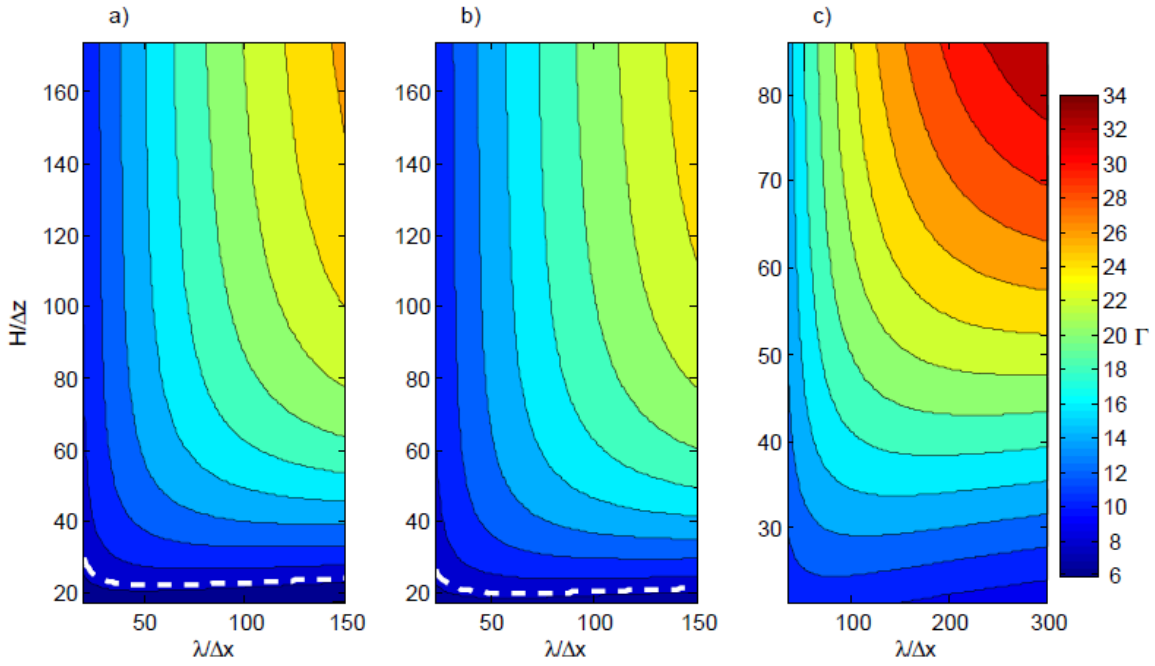

Figure 4.51. Γ values based on horizontal ($\lambda / \Delta x$) and vertical ($H / \Delta z$) grid resolutions for a) Simulation 1, b) Simulation 2, and c) Simulation 3. $\Gamma > \Gamma_C$ yields a dissipation-dominated regime, while $\Gamma < \Gamma_C$ is dominated by diffusion, where $\Gamma_C = 8.5$ (shown as white dashed line).

Validation of the Hydrostatic Assumption

It is important to consider the implications of non-hydrostatic conditions when using a hydrostatic model such as ELCOM. To determine if non-linear waves will have sufficient forcing and time to form, it is useful to use the timescale to steepening τ_s. Here, the timescale will be defined using (4.1) because it estimates the time in which steepening begins to affect the dynamics (Hodges et al., 2006). τ_s depends on the layer

Table 4.6. Parameters used to estimate steepening timescale τ_s. Values are given for a two-layer model with upper layer thickness h_1, bottom layer thickness h_2, wave amplitude ζ_0, and period T. Results given for Simulations 1, 2 and 3.

Simulation	h_1 (m)	h_2 (m)	ζ_0 (m)	T (h)	τ_s (h)
1	6.15	11.25	0.2	1.3	13
2	6.4	11	0.4	1.5	8
3	14	29	4	13	14

thicknesses, the initial wave amplitude, and the period of the gravest (V1H1) mode seiche. To estimate the steepening timescale, a two-layer approximation is made for the thermal structures shown in Figures 4.9 for Simulations 1 and 2, and 4.36 for Simulation 3. To determine if non-linear conditions will occur, an isotherm near the center of the thermocline was interpolated from field data and model output; the 17°C isotherm was chosen for Simulations 1 and 2 , and the 18.5°C was chosen for Simulation 3. See Table 4.6 for parameters used to estimate τ_s.

The time to steepening for all three simulations is shown based on an isotherm displacement (Fig. 4.52). The results for Simulation 1 (Fig. 4.52a) show two time periods where the 17°C isotherm is displaced approximately 0.2 m. This vertical displacement, combined with the two-layer structure given in Table 4.6 yields steepening time of approximately 13 h, ten times larger than the V1H1 period. ELCOM accurately predicted the vertical displacement of the isotherm both during and after both time

periods. Therefore, either the vertical displacements were not large enough to generate nonlinear motions or the waves were dissipated before nonlinear effects could form.

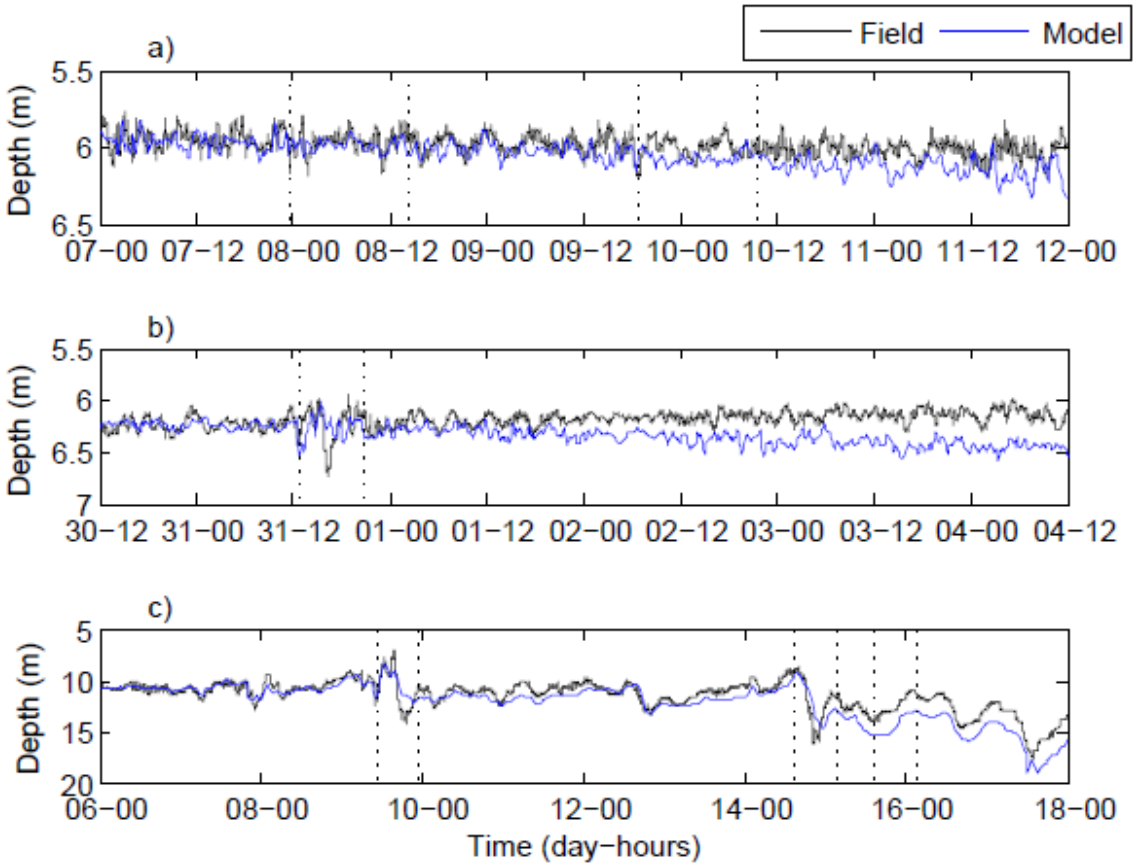

Figure 4.52. Time to steepening using isotherm displacements for a) Simulation 1, 17°C isotherm shown with model grid sizes of Δx = 15 m, and Δz = 0.1 m, b) Simulation 2, 17°C isotherm shown with model grid sizes of Δx = 10 m, and Δz = 0.1 m, and c) Simulation 3, 18.5°C isotherm shown with model grid sizes of Δx = 50 m, and Δz = 1 m.

Figure 4.52b shows the isotherm depth for both field observations and model predictions from Simulation 2. A large displacement was observed on 31 July the amplitude of this displacement was used to determine τ_s. The first vertical dashed line indicates when the initial large-amplitude disturbance was observed; the second vertical line is placed at time τ_s later, indicating when steepening (if present) should have occurred. The model predictions match field observations, except in not reproducing the deep depression of the isotherm to approximately 6.7 m. In fact, the 17°C isotherm begins to deepen in the afternoon of 1 August, well after nonlinear waves should have been produced, and shows an almost steady decline.

Figure 4.52c shows the depth of the18.5 °C isotherm from both field and model results from Simulation 3. Because of the more frequent low L_N events experienced in Simulation 3, three separate events during the 9, 14, and 15 July were isolated which produced large amplitude displacements. Similarly, a pair of vertical lines is shown to indicate the initial displacement and the time τ_s later when steepening begins to become important. The first large wind event on 9 July shows the position of the model isotherm follows the same trend as seen in the field, but with a slight reduction in wave amplitude. The second wind event on 14 July appears to be modeled even closer than the first; the isotherm depth is matched almost exactly. However, the isotherm begins to deepen shortly after the second wind event and ELCOM continues to overestimate the isotherm's depth throughout the remainder of the simulation. During the third wind event the overall trend in isotherm movement is well preserved and follows the measured behavior.

ELCOM was able to accurately predict the vertical isotherm displacement for all simulations, indicating that either no nonlinear effects were present or nonlinear effects were dissipated before a solitary wave could form. Thus, the use of the hydrostatic assumption for modeling purposes is valid.

When considering the simulation time to the wave periods given in Table 4.6, it is clear that simulations of Ada Hayden Lake for 5 d encompass approximately 80 wave periods, while a 12 d simulation of West Okoboji Lake allows for approximately 22 wave periods. Thus, while the longer simulation time of West Okoboji Lake is more than twice as long as simulations of Ada Hayden Lake, it experiences approximately ¼ of the wave oscillations. Therefore, simulation results can be related to the effects of either i) real time or ii) wave period time.

Summary

Field work has shown the formation of internal waves for lakes of differing characteristics. Because of strong stratification in Ada Hayden Lake during 2007 and 2008, winds of sufficient magnitude for large amplitude oscillations were sparse. Conversely, West Okoboji Lake was less stratified and experience higher winds, resulting in higher amplitude internal waves. Power spectra of isotherm displacement showed no dominant waves were present during chosen time periods, merely a steady decrease in power from low to high-frequency motions.

To conduct a grid resolution study of a three-dimensional, hydrostatic, numerical model, ELCOM was used to simulate observed field conditions. Overall, it was shown

that ELCOM was able to reproduce wind-forced, basin-scale internal motions. Model error was responsible for the deepening and thickening of the metalimnion, damping of internal motions, and underestimating surface water temperature. Dimensionless energy variables were used to quantify model performance in terms of retaining stratification and reproducing water column response to environmental forcing.

For a hydrostatic model to provide accurate results, it is required that non-hydrostatic forces be absent during a simulation. To address non-hydrostatic forces, a two-layer model, combined with forcing conditions, was used to evaluate potential internal wave degeneration mechanisms. These mechanisms can consist of basin-scale internal waves or higher frequency flows such as billows and bores. Additionally, field conditions appropriate for the formation of solitary waves were examined. All results indicate that a hydrostatic model was capable of predicting internal waves.

Model results, dependent on horizontal and vertical cell grid sizes, were scaled to combine measurements. These results varied between simulations from small horizontal grid size and larger vertical grid size, to coarser horizontal resolution and finer vertical resolution. Two simulated events of high and low internal wave activity were combined to yield a range of model cell grid sizes where ELCOM was shown to provide numerical results within 25% of field measurements. The model time step is related directly to the horizontal grid size and the internal wave speed using a dimensionless number.

CHAPTER 5: CONCLUSIONS

Summary

Stratification in lakes and reservoirs has been shown to restrict and inhibit vertical mixing and control the spatial variability of nutrients, dissolved oxygen, and other dissolved substances. The energy flux path consists of momentum transfer from wind-applied surface shear to the internal wave field, ultimately degenerating, dissipating, or mixing. Internal dynamics within a stratified body therefore has far-reaching implications in overall water quality and aquatic biological communities.

Numerical models play an important role in representing hydrodynamics in lakes and coastal oceans. Three-dimensional models have been shown to accurately reproduce thermal structures and circulation patterns. The coupling of physical models which solve conservation equation with biological/chemical models provide new opportunities for the use of numerical models outside the physical oceanography and limnology communities. Much of success of 3D models has been well documented; however, the comparisons made between real and simulated events (especially those of the internal wave field and surface layer circulation) is often limited to qualitative discussion.

While 3D models have been shown to be accurate in predicting many facets of hydrodynamic flows, numerical modeling is limited by the presence of numerical error: numerical diffusion erodes stratification and numerical viscosity has been shown to dampen and dissipate internal motions. Scaling has offered estimates for numerical diffusion and dissipation, but these experiments were conducted on simplified basins with

simple waves. Therefore, by considering the effects of spatial and temporal resolution on model predictions, this work evaluated the role of numerical error in model results through comparison to field observations.

The methods for conducting field observations and the procedure for implementing a three-dimensional hydrostatic model were presented. Also, dimensionless energy variables were defined, which can be used to quantify and assess model performance. Instrument locations were identified for three years of field work in two lakes. Also, sampling strategy and explanations involved when planning field studies were presented. Steps were presented which outline the necessary elements for a successful simulation using the Estuary, Lake, and Coastal Ocean Model (ELCOM).

Field work showed the formation of internal waves for lakes of differing characteristics. Because of strong stratification in Ada Hayden Lake during 2007 and 2008, winds of sufficient magnitude for large amplitude oscillations were sparse. Conversely, West Okoboji Lake was less stratified and experienced higher winds, resulting in larger amplitude internal waves. Power spectra of isotherm displacement showed no dominant waves were present during chosen time periods, merely a steady decrease in power from low to high-frequency motions.

To conduct a grid resolution study of a three-dimensional, hydrostatic, numerical model, ELCOM was used to simulate observed field conditions. Overall, it was shown that ELCOM was able to reproduce wind-forced, basin-scale internal motions. Model error was responsible for the deepening and thickening of the metalimnion, damping of internal motions, and underestimating surface water temperature. Dimensionless energy

variables were used to quantify model performance in terms of retaining stratification and reproducing water column response to environmental forcing.

For a hydrostatic model to provide accurate results, it is required that non-hydrostatic forces be absent during a simulation. To address non-hydrostatic forces, a two-layer model, combined with forcing conditions, was used to evaluate potential internal wave degeneration mechanisms. These mechanisms can consist of basin-scale internal waves or higher frequency flows such as billows and bores. Additionally, field conditions appropriate for the formation of solitary waves were examined. All results indicate that a hydrostatic model was capable of predicting internal waves.

Model results, dependent on horizontal and vertical cell grid sizes, were scaled to combine measurements. These results varied between simulations from small horizontal grid size and larger vertical grid size, to coarser horizontal resolution and finer vertical resolution. Two simulated events of high and low internal wave activity were combined to yield a range of model cell grid sizes where ELCOM was shown to provide numerical results within 25% of field measurements. The model time step is related directly to the horizontal grid size and the internal wave speed using a dimensionless number.

Recommendations

Based on the discussion and results previously presented, the following recommendations are made:

1. Internal waves have been observed in two Iowa lakes: Ada Hayden Lake and West Okoboji Lake. Field measurements at high sampling frequency (15 s) were capable of providing accurate observations of the internal lake response. Additionally, these measurements were used to provide initial and forcing conditions in a three-dimensional numerical model.
2. Degeneration mechanisms and steepening times were used to assess the validity of the hydrostatic assumption in a model. Field observations and model results supported the use of a hydrostatic model: nonlinear effects did not adversely affect model results.
3. Model predictions at various grid sizes were able to predict basin-scale motions under environmental forcing. Baroclinic motions—such as internal wave propagation—were reproduced by the model.
4. Model results were evaluated in terms of potential and kinetic energies, and isotherm displacement power spectra were used to evaluate whether vertical oscillations were being produced over the entire frequency spectrum. Comparisons of potential energy evaluated the model's ability to correctly predict the vertical temperature structure in the lake, which depends on mixing, surface heat fluxes, surface shear, and a conservative numerical scheme. Comparisons of kinetic energy provided a method for assessing whether vertical motions predicted by the model were comparable to field observations.
5. Model predictions were not invariant to the grid size chosen: smaller grid cell sizes typically gave results closer to field observations. Scaling the model results by the V1H1 wavelength λ and total depth H yielded a region where potential

and kinetic energies were within 25% of observed values. This region was identified as $\lambda / \Delta x$ = 150-225 and $H / \Delta z$ = 95-140, encompasses the region with the highest horizontal and vertical resolutions tested. Therefore, the hypothesis that a refined model grid yields the best results is supported.

Future Work

The need for further research related to three-dimensional modeling is vast. However, three areas of interest are immediately apparent. The first area of future work is to relate the effects of the duration of a simulation event. Here, two time frames were chosen for different lakes. As shown, the real time for West Okoboji Lake was longer than either of the Ada Hayden Lake simulations, but it encompassed far fewer internal wave oscillations. Additionally, the model time step was governed by the *CFL* number; all simulated events were run with a fixed *CFL* value of 1/3. Further work could relate the effects of the time step on model results.

The second area for future work is to use ELCOM to test the effects of wind duration on internal response. Field results indicate that lower magnitude winds of longer duration may yield larger amplitude oscillations than stronger winds of shorter duration. ELCOM has the ability to predict flow conditions under a wide assortment of forcing conditions; therefore, it can be used as a tool to test the effects of wind duration on internal motions. Additionally, the layered analytical model presented can be used in conjunction with a three-dimensional numerical model when comparing results.

The final item relates to the use of ELCOM in analyzing tracer study results. Tracer studies have been conducted which track intrusions generated by boundary mixing. ELCOM can be used to simulate advective transport in a tracer study. The results from model simulations can be compared to field observations to determine if small-scale mechanisms (which cannot be resolved by ELCOM) are responsible for the intrusion.

APPENDIX

```
!     ------------------------------------------------------------------
      !
FILE WOLbathy.dat
!     ------------------------------------------------------------------
      !
'West Okoboji Lake' TITLE
'Joshua A Scanlon' ANALYST
'Iowa State University' ORGANIZATION
'25-May-2010' COMMENT
!     ------------------------------------------------------------------
      !
yes   overwrite   files
!     ------------------------------------------------------------------
      !
88 x_rows
45 y_columns
82 z_layers
0 n_max
!     ------------------------------------------------------------------
      !
!     Value used to represent land and open boundaries      !
999 land_value
888 open_value
!     ------------------------------------------------------------------
      !
!     Vector Pointing North   !
-1 north_x
0 north_y
!     ------------------------------------------------------------------
      !
!     Geographic Position     !
42 latitude
0 longitude
0 altitude
!     ------------------------------------------------------------------
      !
!     Grid spacing      !
100.000 x_grid_size
100.000 y_grid_size
!     ------------------------------------------------------------------
      !
!     dz vector, from top of lake to bottom     !
0.500 dz
0.500 dz
0.500 dz
0.500 dz
⋮
0.500 dz
!     ------------------------------------------------------------------
      !
```

BATHYMETRY DATA

999	999	999	999	999	999	999	999	999	999	999	999	999	...	999
999	999	999	999	999	0	-2.68	-3.55	-3.497	-2.939	-1.646	...			999
999	999	999	999	999	-2.069	-4.134	-4.654	-4.381	-3.501	...				999
999	999	999	999	999	-2.221	-4.533	-4.925	-4.661	-4.044	...				999
999	999	999	999	999	-2.061	-4.37	-5.548	-4.8	-4.549	-3.253	...			999
999	999	999	999	999	-2.578	-6.522	-6.22	-4.937	-4.571	...				999
999	999	999	999	-2.306	-3.399	-6.649	-6.117	-4.991	-4.571	...				999
999	999	999	-1.469	-2.039	-4.738	-6.503	-6.137	-4.438	-4.573	...				999
⋮	⋮	⋮	⋮	⋮	⋮	⋮	⋮	⋮	⋮	⋮	⋮	⋮	⋮	⋮
999	999	999	999	999	999	999	999	999	999	999	999	999	...	999

```
FILE                                    run_pre.dat
!-------------------------------------------------------!
!  input files !
!-------------------------------------------------------!
!     !
'bathymetry/WOLbathy.dat'            BATHYMETRY_FILE
'bathymetry/WOLBC.dat'             BOUNDARY_CONDITION_FILE
'bathymetry/WOLupdate.dat'             UPDATE_FILE
!-------------------------------------------------------!
!  output files !
!-------------------------------------------------------!
!     !
'bathymetry/WOLout.txt'             DATAOUT_FILE
'../run/infiles/usedata.unf'             ELCOM_USEDATA_FILE
'../run/infiles/sparsedata.unf'             ELCOM_SPARSEDATA_FILE
!-------------------------------------------------------!
!  Permission to overwrite existing files  !
yes               overwrite
```

```
!  LDS profile      !
1  data sets
25 number of depths
73 23  i,j
DEPTH  WTR_TEMP
0.00 22.6814
1.26 22.6814
2.24 22.6511
3.24 22.6206
4.21 22.4262
5.20 21.9759
6.20 21.8644
7.21 21.3021
8.19 20.0913
9.20 19.6372
10.19 18.8473
11.19 18.1981
12.19 17.2589
13.20 16.2468
14.21 15.7147
15.20 15.4161
16.20 15.1198
17.20 14.8792
18.20 14.6281
19.19 14.3324
20.20 14.0866
21.20 13.8583
22.21 13.6833
23.19 13.5621
24.19 13.4136
```

```
!  T52 profile      !
1  data sets
22 number of depths
33 16  i,j
DEPTH  WTR_TEMP
0.00 22.5707
2.76 22.5707
3.73 22.4485
4.73 22.1623
5.73 21.7115
6.72 21.3268
7.72 20.2403
8.71 19.9075
9.70 19.6170
9.90 19.5213
10.70 18.8321
10.88 18.5228
11.70 17.9293
11.85 17.4877
12.68 16.4988
13.18 15.8253
13.68 15.5890
14.20 15.3390
14.67 15.2395
15.19 15.0610
15.68 14.9634
16.19 14.8045
```

```
5 data sets
0 seconds between data
0 0 0 0 0 0
TIME WIND_SPEED WIND_DIR REL_HUM SOLAR_RAD AIR_TEMP
2009187.00000 0.653 275.897 0.796 41.260 18.528
2009187.00017 0.706 268.768 0.794 41.490 18.525
2009187.00035 0.600 256.434 0.794 41.643 18.523
2009187.00052 0.600 244.185 0.795 42.715 18.520
2009187.00069 0.440 239.633 0.798 42.332 18.517
2009187.00087 0.280 225.097 0.800 43.940 18.515
2009187.00104 0.333 207.140 0.807 43.251 18.512
2009187.00122 0.440 238.060 0.809 42.715 18.510
2009187.00139 0.706 217.459 0.814 43.098 18.507
2009187.00156 0.706 218.427 0.810 44.476 18.504
2009187.00174 0.706 225.841 0.812 43.557 18.502
2009187.00191 0.653 231.953 0.800 43.404 18.499
2009187.00208 0.440 217.302 0.797 43.404 18.497
2009187.00226 0.387 195.871 0.800 43.327 18.494
2009187.00243 0.280 231.978 0.803 42.945 18.491
2009187.00260 0.440 251.447 0.804 42.715 18.489
2009187.00278 0.653 254.915 0.809 41.643 18.486
2009187.00295 0.866 266.662 0.811 42.103 18.484
2009187.00313 1.186 285.072 0.805 41.260 18.481
2009187.00330 1.132 269.240 0.799 41.184 18.479
2009187.00347 1.079 257.923 0.805 42.026 18.476
2009187.00365 0.919 268.157 0.795 41.873 18.473
2009187.00382 0.759 258.600 0.806 41.720 18.471
2009187.00399 0.813 263.987 0.799 41.796 18.468
2009187.00417 0.706 263.793 0.793 41.720 18.466
2009187.00434 0.653 259.442 0.791 42.026 18.463
2009187.00451 0.759 271.007 0.795 41.643 18.460
2009187.00469 0.866 284.999 0.796 40.725 18.458
2009187.00486 0.972 281.967 0.801 41.184 18.455
2009187.00503 1.026 262.698 0.809 41.949 18.453
2009187.00521 1.345 277.180 0.797 41.873 18.450
2009187.00538 1.505 278.003 0.776 41.873 18.447
2009187.00556 1.345 286.222 0.785 41.260 18.445
2009187.00573 1.399 284.890 0.785 41.643 18.442
2009187.00590 1.452 284.854 0.788 41.643 18.440
2009187.00608 1.612 261.584 0.805 42.485 18.437
2009187.00625 1.558 286.990 0.797 41.490 18.434
2009187.00642 1.558 281.659 0.796 41.490 18.432
2009187.00660 1.452 279.601 0.798 41.490 18.429
2009187.00677 1.399 302.169 0.809 40.954 18.427
2009187.00694 1.345 311.144 0.796 40.954 18.424
2009187.00712 1.399 307.095 0.767 40.954 18.421
2009187.00729 1.452 303.755 0.763 40.954 18.419
2009187.00747 1.558 286.216 0.789 41.260 18.416
2009187.00764 1.665 283.232 0.775 41.796 18.414
2009187.00781 1.665 284.745 0.765 41.796 18.411
2009187.00799 1.558 275.728 0.768 41.873 18.409
2009187.00816 1.825 279.825 0.770 42.179 18.406
⋮
2009198.99983 3.369 336.357 0.775 4.899 13.564
2009199.00000 3.210 333.748 0.763 5.129 13.561
```

```
DATABLOCK DESCRIPTION FILE
1.1.a                    ! datablock version
2                        ! number of output groups
2                        ! number of output sets
BEGIN GROUP_DESCRIPTION
001                      ! group reference number
tc52_grp                 ! user label
tc52_prof.unf            ! output filename
001                      ! set reference number
4                        ! number of datatypes in group
.TRUE.                   ! is_interval? logical: true if time step
interval is used for output
36                       ! output interval
0                        ! output start time
0                        ! output end time, 0 indicates entire run
0                        ! size of time list, non-zero only if
is_interval = .FALSE.
BEGIN GROUP_DESCRIPTION
002                      ! group reference number
lds_grp                 ! user label
lds_prof.unf            ! output filename
002                      ! set reference number
4                        ! number of datatypes in group
.TRUE.                   ! is_interval? logical: true if time step
interval is used for output
36                       ! output interval
0                        ! output start time
0                        ! output end time, 0 indicates entire run
0                        ! size of time list, non-zero only if
is_interval = .FALSE.
BEGIN SET_DESCRIPTION
001                      ! set reference number
tc52_set                ! user label
PROFILE_1D                ! type of set
1                        ! number of cells in set
NULL                   ! sheet type
NULL                   ! sheet calc
1.0                      ! sheet value
NULL                     ! dynamic name #1
NULL                     ! dynamic calc #1
NULL                     ! dynamic direction #1
0.0                      ! dynamic value #1
NULL                     ! dynamic name #2
NULL                     ! dynamic calc #2
NULL                     ! dynamic direction #2
0.0                      ! dynamic value #2
BEGIN SET_DESCRIPTION
002                      ! set reference number
lds_set                 ! user label
PROFILE_1D                 ! type of set
1                        ! number of cells in set
NULL                    ! sheet type
NULL                   ! sheet calc
1.0                      ! sheet value
NULL                     ! dynamic name #1
```

```
NULL                    ! dynamic calc #1
NULL                    ! dynamic direction #1
0.0                     ! dynamic value #1
NULL                    ! dynamic name #2
NULL                    ! dynamic calc #2
NULL                    ! dynamic direction #2
0.0                     ! dynamic value #2
BEGIN GROUP_DATA_TYPES
001             ! group reference number
TEMPERATURE
U_VELOCITY
V_VELOCITY
W_VELOCITY
BEGIN GROUP_DATA_TYPES
002             ! group reference number
TEMPERATURE
U_VELOCITY
V_VELOCITY
W_VELOCITY
BEGIN GROUP_TIME_LIST
001             ! group reference number
BEGIN GROUP_TIME_LIST
002             ! group reference number
BEGIN SET_CELL_DATA
001             ! set reference number
33 16 0 0
BEGIN SET_CELL_DATA
002             ! set reference number
73 23 0 0
```

```
! ------------------------------------------------------------------------!
!                                                                         !
 FILE           run_elcom.dat
!                                                                         !
! ------------------------------------------------------------------------!
!                                                                         !
'West Okoboji Lake'          TITLE
'Joshua A Scanlon'          ANALYST
'Iowa State University'          ORGANIZATION
'Prepared 25-May-2010'       COMMENT
!                                                                         !
! ------------------------------------------------------------------------!
! time controls                                                           !
!                                                                         !
2009187.00000                      start_date_cwr  ! CWR Julian day
 120.0                           del_t           ! Time step (s)
  8640.0                           iter_max        ! Number of time
steps
! ------------------------------------------------------------------------!
! file directories (require quote marks around)                           !
! (note that incomplete quotes can cause code to hang)                    !
!                                                                         !
 'infiles'                       infile_dir
 'unffiles'                      outfile_unf_dir
 'txtfiles'                      outfile_txt_dir
! ------------------------------------------------------------------------!
! input file names (include exact file extension)                         !
!                                                                         !
 sparsedata.unf                  3D_data_file
 usedata.unf                     preprocessor_file
 MetFile.dat    boundary_condition_file
 datablock.db                    datablock_file
! TracerRelease.dat               update_file (for dye...)!
! ------------------------------------------------------------------------!
! initial configuration file names (include exact file extension)
!
!                                                                         !
 T52.dat        initial_profile_file
 LDS.dat        initial_profile_file
! 2 IC_DIST_WEIGHTING    ! Inverse distance weighting used for multiple
profile init
!                                                                         !
! ------------------------------------------------------------------------!
! simulation modules (0=OFF,1=ON)                                         !
 6              iclosure                ! closure model
 1              iheat_input             ! surface thermodynamics
 0              iatmstability           ! atmospheric stability
 0              iflow                   ! inflow/outflow
 1              itemperature            ! temperature
 0              isalinity               ! salinity
 1              idensity                ! density (baroclinic forcing)
 0              irain                   ! rainfall input
 0              ibubbler                ! bubble plume destrat
 0              ijet                    ! jet destrat
 0              ifilter                 ! scalar diffusion filter
```

```
 0              iretention              ! track retention time
 0              ICAEDYM                 ! water quality module
 1              icoriolis               ! turn off/on coriolis forcing
 0              ntracer                 ! number of tracers
!                                                                      !
! ---------------------------------------------------------------------!
! default boundary conditions                                          !
!                                                                      !
!   1 = noslip all                                                     !
!   2 = freeslip all                                                   !
!   3 = drag all                                                       !
!   4 = neumann all                                                    !
!   5 = slip sides, noslip bottom                                      !
!   6 = slip sides, drag bottom                                        !
!   7 = slip sides, neumann bottom                                     !
!   8 = header values                                                  !
!   9 = turbulent benthic boundary layer                               !
!                                                                      !
 9              DEFAULT_BC
! ---------------------------------------------------------------------!
! bottom drag
!                                                                      !
 0.005          drag_btm_cd
! ---------------------------------------------------------------------!
! default values (superseded by inputs in elcom_setup.f90)             !
!                                                                      !
 2.14           WIND_SPEED_HEIGHT        ! Wind sensor height
 2.14           SCALAR_HEIGHT            ! Met sensor height
! ---------------------------------------------------------------------!
! default values (superseded by inputs in elcom_setup.f90)             !
!                                                                      !
 0.0            DEFAULT_HEIGHT           ! Initial uniform water level
 20.0           DEFAULT_WTR_TEMP         ! Initial uniform temperature
 0.0            DEFAULT_TRACER_1         ! Initial uniform tracer
 0.0            DEFAULT_WIND_SPEED       ! Uniform wind speed
 0.0            DEFAULT_WIND_DIR         ! Uniform wind direction
 0.25           DEFAULT_PAR_EXTINCTION   ! PAR extinction coefficient
45% of SW
 1.00           DEFAULT_NIR_EXTINCTION   ! NIR extinction coefficient
41% of SW
 1.00           DEFAULT_UVA_EXTINCTION   ! UVA extinction coefficient
3.5% of SW
 2.50           DEFAULT_UVB_EXTINCTION   ! UVB extinction coefficient
0.5% of SW
 0.08           mean_albedo              !
!                                                                      !
! ---------------------------------------------------------------------!
! horizontal diffusivities                                             !
!                                                                      !
 0.0            DEFAULT_DIFFUSIVITY      ! Default horizontal
diffusivity for all scalars
!                                                                      !
! ---------------------------------------------------------------------!
 'NONE'         CASE_KEYWORD
!                                                                      !
```

```
! ------------------------------------------------------------------!
! initialization options                                            !
!                                                                   !
 0              irestart                !  start from restart file
(yes=1/no=0)
 0              user_init_u_vel         !  1 = use stub routine in
elcom_user.f90
 0              user_init_v_vel
 0              user_init_w_vel
 0              user_init_temperature
 0              user_init_salinity
 0              user_init_tracer
 0              user_init_height
 0              user_init_extinction
! ------------------------------------------------------------------!
! user options                                                      !
!                                                                   !
 0              user_update_data        ! 1 = use stub routine in
elcom_user.f90
 0              gravity_angle           ! Use varying gravity angle
 2              idatablock              ! Datablock style (use 2)
!                                                                   !
! ------------------------------------------------------------------!
! model settings and controls                                       !
!                                                                   !
 1.0            model_grav_damp_x       ! damping of gravity for x
baroclinic term
 1.0            model_grav_damp_y       ! damping of gravity for y
baroclinic term
!                                                                   !
! ------------------------------------------------------------------!
! debug output controls                                             !
!                                                                   !
 2              debug_check             ! level of error checking
 2              debug_print             ! level of debug printing
 0              debug_point             ! point for debug output
 1              debug_baroclinic_x      ! error trapping on = 1, off =
0
 1              debug_baroclinic_y      ! error trapping on = 1, off =
0
!                                                                   !
! ------------------------------------------------------------------!
! scalar max and min                                                !
!                                                                   !
 0              IHARDLIMIT              ! 1 = Limit scalars to min/max
values
 1.0            min_WTR_TEMP
 40.0           max_WTR_TEMP
! 0.0            min_TRACER_1!
 !1.0            max_TRACER_1!
!                                                                   !
! ------------------------------------------------------------------!
! filter options                                                    !
!                                                                   !
 0.0            DEFAULT_FILTER
```

```
!                                                                      !
! ---------------------------------------------------------------------!
! frequency of outputs                                                 !
!                                                                      !
 50             iter_out_monitor        ! monitoring output to screen
 5000           iter_out_save           ! saving separate restart files
 1000           iter_out_restart        ! overwriting restart output!
!                                                                      !
! ---------------------------------------------------------------------!
! start of outputs                                                     !
!                                                                      !
 0              start_output_monitor    ! monitor output to screen
 0              start_output_save       ! saved restart files
!                                                                      !
! ---------------------------------------------------------------------!
! conjugate gradient iteration controls                                !
!                                                                      !
 1.e-16         CGM_TOL                 ! CGM tolerance
 30             CGM_MIN                 ! minimum iterations of CGM
 1000           CGM_MAX                 ! maximum iterations of CGM
!                                                                      !
! ---------------------------------------------------------------------!
! restart file names (do not include file extension)                   !
!                                                                      !
 save           restart_save_file
 restart_final  restart_out_file
```

```
! Profile translation
lds_prof.unf
../infiles/sparsedata.unf
../ncfiles/profile_LDS.nc
-1
-1
clobber           !replace
no_map
no_echo


! Profile translation
tc52_prof.unf
../infiles/sparsedata.unf
../ncfiles/profile_TC52.nc
-1
-1
clobber           !replace
no_map
no_echo
```

REFERENCES

Antenucci, J. P., J. Imberger, and A. Saggio. 2000. Seasonal evolution of the basin-scale internal wave field in a large stratified lake. Limnol. Oceanogr. **45:** 1621-1638.

Beletsky, D., W. P. Oconnor, D. J. Schwab, and D. E. Dietrich. 1997. Numerical simulation of internal Kelvin waves and coastal upwelling fronts. J. Phys. Oceanogr. **27:** 1197-1215.

Boegman, L., G. N. Ivey, and J. Imberger. 2005. The energetics of large-scale internal wave degeneration in lakes. J. Fluid Mech. **531:** 159-180.

Botelho, D., J. Imberger, C. Dallimore, and B. R. Hodges. 2009. A hydrostatic/non-hydrostatic grid-switching strategy for computing high-frequency, high wave number motions embedded in geophysical flows. Environ. Modell. Softw. **24:** 473-488.

Botelho, D. A., and J. Imberger. 2007. Downscaling model resolution to illuminate the internal wave field in a small stratified lake. J. Hydraul. Eng. **133:** 1206-1218.

Casulli, V., and R. T. Cheng. 1992. Semi-implicit finite-difference methods for 3-dimensional shallow-water flow. International Journal for Numerical Methods in Fluids **15:** 629-648.

Chung, S. W., M. R. Hipsey, and J. Imberger. 2009. Modelling the propagation of turbid density inflows into a stratified lake: Daecheong Reservoir, Korea. Environ. Modell. Softw. **24:** 1467-1482.

Csanady, G. T. 1982. On the structure of transient upwelling events. J. Phys. Oceanogr. **12:** 84-96.

Cushman-Roisin, B. 1994. Introduction to Geophysical Fluid Dynamics. Prentice-Hall.

Eckert, W., J. Imberger, and A. Saggio. 2002. Biogeochemical response to physical forcing in the water column of a warm monomictic lake. Biogeochemistry **61:** 291-307.

Fee, E. J. 1967. The seiches of Lake West Okoboji. Iowa State J. Sci. **42:** 73-81.

Fee, E. J., and R. W. Bachmann. 1968. An empirical study of Defant method of seiche analysis. Limnol. Oceanogr. **13:** 665-&.

Gill, A. E. 1982. Atmosphere-Ocean Dynamics. Academic Press.

Gomez-Giraldo, A., J. Imberger, and J. P. Antenucci. 2006. Spatial structure of the dominant basin-scale internal waves in Lake Kinneret. Limnol. Oceanogr. **51:** 229-246.

Heaps, N. S., and A. E. Ramsbottom. 1966. Wind effects on water in a narrow two-layered lake. Philosophical Transactions of the Royal Society of London Series A-Mathematical and Physical Sciences **259:** 391-&.

Hodges, B.R. 2000. Numerical techniques in CWR-ELCOM. Technical Report WP 1422 BH, Centre for Water Research, University of Western Australia.

Hodges, B. R., and C. Dallimore. 2007. Estuary, Lake and Coastal Ocean Model: ELCOM. Version 2.2: User's manual. Centre for Water Research, University of Western Australia.

Hodges, B. R., J. Imberger, A. Saggio, and K. B. Winters. 2000. Modeling basin-scale internal waves in a stratified lake. Limnol. Oceanogr. **45:** 1603-1620.

Hodges, B. R., B. Laval, and B. M. Wadzuk. 2006. Numerical error assessment and a temporal horizon for internal waves in a hydrostatic model. Ocean Model. **13:** 44-64.

Hodges, B. R., and F. J. Rueda. 2008. Semi-implicit two-level predictor-corrector methods for non-linearly coupled, hydrostatic, barotropic/baroclinic flows. International Journal of Computational Fluid Dynamics **22:** 593-607.

Horn, D. A., J. Imberger, and G. N. Ivey. 2001. The degeneration of large-scale interfacial gravity waves in lakes. J. Fluid Mech. **434:** 181-207.

Imberger, J. 1994. Measurement of turbulent properties in a natural system, p. 1-20. *In* C. A. Pugh [ed.], Fundamentals and Advancements in Hydraulic Measurements and Experimentation.

Imberger, J. 1998. Flux paths in a stratified lake: a review, p. 1-18. *In* J. Imberger [ed.], Physical Processes in Lakes and Oceans. Coastal and Estuarine Studies. American Geophysical Union.

Imberger, J. 2004. Characterizing the dynamical regimes of a lake, p. 1121-1130. *In* A. H. El-Shaarawi [ed.], The Encyclopaedia of Environmetrics. Wiley.

Imberger, J., and J. C. Patterson. 1981. A dynamic reservoir simulation model—DYRESM 5, p. 310-361. *In* H. Fisher [ed.], Transport models for inland and coastal waters. Academic Press.

Imberger, J., and J.C. Patterson. 1990. Physical limnology. Advances in Applied Mechanics **27:** 303-475.

Kalff, J. 2002. Limnology. Prentice-Hall.

Kocyigit, M. B., and R. A. Falconer. 2004. Three-dimensional numerical modelling of wind-driven circulation in a homogeneous lake. Advances in Water Resources **27:** 1167-1178.

Kundu, P. K., and I. M. Cohen. 2008. Fluid Mechanics. Academic Press.

Laval, B., B. R. Hodges, and J. Imberger. 2003a. Reducing numerical diffusion effects with pycnocline filter. J. Hydraul. Eng. **129:** 215-224.

Laval, B., J. Imberger, B. R. Hodges, and R. Stocker. 2003b. Modeling circulation in lakes: Spatial and temporal variations. Limnol. Oceanogr. **48:** 983-994.

Laval, B. E., J. Imberger, and A. N. Findikakis. 2005. Dynamics of a large tropical lake: Lake Maracaibo. Aquatic Sciences **67:** 337-349.

Lemckert, C., and J. Imberger. 1998. Turbulent benthic boundary layer mixing events in fresh water lakes, p. 503-516. *In* J. Imberger [ed.], Physical Processes in Lakes in Oceans. Coastal and Estuarine Studies.

Leon, L. K., J. Imberger, R. E. H. Smith, R. E. Hecky, D. C. L. Lam, and W. M. Schertzer. 2005. Modeling as a tool for nutrient management in Lake Erie: a hydrodynamics study. Journal of Great Lakes Research **31:** 309-318.

Leonard, B. P. 1991. The ULTIMATE conservative difference scheme applied to unsteady one-dimensional advection. Computer Methods in Applied Mechanics and Engineering **88:** 17-74.

Lighthill, M. J. 1969. Dynamic response of the Indian Ocean to onset of the Southwest Monsoon. Philosophical Transactions of the Royal Society of London Series A-Mathematical and Physical Sciences **265:** 45-92.

Liu, Y., P. MacCready, B. M. Hickey, E. P. Dever, P. M. Kosro, and N. S. Banas. 2009. Evaluation of a coastal ocean circulation model for the Columbia River plume in summer 2004. J. Geophys. Res. **114:** C00B04.

Lorenz, E. N. 1955. Available potential energy and the maintenance of the general circulation. Tellus **7:** 157-167.

MacIntyre, S., K. M. Flynn, R. Jellison, and J. R. Romero. 1999. Boundary mixing and nutrient fluxes in Mono Lake, California. Limnol. Oceanogr. **44:** 512-529.

Marti-Cardona, B., T. E. Steissberg, S. G. Schladow, and S. J. Hook. 2008. Relating fish kills to upwellings and wind patterns in the Salton Sea. Hydrobiologia **604:** 85-95.

Monismith, S. G. 1985. Wind-forced motions in stratified lakes and their effect on mixed-layer shear. Limnol. Oceanogr. **30:** 771-783.

Moum, J. N., and J. D. Nash. 2000. Topographically induced drag and mixing at a small bank on the continental shelf. J. Phys. Oceanogr. **30:** 2049-2054.

Münnich, M., A. Wüest, and D. M. Imboden. 1992. Observations of the second vertical mode of the internal seiche in an alpine lake. Limnol. Oceanogr. **37:** 1705-1719.

Pedlosky, J. 1979. Geophysical Fluid Dynamics. Springer.

Rao, Y. R., C. H. Marvin, and J. Zhao. 2009. Application of a numerical model for circulation, temperature and pollutant distribution in Hamilton Harbour. Journal of Great Lakes Research **35:** 61-73.

Rueda, F. J., E. Sanmiguel-Rojas, and B. R. Hodges. 2007. Baroclinic stability for a family of two-level, semi-implicit numerical methods for the 3D shallow water equations. International Journal for Numerical Methods in Fluids **54:** 237-268.

Saggio, A., and J. Imberger. 1998. Internal wave weather in a stratified lake. Limnol. Oceanogr. **43:** 1780-1795.

Saggio, A., and J. Imberger. 2001. Mixing and turbulent fluxes in the metalimnion of a stratified lake. Limnol. Oceanogr. **46:** 392-409.

Simanjuntak, M. A., J. Imberger, and K. Nakayama. 2009. Effect of stair-step and piecewise linear topography on internal wave propagation in a geophysical flow model. J. Geophys. Res.-Oceans **114**.

Smith, S. D. 1988. Coefficients for sea surface wind stress, heat flux, and wind profiles as a function of wind speed and temperature. Journal of Geophysical Research **93:** 15467-15472.

Spigel, R. H., and J. Imberger. 1980. The classification of mixed-layer dynamics in lakes of small to medium size. J. Phys. Oceanogr. **10:** 1104-1121.

Spigel, R. H., J. Imberger, and K. N. Rayner. 1986. Modeling the diurnal mixed layer. Limnol. Oceanogr. **31:** 533-556.

Spillman, C. M., J. Imberger, D. P. Hamilton, M. R. Hipsey, and J. R. Romero. 2007. Modelling the effects of Po River discharge, internal nutrient cycling and hydrodynamics on biogeochemistry of the Northern Adriatic Sea. Journal of Marine Systems **68:** 167-200.

Stevens, C., G. Lawrence, P. Hamblin, and E. Carmack. 1996. Wind forcing of internal waves in a long narrow stratified lake. Dyn. Atmos. Oceans **24:** 41-50.

Stevens, C. L., and G. A. Lawrence. 1997. Estimation of wind-forced internal seiche amplitudes in lakes and reservoirs, with data from British Columbia, Canada. Aquatic Sciences **59:** 115-134.

Thompson, R. O., and J. Imberger. 1980. Response of a numerical model of a stratified lake to wind stress, p. 562-570. 2nd International Symposium on Stratified Flows.

Turner, J. S. 1973. Buoyancy Effects in Fluids. Cambridge University Press.

Vidal, J., and X. Casamitjana. 2008. Forced resonant oscillations as a response to periodic winds in a stratified reservoir. Journal of Hydraulic Engineering-Asce **134:** 416-425.

Vidal, J., X. Casamitjana, J. Colomer, and T. Serra. 2005. The internal wave field in Sau reservoir: Observation and modeling of a third vertical mode. Limnol. Oceanogr. **50:** 1326-1333.

Wilkin, J. L. 2006. The summertime heat budget and circulation of southeast New England shelf waters. J. Phys. Oceanogr. **36:** 1997-2011.

Willmott, C. J. 1981. On the validation of models. Phys. Geogr. **2:** 184-194.

Willmott, C. J. 1982. Some comments on the evaluation of model performance.

Willmott, C. J., and D. E. Wicks. 1980. An empirical method for the spatial interpolation of monthly precipitation within California. Phys. Geogr. **1:** 59-73.

Winters, K. B., P. N. Lombard, J. J. Riley, and E. A. D'Asaro. 1995. Available potential energy and mixing in density-stratified fluids. J. Fluid Mech. **289:** 115-128.

Wüest, A., and A. Lorke. 2003. Small-scale hydrodynamics in lakes. Annu. Rev. Fluid Mech. **35:** 373-412.

Yeates, P. S., J. Imberger, and C. Dallimore. 2008. Thermistor chain data assimilation to improve hydrodynamic modeling skill in stratified lakes and reservoirs. J. Hydraul. Eng. **134:** 1123-1135.

Yelland, M., and P. K. Taylor. 1996. Wind stress measurements from the open ocean. J. Phys. Oceanogr. **26:** 541-558.